Structure, faulting and gas accumulation: southeast Wanganui Basin, New Zealand

Lloyd Pledger

A thesis submitted to Victoria University
of Wellington in fulfilment of the
requirements for the degree of
Master of Science in Geophysics.

Victoria University of Wellington

January 2012

Abstract

There has been low interest in petroleum exploration in the Wanganui Basin as it lacks known hydrocarbon source rock of sufficient age or burial depth. However, the onshore Southeast Wanganui Basin has many occurrences of methane-rich biogenic gas found in shallow water wells. This project used three studies across the Horowhenua area to examine the faulting style in the Southeast Wanganui Basin where it is bounded by the Tararua range-front, and how this faulting relates to the accumulation of gas deposits in the shallow sedimentary section.

South of Levin the Tararua range front steps laterally near Muhunoa East Road. A previous seismic reflection line identified a deep intra-basement arrival, which could have been either a low-angle thrust fault or side-swipe from a pull-apart basin at the step in the Tararua range front. Two seismic lines and a gravity survey found no sub-vertical drops in basement depth which would indicate the presence of a pull-apart basin or a favourable surface off which a laterally travelling seismic wave could reflect. The intra-basement arrival on the previous seismic line was therefore interpreted to be from an intra-basement low-angle thrust fault.

Also two biogenic gas sites also were surveyed. A shallow gas reservoir east of Levin on Wallace Road, abutting the Tararua range front, had been discovered when a water well was drilled; and a potential reservoir southwest of Sanson was located when an aerial survey identified a domed structure with high resistivity. In both areas biogenic gas was thought to be trapped in buried sand dunes at a depth of approximately 20 m. Shallow seismic refraction and reflection methods and amplitude variation with offset analysis were used to map both reservoir bodies and confirm the presence of biogenic gas.

Acknowledgements

Firstly I would like to thank my supervisor Professor Tim Stern for all his guidance throughout this study, and for working with Ian R Brown Associates Ltd to put me onto this study in the first place.

Special thanks to Susi Woelz and Mark Henderson for their cheerful and tireless assistance with field work, and Ian Calman, Adrian Benson and Alex Fuerst for their invaluable help with data processing and interpretation. I would like to acknowledge the many kind landowners across the Horowhenua region who let me do surveys across their properties and made this study possible.

I would also like to thank my fantastic office mates Kathi Unglert, Denise Fernandez, Richard Davy, Sanne Maas, Karen McKinnon, Laura Kehrl, Brook Tozer, Syuhada, Nicolas Brikke and Nick Cozens for their help with field work and keeping me sane.

Finally I would like to thank my partner Renee and my family for their patience and support throughout.

Contents

List of Figures

List of Tables

Chapter 1

Introduction

The South Wanganui Basin, located on the west coast of the lower North Island of New Zealand, is a rapidly subsiding Plio-Pleistocene basin that is part of an active continental margin. The South Wanganui Basin is located in an area of mild crustal compression but rapid crustal downwarp. Because of the strong vertical movement here it is likely that mantle dynamics linked to the coupling of the negatively buoyant subducting slab to the overriding plate is the driving force behind the surface subsidence observed [Stern *et al.*, 1992; Ewig, 2008]. The South Wanganui Basin has a -150 mGal gravity anomaly which can be only partially explained by sediment infill. Flexural downwarp of the crust due to strong coupling with the subducting plate interface has been proposed as a driving mechanism for the development of this basin [Stern *et al.*, 1992].

The Taranaki Basin is a broad compressional foreland basin that formed to the west of the Taranaki Fault System during the Miocene, owing to 70±30 km of Miocene shortening in the western North Island [Stern and Davey,

1990; Stern *et al.*, 2006; Nicol *et al.*, 2007]. At the start of the Pliocene compression slowed and the rapid subsidence of the South Wanganui Basin began. The subsidence is currently modulated by the predominantly reverse Kapiti Manawatu Fault System (KMFS) [Lamarche *et al.*, 2005]. The rapid crustal downwarp in the South Wanganui Basin has been accompanied from the early Pliocene by equally rapid rock uplift in the central North Island [Pulford and Stern, 2004].

Present-day relative plate motion on the Pacific-Australia plate boundary is 40-42 mm/yr at an azimuth of 261° [DeMets *et al.*, 1994]. Of this motion 17-22 mm/yr is accommodated between the west coast of New Zealand and the Hikurangi subduction front [Barnes *et al.*, 1998; Darby and Beavan, 2001; Nicol and Beavan, 2003; Barnes *et al.*, 2002], leaving 18-25 mm/yr compression to be accommodated to the west of the North Island across the South Wanganui Basin.

In the last 2 Ma contraction across the plate boundary zone has facilitated the uplift of the Tararua Ranges. Eroded material from this rapid uplift has been washed down to fill the accommodation space in the rapidly subsiding South Wanganui Basin, enabling the high sedimentation rate observed. Subsidence and sedimentation rates in the South Wanganui Basin are greater than 1 mm/yr, contributing to more than 4 km of basin subsidence [Anderton, 1981; Lamarche *et al.*, 2005].

This study investigates two aspects of this enigmatic basin. The first part of this thesis is a structural study at the onshore southeast margin of the basin near Muhunoa East Road (figure 1.1) to unravel an ambiguity about the origin of a low angle reflection in a reprocessed seismic reflection

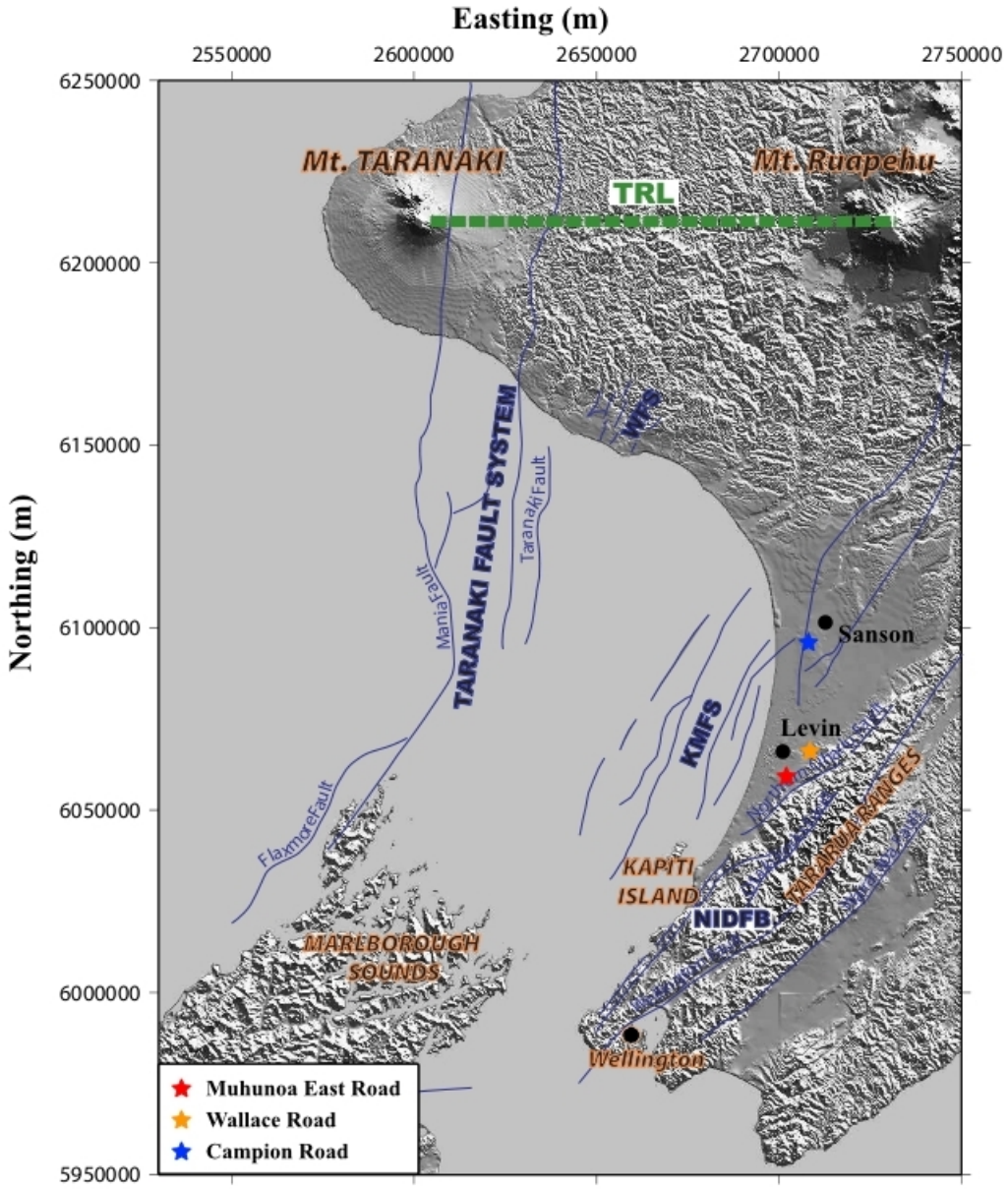

Figure 1.1: Map of the South Wanganui Basin. Taranaki Fault System, Kapiti Manawatu Fault System (KMFS), North Island Dextral Fault Belt (NIDFB), individual faults (blue lines) and study areas are shown. The green line indicates the location of the Taranaki-Ruapehu line (TRL) [Salmon *et al.*, 2011] Original figure from Ewig [2008]. Scale is in New Zealand Map Grid (NZMG).

line [Aharoni, 1991; Ewig, 2008]: is it the base of a sedimentary section or does it represent a low angle thrust that was active in the earlier phase of the Wanganui area?

The second and main part of this thesis is focussed on the detection and imaging of shallow gas bodies. The rapid subsidence of the South Wanganui Basin causes fast sedimentation. This combined with a lack of major faulting in the basin favours the generation and trapping of biogenic gas. The faults appear to be superficial in the sense that they accommodate only 50-75% of the total vertical displacement [Lamarche *et al.*, 2005]. There have been numerous gas shows in water wells across the onshore South Wanganui Basin, demonstrating that biogenic gas may be present in commercial quantities; so it is important to develop tools to locate and map potential biogenic gas reservoirs as conventional gas deposits become more scarce. Because the gas bodies are shallow, their presence can be detected by independent means, and it is possible to design simple experiments with land-based seismic equipment to investigate P and S wave partitioning at the top of gas-bearing sediments.

Two biogenic gas sites are investigated in this study: Wallace Road and Campion Road (figure 1.1) [Proposed Geoprobe Programme, PEP 38771 Report, Ian R Brown Associates Ltd]. At the Wallace Road site biogenic gas was found at a depth of 20 m in a buried sand dune structure while drilling a water well. The confirmed presence of gas and known stratigraphy allows for a controlled seismic study of shallow biogenic gas. At the Campion Road site an airborne survey detected a high resistivity anomaly which suggested the presence of shallow gas. The seismic response from a survey at Campion Road can be compared with the controlled survey at Wallace Road to determine

the similarities and differences in the subsurface structure.

Chapter 2

Tectonic setting of the Horowhenua region

2.1 New Zealand tectonic setting

New Zealand lies on the boundary between the Australian and Pacific plates. At the southern tip of the South Island the Australian plate subducts beneath the Pacific plate in the Puysegur trench at a rate of 38 mm/a [DeMets *et al.*, 1990]. Over the length of the South Island the polarity of the subducting system changes until off the east coast of the North Island the Pacific plate subducts beneath the Australian plate in the Hikurangi trench at a rate of 42-48 mm/a [DeMets *et al.*, 1990]. Between the two opposing subduction regimes the plate motion is accommodated by the Alpine Fault and the Marlborough Fault System.

The nature of the plate boundary through New Zealand changed from transcurrent motion to oblique convergence in the last 25 Ma [Stock and

Molnar, 1982]. Since then, zones of compression and tectonic shortening have formed on the overriding Australian plate and migrated southward, as have the depocenters of basins that form within these zones. The youngest of these basins is the South Wanganui Basin (figure 2.1), which is filled with sediment of Plio-Pleistocene age [Anderton, 1981]. The oblique subduction of the Pacific plate under the lower North Island causes both strike-slip and compressional deformation in the upper plate. The strike-slip component of this deformation is primarily accommodated along the North Island dextral fault belt (NIDFB), a zone of numerous individual faults to the east of the South Wanganui Basin [Beanland, 1995].

2.2 South Wanganui Basin

The South Wanganui Basin is an asymmetric Plio-Pleistocene sedimentary basin located to the south of the actively extensional Central Volcanic Region [Anderton, 1981; Stern, 1987]. It has subsidence rates of about 1 mm/a and with predominantly reverse faulting [Stern *et al.*, 1992]. Seismic data show that the South Wanganui Basin is a broad half-graben structure trending northeast with a depocentre that lies 20km south of Wanganui [Anderton, 1981]. The basin contains up to 4000 m of Plio-Pleistocene sediments that rest unconformably on greywacke basement rocks which are exposed in the ranges to the east. The preferred explanation for the driving mechanism of the basin is a broad-scale lithospheric flexure due to high frictional coupling at the plate interface (figure 2.2) [Stern *et al.*, 1992; Ewig, 2008]. Some additional vertical loading may come from overthrusted mantle lithosphere

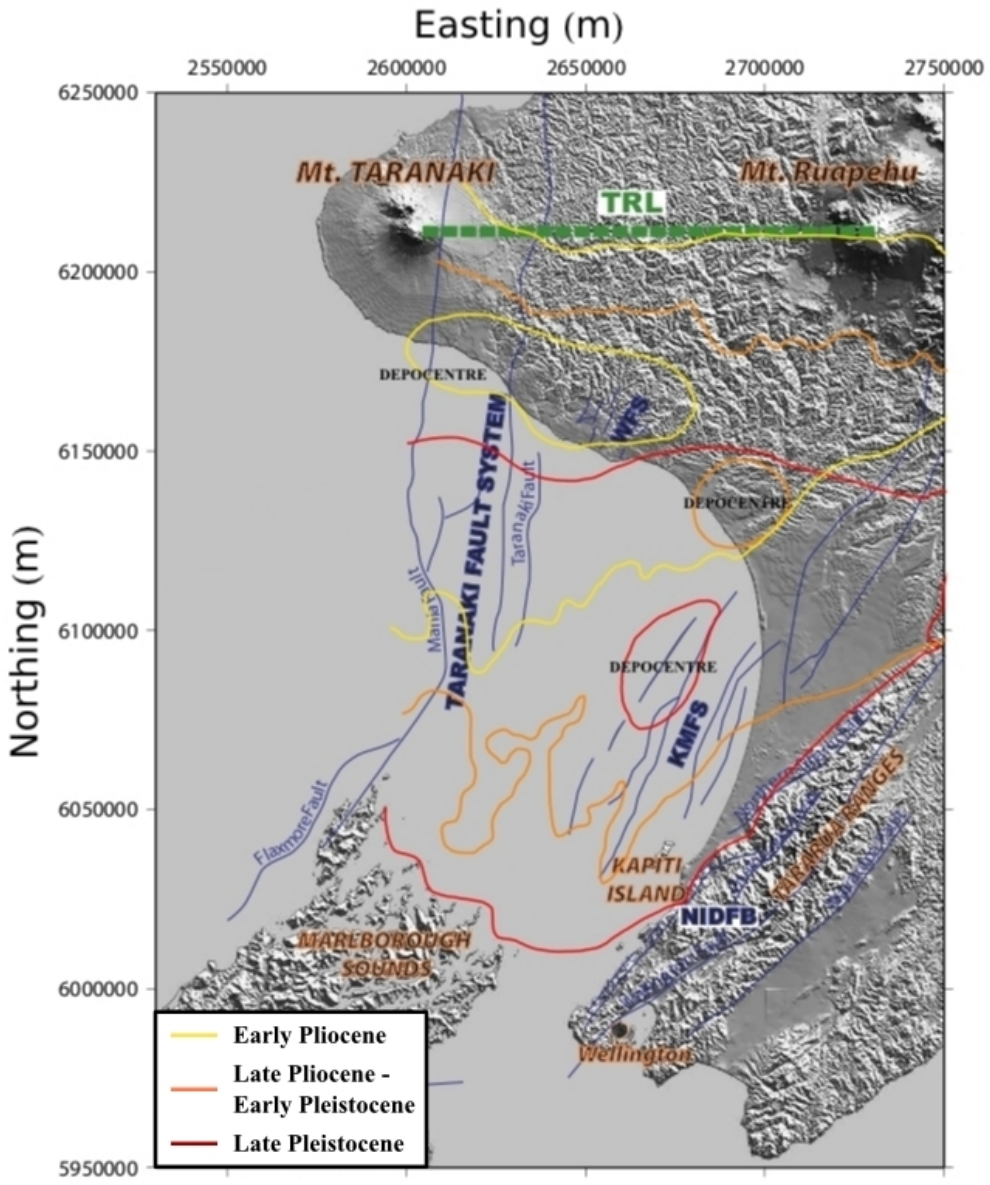

Figure 2.1: Map of the South Wanganui Basin showing major faults, the limits of the basin depocentres and Plio-Pleistocene sediment distribution. The green line indicates the location of the Taranaki-Ruapehu line (TRL) [Salmon *et al.*, 2011]. The Taranaki Fault System consisting of the Taranaki, Manaia and Flaxmore thrust faults is shown in the west. Also shown are the reverse Kapiti-Manawatu Fault System (KMFS) [Lamarche *et al.*, 2005] and the North Island dextral fault belt (NIDFB). The southward migration of the South Wanganui Basin depocentre and sediment distribution through time are shown [Anderton, 1981]. Original figure from Ewig [2008]. Scale is in New Zealand Map Grid (NZMG).

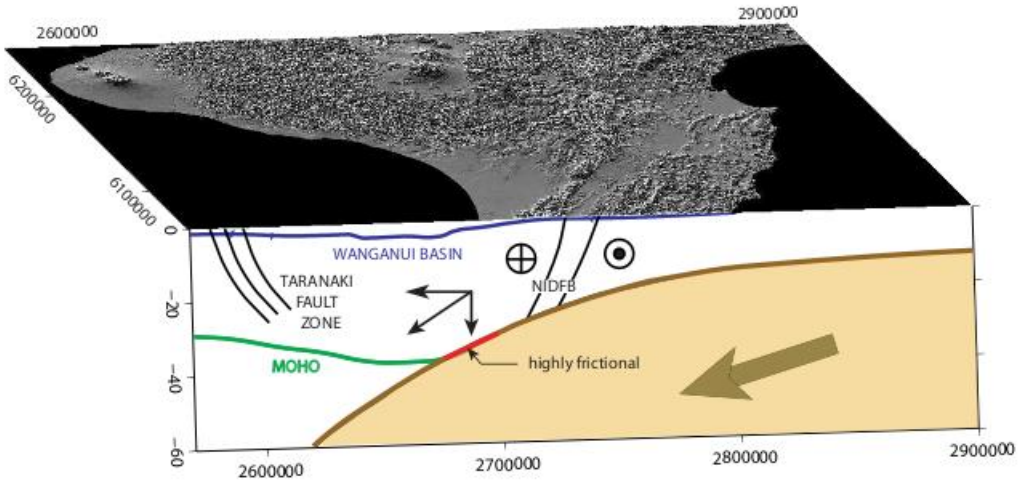

Figure 2.2: This figure shows the proposed driving force beneath the South Wanganui Basin. The shear force at the highly coupled interface creates a vertical pull as well as in-plane stress in the overriding plate. The blue line shows the depth of the sediment basin. The green line shows the proposed Moho of the thickened Australian plate. Also shown are the approximate locations of the Taranaki Fault Zone in the west and North Island dextral fault belt (NIDFB) in the east. Depths are in km. Reproduced from [Ewig, 2008]. Scale is in New Zealand Map Grid (NZMG) and depth is in km.

south of the Taranaki-Ruapehu line [Salmon *et al.*, 2011; Stern *et al.*, 2006].

The South Wanganui Basin is not a traditional back-arc basin; because of the absence of volcanic arc magmatism and the contractional tectonics at the boundaries along the Taranaki fault and the Kapiti-Manawatu Fault System (KMFS). There is some strike-slip motion on the KMFS but both bounding fault systems display largely reverse motion (figure 2.2, figure 2.3) [Proust *et al.*, 2005]. Interpretation of seismic stratigraphy reveals two phases of basin development: a pre-growth phase (3.8 to 1.35 Ma) and a syn-growth phase (1.35 Ma to present). The Pliocene pre-growth mega-sequence consists of three seismic units which broadly change from deep marine to non-marine

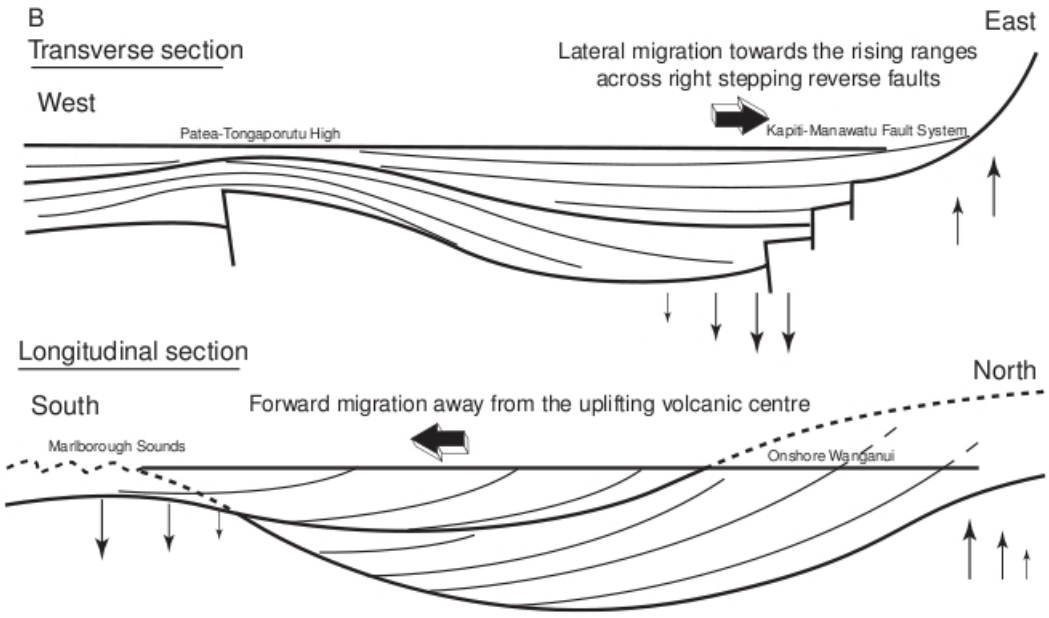

Figure 2.3: Diagrammatic arrangement of Plio-Pleistocene stratal units in the South Wanganui Basin perpendicular and parallel to the main sediment pathways. The sediment fill is composed of two mega-sequences prograding southeastward towards the foundering Marlborough Sounds and onlapping the eastern side of the axial mountain ranges along the Kapiti-Manawatu Fault System. The unconformity between the two mega-sequences developed as a consequence of the onset of the fault activity in the Kapiti-Manawatu Fault System at ca 1.75 Ma. Reproduced from [Proust *et al.*, 2005].

depositional environments. The Pleistocene syn-growth mega-sequence is made up of shallow marine sediments that exhibit little change in depositional environment through time and are transgressive across the Pliocene mega-sequence. The unconformity between the two mega-sequences is due to the onset of fault activity in the KMFS ca 1.75 Ma (figure 2.3) [Proust *et al.*, 2005].

2.2.1 Onshore structure

The southeastern part of the South Wanganui Basin is bounded by recently uplifted (last 2 Ma) greywacke basement rock of the Tararua and Ruahine mountain ranges [Lamb and Vella, 1987], while offshore reverse faults in the Kapiti-Manawatu Fault System (figure 2.4) control the subsidence of the basin [Lamarche *et al.*, 2005]. The Tararua Ranges form the southern part of the North Island Axial Range and are characterised by high shear strain associated with the oblique convergence of the Australian and Pacific plates. The shear stress is being released by dextral strike-slip motion on faults along the axial ranges and their margins. Faulting between the axial ranges and the coast is masked beneath the coastal floodplain. Here the basement is sharply folded into anticlines and synclines which run parallel to the Axial Ranges [Te Punga, 1957]. The region is cut by a series of near-parallel, north-northeast trending strike-slip faults [Anderton, 1981].

Levin area

Geological and geophysical surveys [Anderton, 1981] and gravity surveys [Bekesi, 1989] have found the basement to be shallow, less than 1500m below sea level, and gradually deepening to the northwest away from the Tararua Ranges. The only recognised buried basement structure is the Poroutawhao High [Te Punga, 1953], an elongated structure trending north-northeast which lies north of Lake Horowhenua and is bounded to the east by a high angle fault (figure 2.4). There are also two known anticlines south of the Manawatu River, the Levin and Shannon anticlines. The Levin anticline is

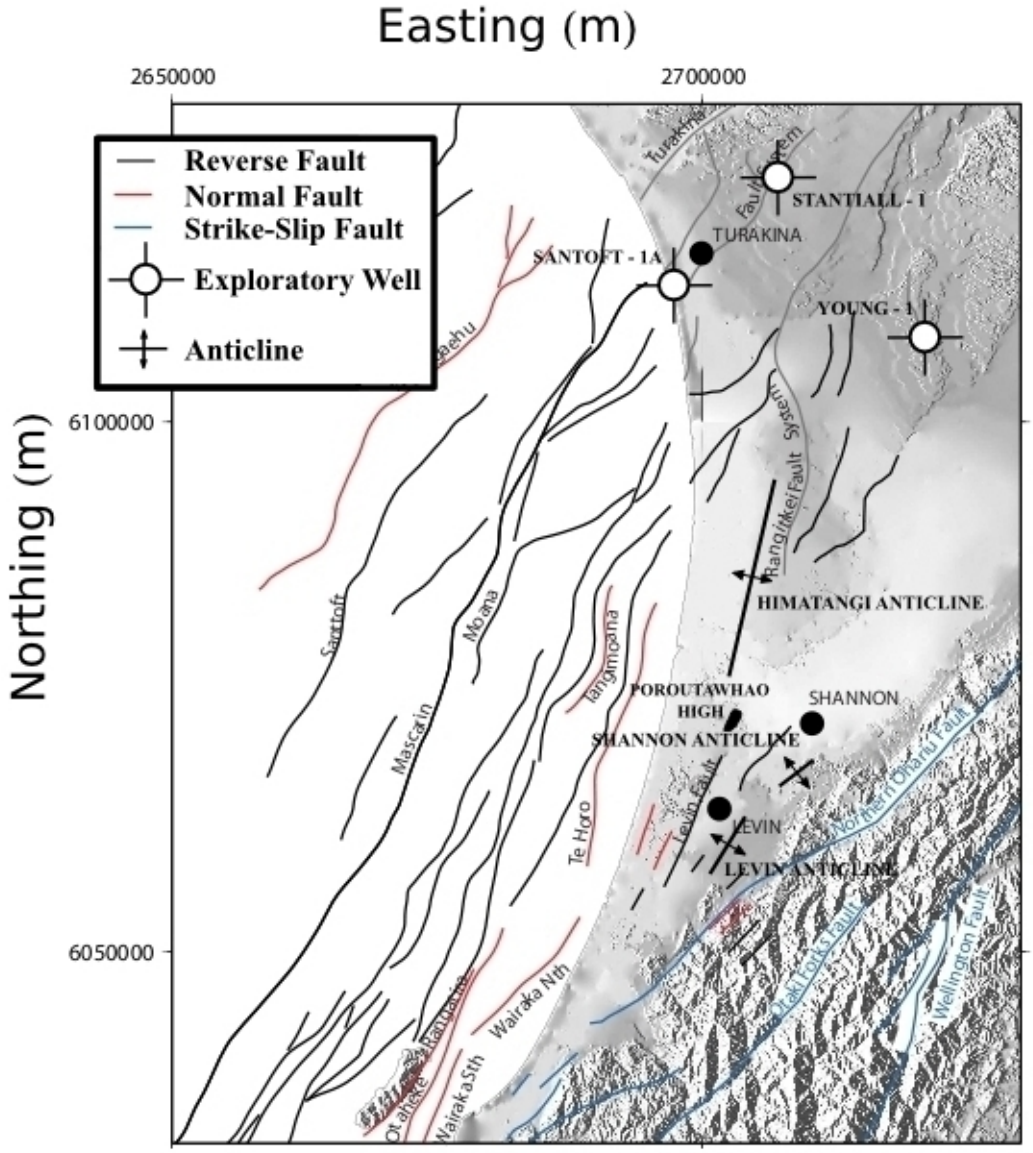

Figure 2.4: Map showing the location of mapped faults, anticlines and exploratory oil wells in the southeastern corner of the South Wanganui Basin. The offshore faults are collectively known as the Kapiti-Manawatu Fault System (KMFS) [Lamarche *et al.*, 2005]. Reproduced from Ewig [2008]. Scale is in New Zealand Map Grid (NZMG).

6 km long and trends northeast while the Shannon anticline is 3 km long and trends east-northeast. Gravity surveys show only a slight distortion of the regional Bouguer anomaly (-3 mGal) over the Poroutawhao High and no significant changes over the Levin and Shannon anticlines [Bekesi, 1989].

Himatangi area

The Himatangi anticline lies between Foxton and Rongotea, trends north-northeast and is 20 km long. A gravity survey indicates the presence of a basement high trending north-northeast underlying the Himatangi anticline [Hunt, 1980]. Three exploratory oil wells were drilled on buried basement highs and reached basement rock at the following depths below the surface: Santoft 1A; 2633m, Stantiall 1; 2098m, Young 1; 1035m (figure 2.4).

2.2.2 Kapiti-Manawatu Fault System

The Kapiti-Manawatu Fault System (KMFS) is a major contractional fault system that runs north-northeast parallel to the Axial Ranges (figure 2.4) [Lamarche *et al.*, 2005; Nodder *et al.*, 2007]. The KMFS has accommodated $\approx$ 3.5 km of basement throw over the last 3 Ma and controls the subsidence of the South Wanganui Basin [Lamarche *et al.*, 2005]. Cumulative vertical displacement of 3500 m across the KMFS combined with a further 200 m associated with reverse faulting between the coast and the foot of the Axial Ranges results in 3700 m of vertical separation. However, there is a measured 5000 - 7000 m elevation difference between the top of the Axial Ranges and the basement floor of the South Wanganui Basin. Distributed deformation

in small structures probably accounts for the remaining 1300 - 3300 m of separation [Lamarche *et al.*, 2005].

Lamarche et al. [2005] found that the KMFS faults are kinematically dependent and that individual faults acquired their length early in the history of the fault system. They also proposed that the faults were originally extensional normal faults which have reactivated in the last 1.8 Ma as reverse structures. The age of the formation of these faults is not known, but it probably predates the formation of the Wanganui Basin and probably occurred during a widespread extensional phase in New Zealand during the late Cretaceous to early Eocene [Lamarche *et al.*, 2005]. Two of the faults in the KMFS, the Mascarin and the Rangitikei faults, may extend to depth and link with the subducted Pacific plate [Nodder *et al.*, 2007].

2.2.3 Stratigraphy

Because the South Wanganui Basin formed in the north and its depocentre migrated southeast over time (figure 2.1), only the youngest formations found within the basin are deposited onshore at the southeastern edge. Greywacke and schist basement rock underlies the entire area and outcrops in the Tararua Ranges [Anderton, 1981]. The outcropping greywacke rocks are strongly deformed sedimentary strata consisting of sandstone and siltstone in alternating sequences with rare limestone and red volcanic bands [Bekesi, 1989].

The coastline of the South Wanganui Basin is constantly changing owing both to tectonic uplift and subsidence of the basin, and to sea level change

due to glacial-interglacial cycles. Also the uplift of the Axial Ranges in the last 2 Ma has caused the deposition of large quantities of fluvial deposits across the coastal plain. Because of this active environment the onshore area of the South Wanganui Basin has many closely interspersed layers of fluvial sands, coastal dune sands and peat layers. Coastal dune sands and fluvial sands can be distinguished by the mean roundness of the grains and the percentage of heavy minerals present by weight [Shepard, 1985].

The Koputaroa Dune Phase was active near Levin during late Pleistocene time, and grain analysis indicates a marine rather than fluviate source. A problem with this interpretation is that these dunes were active during the last stadial of the Otira Glaciation, a time when global sea level was 100 m lower than at present, so the shoreline was probably located at least 30 km to the west. The present-day prevailing westerly winds along the Manawatu coast are strong enough to initiate sand transport approximately 33 percent of the time, so assuming a dune migration rate of 10-30 m/year it is entirely possible that these dunes could have formed during this time and migrated to their current location [Shepard, 1985]. Dune migration rates are influenced not only by wind speed but also by the nature of the vegetation covering the surface over which the dune advances [Shepard, 1985].

During the Holocene epoch, a period of estuarine deposition initiated by the Postglacial Transgression was succeeded by a phase of fluvial deposition which dominated subsequent development [Shepard, 1987]. The boundary of the estuary once lay as far inland as Shannon, and began infilling approximately 6000 years B.P. leaving behind an alluvial plain. Sand dunes migrating inland from the coast left thin eolian veneers in their wake mantling the

flood-plain surface [Shepard, 1987]. Cowie [1963] identified and described three distinct surges of dune activity during the Holocene. Floods then inundated the low sandy plain, depositing a thin layer of alluvium which impeded drainage. Swamps and forests then became established on the plain enabling a layer of peat to accumulate.

2.2.4 Biogenic gas accumulation

Five exploration wells have been drilled in the onshore South Wanganui Basin area in the last 70 years, all of which reached basement and were found to be dry. This area has, however, demonstrated a propensity for forming shallow gas deposits with numerous shows of methane-rich gas in shallow water wells throughout the region. This gas is likely to be of biogenic origin as there is a lack of evidence for hydrocarbon source rocks of sufficient burial depth and maturation for the production of thermogenic gas within the South Wanganui Basin. Biogenic gas is produced when archeobacteria called methanogens metabolise organic material in an anoxic environment. The rapid subsidence of the area has allowed the formation of multiple peat layers and lignite lenses capable of generating biogenic gas. Sand dunes migrating across the region have become buried and form possible stratigraphic traps for gas, and the presence of many vertical faults in the area provides a method of gas migration. The confirmed presence of gas in water wells together with the known stratigraphy and depositional environment indicate that there are likely to be many shallow pockets of biogenic gas across the onshore South Wanganui Basin area. Assuming that biogenic gas is generated in sufficient quanti-

ties, the shallow structure in this region should provide excellent widespread possibilities for migration and trapping.

Chapter 3

Shallow gas

3.1 Biogenic gas

There are two types of gas found in the earth: thermogenic and biogenic. More than 20% of known gas reserves globally are considered to be of biogenic origin [Li and Lin, 2010]. Interest in shallow biogenic gas has been rising in recent years. This is demonstrated by an increase in survey expenditure. Shallow biogenic gas has been shown to occur widely, accumulate in commercially significant quantities, and be relatively cheap to extract [Li and Lin, 2010].

In hydrocarbon generation there are three main stages of thermal maturity for organic matter in sediments. In the immature stage biogenic gas is generated by microbial action either through acetate fermentation or carbon dioxide reduction on organic matter [Premchitt *et al.*, 1992, Dang *et al.*, 2008]. During the immature stage methane and other gases are produced with only very small amounts of higher hydrocarbons. In the mature stage

increasing burial depth, temperature and time produce a wider range of hydrocarbons. These higher hydrocarbons begin to degenerate into methane during the postmature stage. The gas formed in the immature stage is biogenic gas while the gas formed in the postmature stage is thermogenic gas. Biogenic gas can form in both saline and fresh water environments [Premchitt *et al.*, 1992].

Biogenic gas often occurs in flood-plain, estuarine or shallow marine environments and is preserved in stratigraphic traps. Sand lenses commonly serve as gas reservoirs, while overlying impermeable clay or mud beds serve as seals. Sandstone permeability can be up to two orders of magnitude greater than that of mudstone beds and the porosities of sand lenses range from 30% to 50% [Dang *et al.*, 2008, Li and Lin, 2010].

3.2 Detection methods

Biogenic gas deposits tend to have a scattered distribution. Most reservoirs are typically of single-bed thickness (1-3m) that may be stacked vertically to produce larger deposits with high vertical heterogenity and good horizontal connectivity [Dang *et al.*, 2008]. Owing to the method of their formation most biogenic gas deposits are at shallow burial depths and low pressure. Because of these attributes conventional exploration methods are too expensive to be used for shallow gas prospecting [Li and Lin, 2010]. Shallow gas exploration is most likely to be successful if a combination of methods is used.

For the initial exploration of a large area, cone penetration tests (CPT's), microbiological, resistivity and radon anomaly surveys can be used to con-

firm the presence and location of shallow biogenic gas deposits. The choice of which of these methods to use is dependent on accessibility of the area, budget, geological setting and stratigraphy. The lithology and anticipated gas-bearing structures in the study area will influence which methods of detection will be most suitable. Once a potential gas reservoir has been located, the next step is to determine the depth and boundaries of the structure as well as the lithological units involved. Resistivity surveys can image the top surface of gas-charged bodies. Shear wave seismic profiles can be used to locate strong reflections from the top of gas-bearing sand bodies and identify their edges. Edges of shallow gas bodies can also be mapped by radon anomaly surveys, and CPT's can be used to enlarge a known gas field [Li and Lin, 2010].

3.2.1 Active source seismology

Sedimentary sequences are made up of rock with a porosity that can approach 50% [Dang *et al.*, 2008]. This pore space is usually filled with water. Shear waves cannot propogate through liquid, so they travel through the sediment frame alone and shear wave velocity increases with depth as the overburden pressure increases [Gardner *et al.*, 1974]. In contrast compressional waves are carried by both the sediment frame and the pore fluid, so compressional wave velocity is controlled by the volume fraction of gas within the pore space. Water has a higher compressional wave velocity than gas, so as gas replaces water in the pore space the compressional wave velocity of the rock will decrease and its acoustic properties will change [Yuan *et al.*, 1992]. Since

compressional wave velocity decreases with increasing gas content, in some cases it will be possible to estimate the overall gas volume from the velocity change [Missiaen *et al.*, 2002].

The strong seismic reflection feature at the top of gas-bearing bodies declines sharply as the body ends. This allows the edges of gas-bearing bodies to be mapped using seismic reflection profiles. The land seismic method requires extensive field work and data processing, so is not useful for exploration of large areas; but it is useful for determining the extent of an already located gas body. Shallow onshore gas deposits are a natural laboratory that provides the opportunity to study the seismic effects of gas in a testable environment.

Amplitude variation with offset

Amplitude Variation with Offset (AVO) is a commonly used method of gas detection in seismic surveys. At a boundary between two isotropic, homogeneous elastic media, an incident compressional plane-wave will split into four waves: reflected P-wave, reflected S-wave, transmitted P-wave and transmitted S-wave (figure 3.1). The angles of reflection and refraction are governed by Snell's law:

$$\frac{sin\theta_1}{sin\theta_2} = \frac{V_1}{V_2} \tag{3.1}$$

where V_1 and V_2 are the velocities in the first and second layers, θ_1 is the angle of incidence and θ_2 is the angle of refraction.

The reflection coefficients at such a boundary are governed by Poisson's

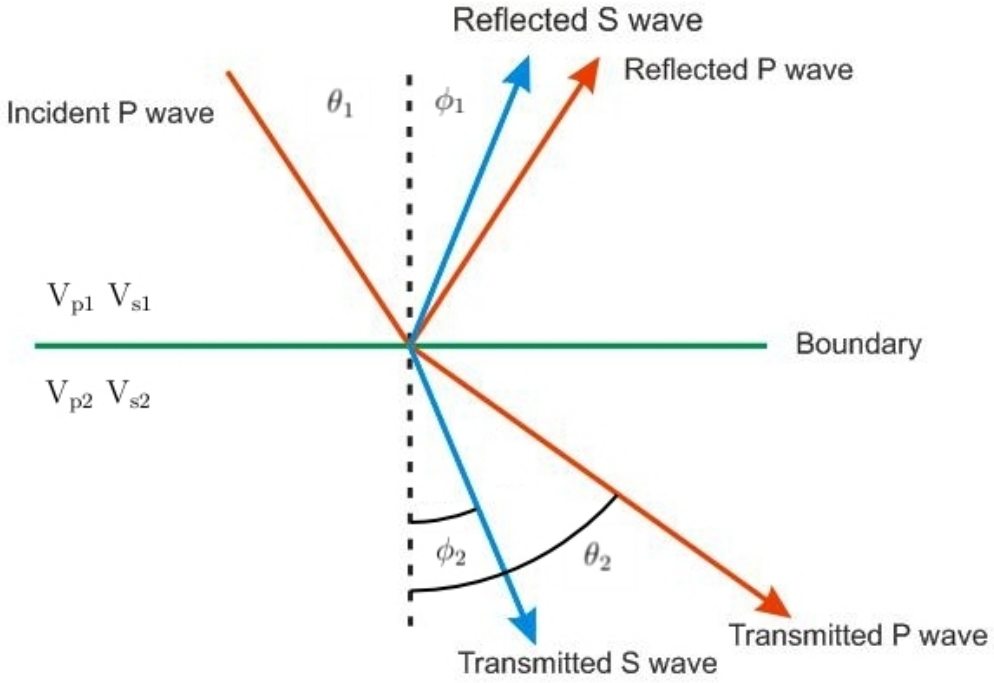

Figure 3.1: Diagram showing the splitting of a compressional plane wave at the boundary between two media with different V_p and V_s. The angles of reflection and refraction are calculated from the angle of incidence and the velocities of the two media using Snell's law.

ratio (σ) and density (ρ) in the two media and the angle of incidence. P-wave velocity (V_p), S-wave velocity (V_s) and density (ρ) depend on the lithology, porosity, pore fluid and pressure of the medium. Poisson's ratio (σ) for a material describes how its volume changes under compressional force. In an isotropic, elastic material Poisson's ratio is related to the P-wave (V_p) and S-wave (V_s) velocities of the material.

$$\sigma = \frac{(V_p/V_s)^2 - 2}{2[(V_p/V_s)^2 - 1]} \tag{3.2}$$

Poisson's ratio varies from 0.0 to 0.5 in common isotropic materials, with

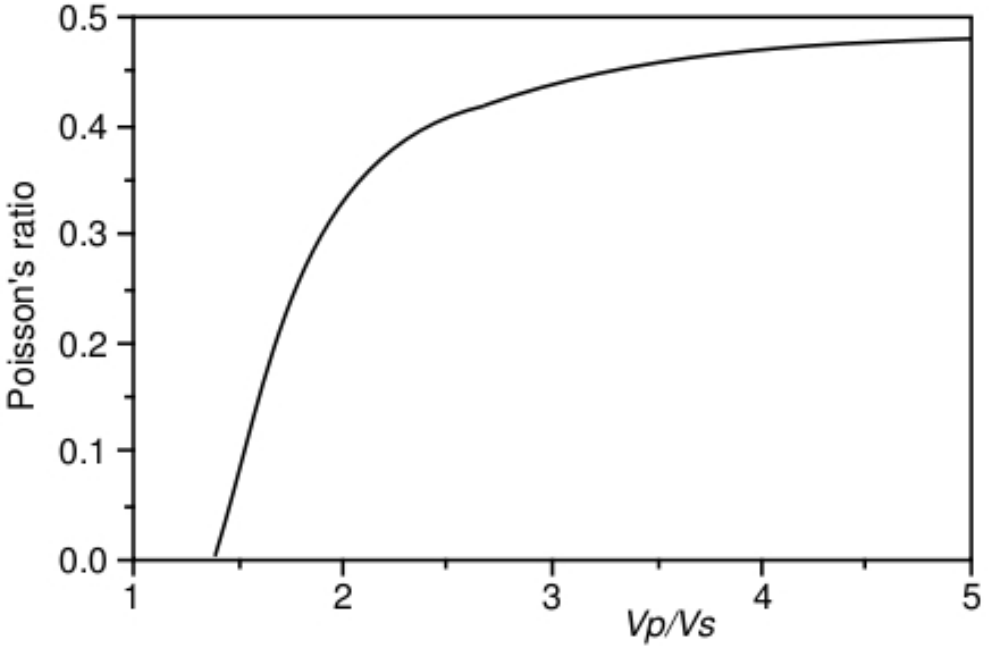

Figure 3.2: Plot showing the change in Poisson's ratio with change in V_p/V_s for an isotropic elastic medium. Reproduced from Ostrander [1984].

incompressible materials such as liquids having a Poisson ratio of 0.5. High porosity gas sands tend to exhibit abnormally low Poisson ratios. Typical shallow marine sediments have a Poisson ratio of 0.45 - 0.50 while gas saturated sediments have a Poisson ratio of 0.02 - 0.14 [Ostrander, 1984]. The presence of gas in pore space causes a strong drop in V_p and a small increase in V_s. This reduces V_p/V_s and consequently Poisson's ratio (figure 3.2). Less than 5% gas saturation is required to produce a significant drop in V_p (figure 3.3) [Ostrander, 1984].

Zoeppritz [1919] investigated the reflection coefficient at differing angles of incidence for a plane wave at a boundary between two media. An approximation to the P-P reflection coefficient of the Zoeppritz equation assuming

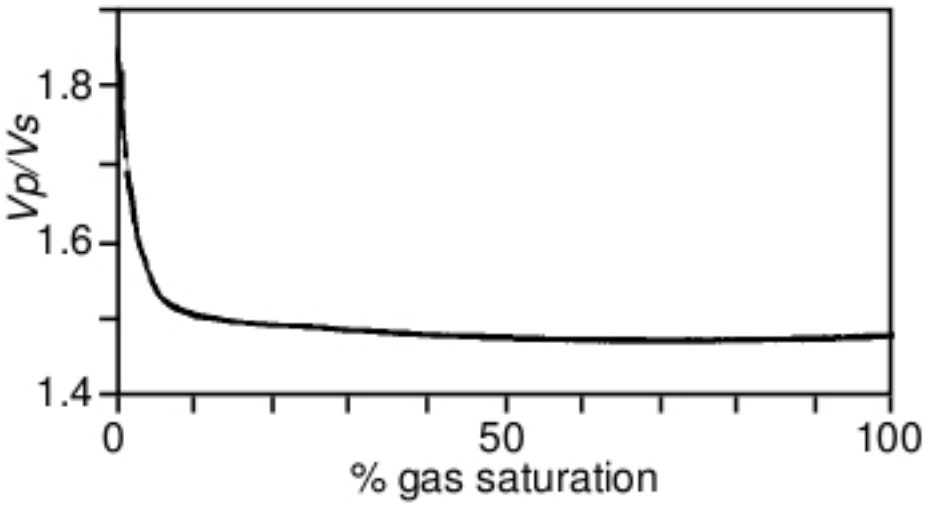

Figure 3.3: Plot showing change in V_p/V_s with change in % gas saturation in the pore space of a medium. Reproduced from Ostrander [1984].

relatively small changes in medium properties is provided by Shuey [1985]:

$$R_{pp}(\theta) = R_0 + (A_0 R_0 + \Delta\sigma/(1-\sigma)^2) sin^2\theta + \frac{1}{2}\frac{\Delta V_p}{V_p}(tan^2\theta - sin^2\theta) \quad (3.3)$$

where R_0 = reflection coefficient, σ = Poisson's ratio, θ = angle of incidence,

$$\Delta V_p = V_{p2} - V_{p1}, \quad (3.4)$$

$$V_p = (V_{p1} + V_{p2})/2, \quad (3.5)$$

$$A_0 = B_0 - 2(1 + B_0)[\frac{1-2\sigma}{1-\sigma}], \quad (3.6)$$

$$B_0 = (\Delta V_p / V_p)/[\frac{\Delta V_p}{V_p} + \frac{\rho_2 - \rho_1}{(\rho_1 + \rho_2)/2}]. \quad (3.7)$$

Given the P-wave velocity, S-wave velocity and density in two media, Zoeppritz's equations predict the reflection and transmission coefficients at the interface. Ostrander [1984] calculated the theoretical behaviour of P-P reflection coefficients at a media boundary, varying the velocity and Poisson's ratio contrasts over a range of incidence angles (figure 3.4).

An interface between sediments with a high Poisson's ratio overlying gas-charged sand with a low Poisson's ratio should result in an increase in reflected P-wave energy at wider angles of incidence [Ostrander, 1984]. This is shown in figure 3.4, case **(d)**, where $V_{p1} > V_{p2}$ and $\sigma_1 > \sigma_2$ results in an increase in the absolute reflection coefficient with increasing angle of incidence. If there is no gas present then Poisson's ratio is unlikely to change significantly, leading to results like cases (a) and (b) (see figure 3.4), where the absolute reflection coefficient decreases slightly with increasing angle of incidence.

Acoustic turbidity and blanking

When the acoustic pulse from a seismic source passes into gas-charged sediments, absorption and scattering of the pulse occurs. This causes a drop in sonic velocity, attenuating and absorbing the returning signal, and appears on seismic profiles as a zone of disruption of the continuity of reflectors within and beneath it. This so-called acoustic turbidity often cuts sharply across stratigraphy and is an indicator that it is probably not related to the

lithology [Missiaen *et al.*, 2002]. Diffractions related to gas horizons also can be visible on seismic records. These can be caused by irregularities in the morphology due to the presence of gas, such as doming (figure 3.5).

Acoustic turbidity can make it hard to determine the thickness of a gas-charged layer by masking seismic reflections from the base of the layer. Gas content below saturation in reservoir rock is capable of producing acoustic turbidity in seismic surveys, so the presence of acoustic turbidity or blanking is not an indication of the amount of gas present [Premchitt *et al.*, 1992].

3.2.2 Resistivity

Resistivity surveys can be used to investigate subsurface structure and stratigraphy. An electrical direct current is applied between two electrodes implanted in the ground. The difference in electric potential is then measured between two additional electrodes that do not carry any current. Mineral grains are essentially non-conductive so the resistivity of soil or rock is governed primarily by the amount of pore water, its composition and the arrangement of the pores. Data from resistivity surveys are interpreted in the form of apparent resistivity ρ:

$$\rho = U\frac{2\pi r}{I} \tag{3.8}$$

where ρ = the resistivity of the medium, U = the potential in Volts at distance r from the electrode, r = distance from the electrode, and I = current.

High salinity lowers the electrical resistivity of water while gas-charged sediments have high resistivity due to water being replaced by gas in the pore

space. The electrical resistivity difference between gas- and water-saturated bodies allows the identification of gas sands (figure 3.6) [Li and Lin, 2010]. The thickness of the gas-bearing layer and the resistivity difference between gas- and water-saturated layers will affect how evident shallow gas deposits appear on resistivity curves.

Resistivity surveys are low-cost and can be used in prospecting a large area, both to initially identify gas-bearing zones and subsequently to determine their size. Different survey geometries measure resistivity at different depths in the subsurface so it is possible to roughly determine the depth and thickness of gas-bearing zones [Li and Lin, 2010]. Drawbacks of resistivity surveys are that they must be conducted in areas with minimal electrical interference from other sources, and any depths obtained will have high margins of error.

3.2.3 Other methods of shallow gas detection

Cone penetration test

A Cone Penetration Test (CPT) can be used to collect lithological data on shallow unconsolidated near-surface sediments. A CPT is a low-cost and repeatable method of profiling the subsurface, providing high-resolution logs of vertical grain-size variation which can be used to confirm the depths of sedimentary successions (figure 3.7) [Tillmann *et al.*, 2008].

A cone penetration testing tool consists of a conical tip which measures the soil mechanical resistance to penetration per unit area, a friction sleeve which measures the friction of the sediments along the tool (both measured

in MPa) and electrodes which measure the electrical resistivity (Ω m). The cone is pushed downwards into the sediment at a constant rate of 2 cm/s and is limited to a depth of 90 m. Once the cone penetration testing tool is removed, a probe can be lowered down the hole to log the natural gamma activity, gamma-gamma activity and neutron activity (counts per minute). These measurements can be related to clay content, bulk modulus (kg/m^3) and water content [Tillmann *et al.*, 2008].

By taking a core sample and CPT at the same location, the CPT can be calibrated to distinguish the lithology of known strata. Since CPT's are quick and cheap to perform, once calibrated they can be used to correlate strata depths across a large area. Another advantage of CPT's is that if gas is present then it will be emitted from the hole after drilling. Unfortunately CPT's are not suitable in areas with gravel beds, as the cone tip cannot penetrate beds with more than 30% gravel. Also if gas is present in several sand lenses, the CPT cannot determine which lens the gas originated from [Li and Lin, 2010].

Soil-gas radon analysis

Radiation levels over oil and gas fields have often been shown to be higher than background levels, with high radioactive anomalies found over the edges of fields (figure 3.8). This is due to radon content being enriched within hydrocarbon fields. Ultra-small bubbles of light hydrocarbons escape through the hydrocarbon-water contact at the edges of oil and gas fields, then water rich in radon is vertically migrated up fracture zones by pressure and temperature differences forming the surface radon anomaly [Saunders *et al.*, 1993,

Li and Lin, 2010].

Soil-gas radon surveys are a quick and economic method of predicting the location of shallow biogenic gas accumulations. Data can be affected by tectonic and geochemical properties of the area as well as groundwater distribution. This method works best in areas with high levels of radioactive materials such as uranium and thorium. Soil-gas radon surveys can reveal only the probable presence of hydrocarbons without giving any information about the depth or volume of the reservoir. Another problem with this method is that once an abnormal peak has been located, if the anomaly intensity is equal on both sides of the peak it is difficult to determine on which side the gas-bearing reservoir lies.

Microbiological exploration

Certain bacteria have the ability to oxidize methane, ethane and propane. Detecting the presence and concentration of these bacteria in the soil can be used to ascertain the presence and extent of deeper hydrocarbon accumulations (figure 3.9). Microbiological exploration is a rapid and economically viable method of exploration for oil and gas. However, like soil-gas radon surveys, it can determine only the lateral extent of oil or gas and not the depth or thickness of the reservoir. Because of this limitation microbiological exploration should be used in conjunction with other geophysical prospecting methods to reduce the exploration risk [Li and Lin, 2010].

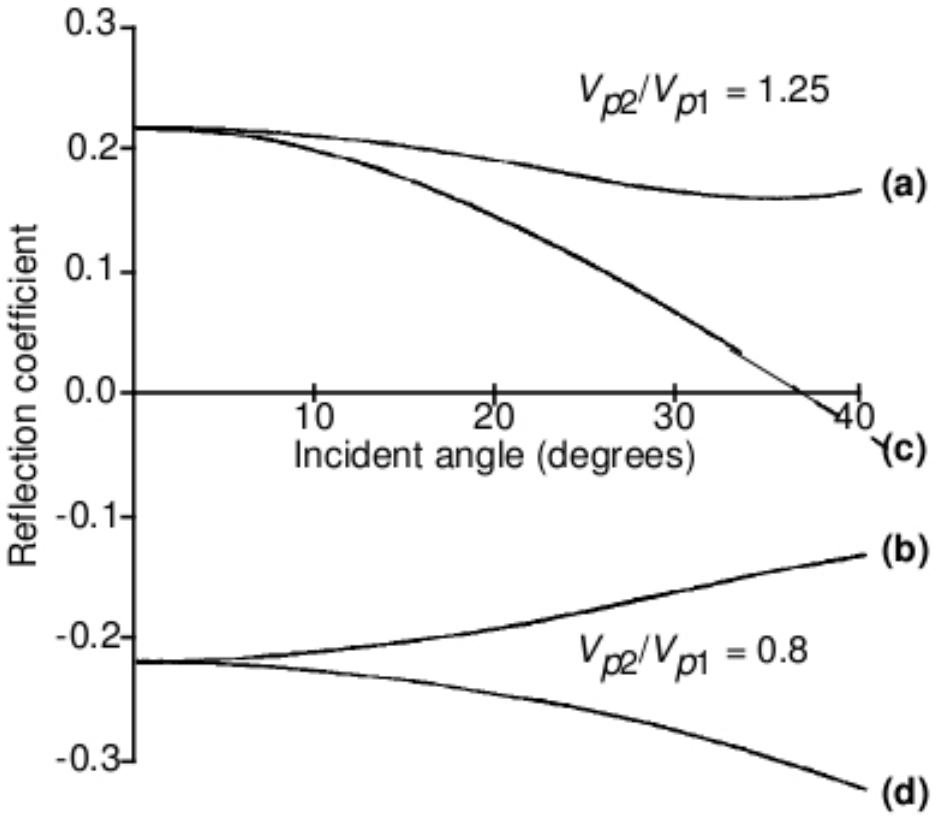

Figure 3.4: Plot showing change in the predicted reflection coefficient (from Zoeppritz equations) with increasing incidence angle for four different scenarios: **(a)** V_{p2} / V_{p1} = 1.25, $\sigma_1 = \sigma_2 = 0.3$, **(b)** V_{p2} / V_{p1} = 0.8, $\sigma_1 = \sigma_2 = 0.3$, **(c)** V_{p2} / V_{p1} = 1.25, $\sigma_1 = 0.4$ $\sigma_2 = 0.1$, **(d)** V_{p2} / V_{p1} = 0.8, $\sigma_1 = 0.4$ $\sigma_2 = 0.1$. The sign of the reflection coefficient determines the polarity of the observed signal while the absolute reflection coefficient determines the amplitude of the observed signal. Reproduced from Ostrander [1984].

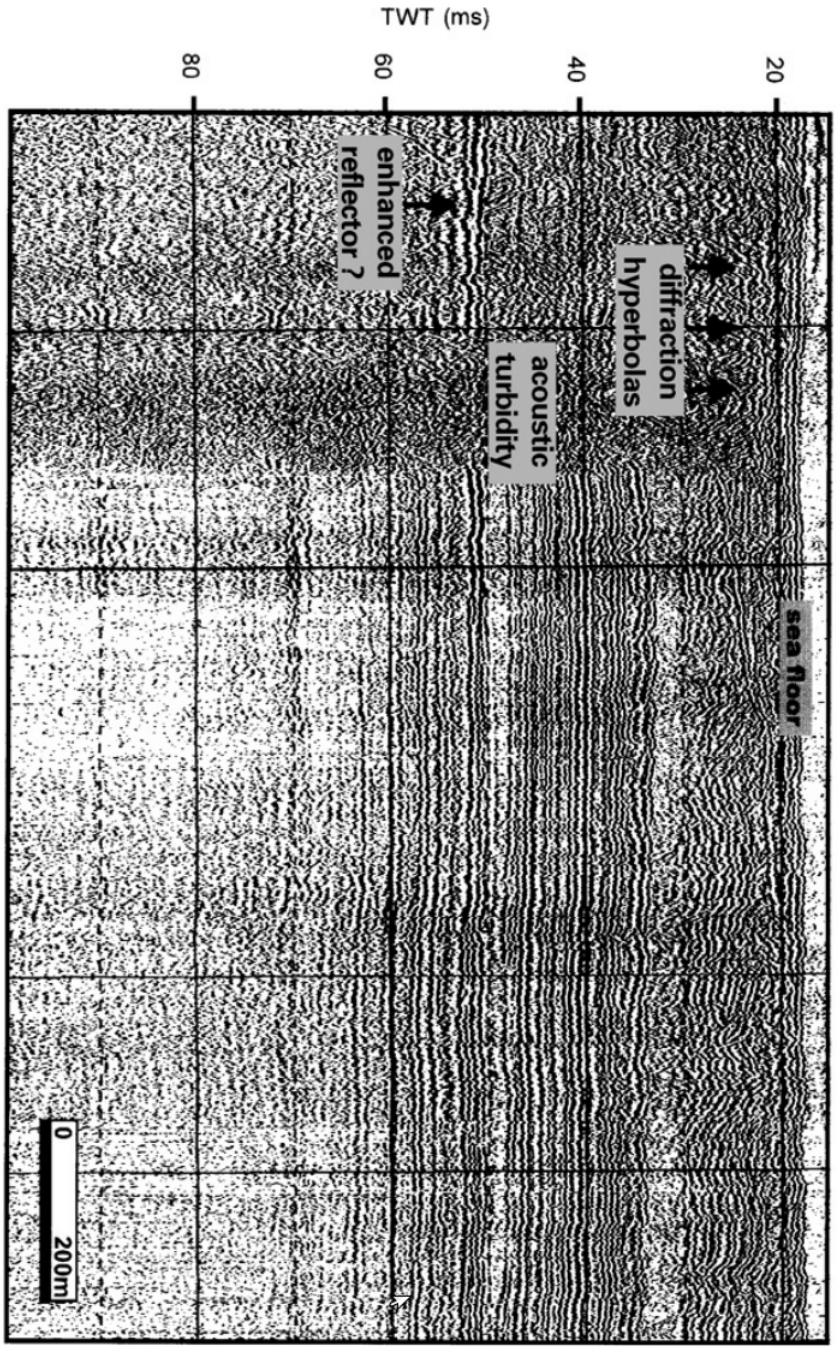

Figure 3.5: Analogue boomer profile showing zones of acoustic turbidity cutting across the stratification. Note how the turbidity disrupts reflectors and stops at the level of the diffraction hyperbolas rather than reaching the sea floor. The high amplitude of the reflector at the left is possibly gas-related. Reproduced from Missiaen *et al.*, [2002].

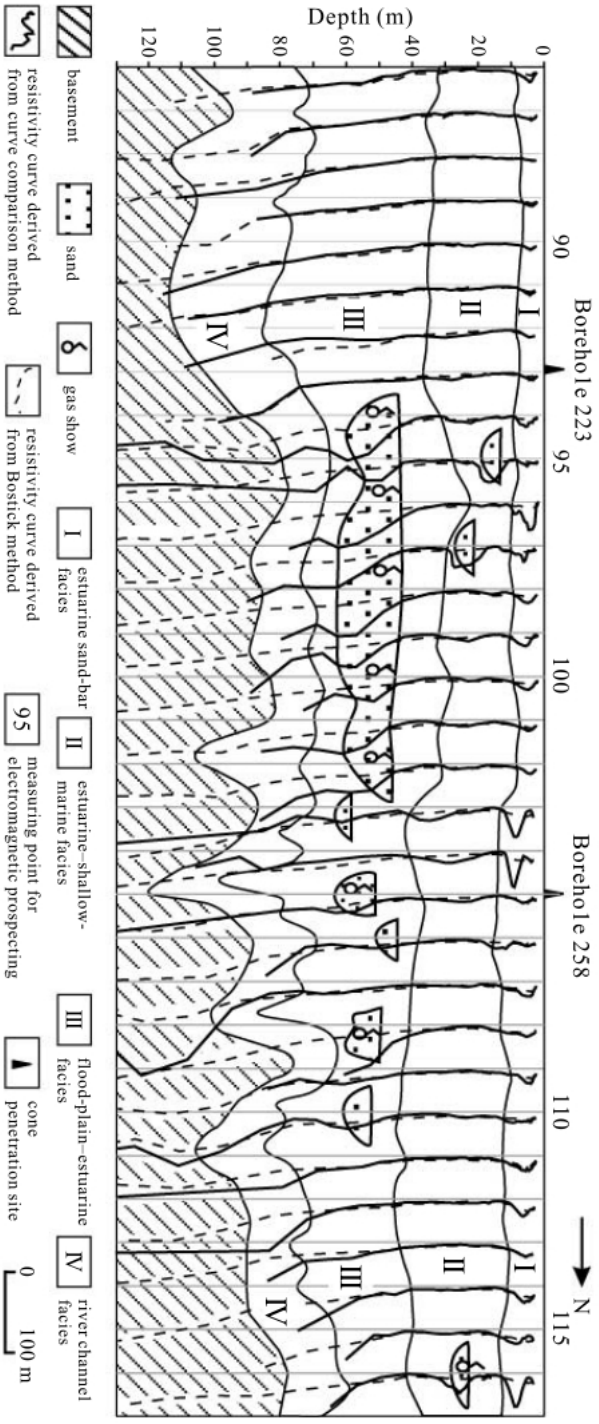

Figure 3.6: Resistivity-depth profile defining the distribution of gas-bearing sand bodies, survey line XW-1 in the Xinwan, Hangzhou Bay area, eastern China. Reproduced from Li and Lin, [2010].

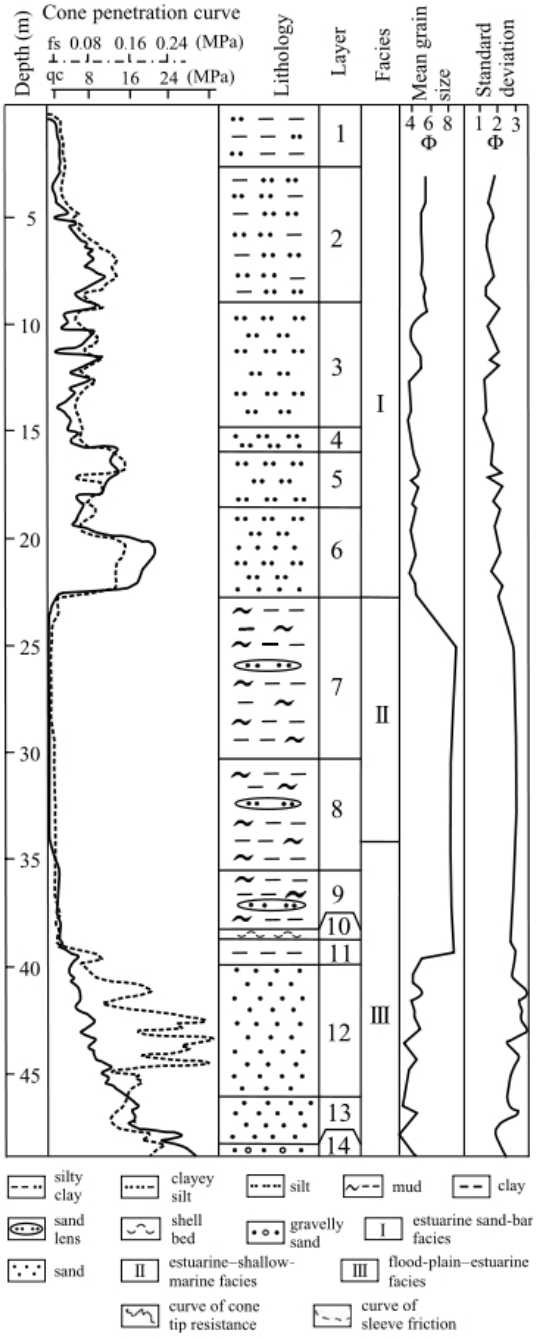

Figure 3.7: Cone penetration borehole log from the Hangzhou Bay area, eastern China. qc = cone tip resistance and fs = sleeve friction. Reproduced from Li and Lin, [2010].

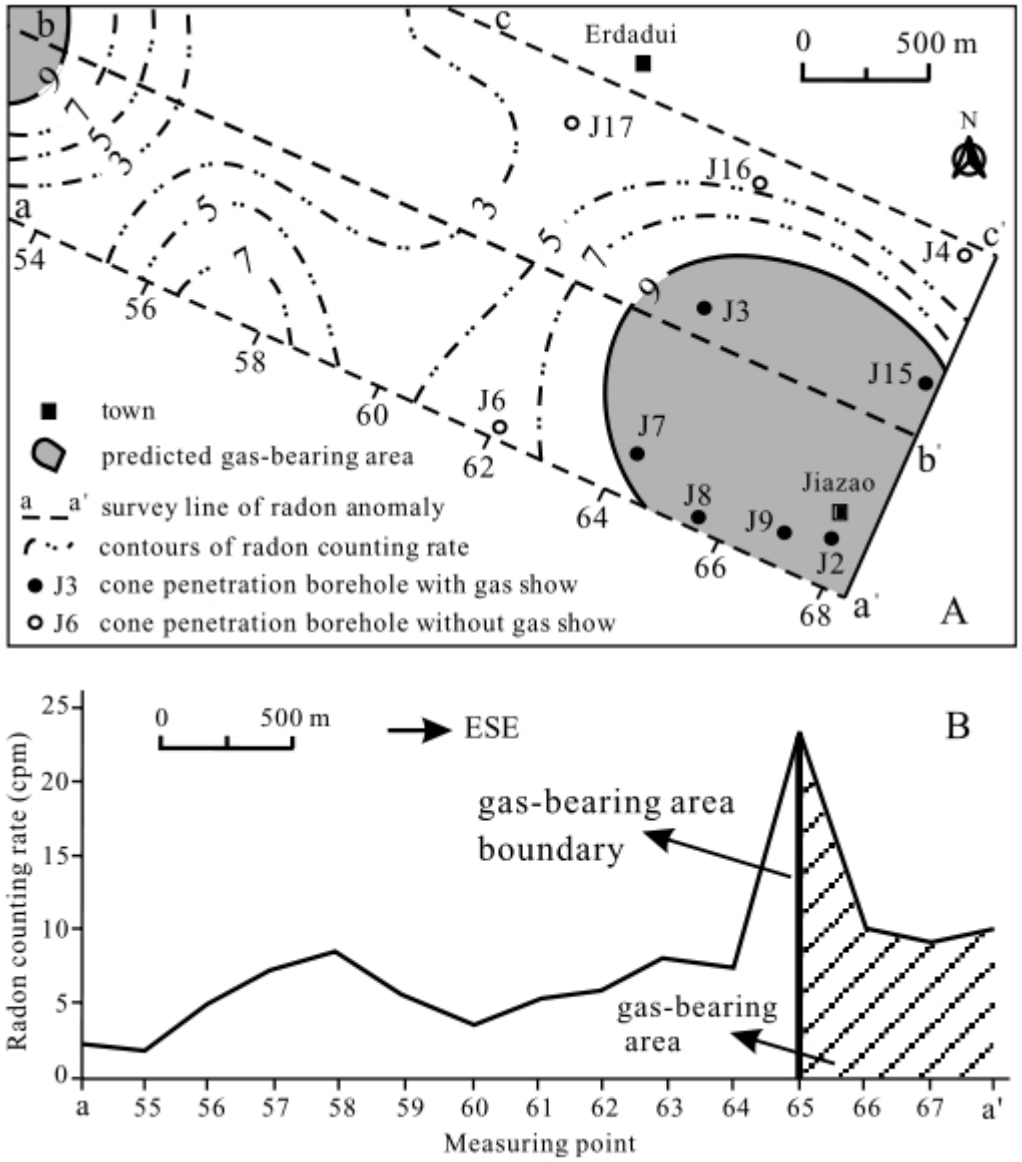

Figure 3.8: Radon anomaly in Hangzhou Bay area, eastern China. (A) Shows radon survey lines over Jiazao shallow gas field. (B) Shows radon anomaly profile (aa'). cpm = counts per minute. Reproduced from Li and Lin, [2010].

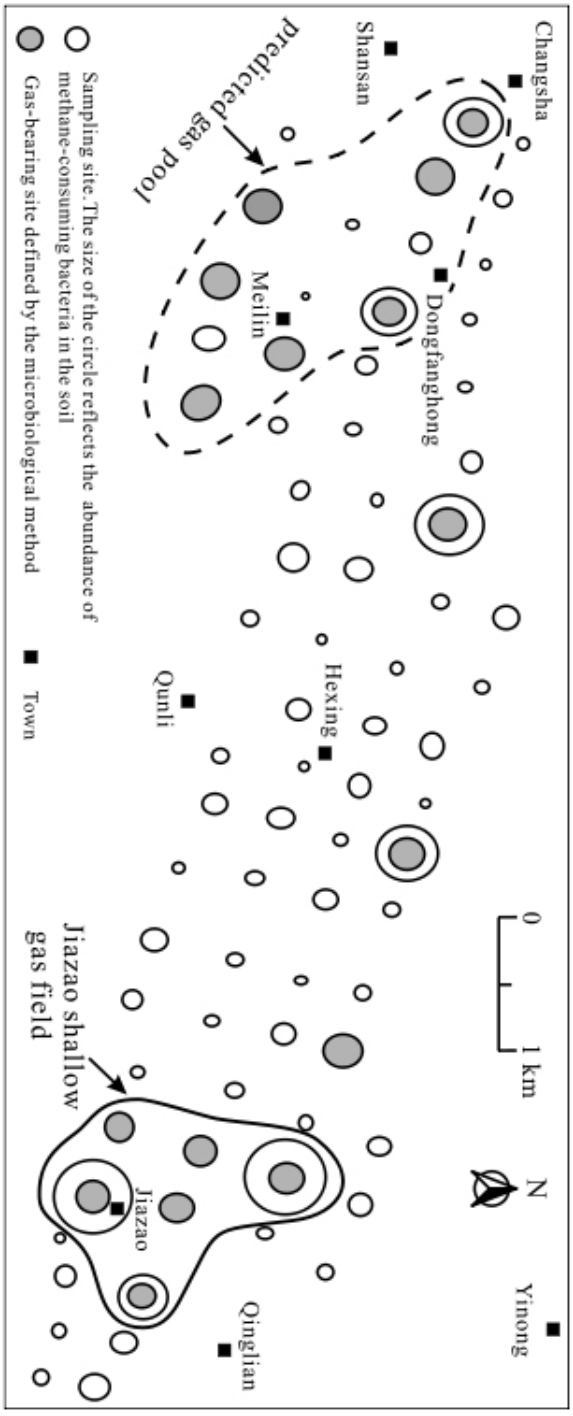

Figure 3.9: The distribution of methane-consuming bacteria *Flavobacterium, Bacillus, Acinetobacter, Xanthomonas,* and *Pseudomonas,* in the Jiazao region in Hangzhou Bay area, eastern China. Reproduced from Li and Lin, [2010].

Chapter 4

Muhunoa East Road – Basement depth survey

The Tararua Ranges are formed of greywacke basement rock that is bounded to the west by a series of strike-slip faults and becomes buried beneath the sediments of the Manawatu plains until it is at a depth of approximately 1.5 km beneath Levin [Bekesi, 1989]. The Northern Ohariu Fault, which has predominantly dextral strike-slip motion, cuts through the Tararua range front near Muhunoa East Road. At semi-regular intervals the boundary of the Tararua range front steps laterally, potentially forming pull-apart basins. One such basin possibly lies to the south of Muhunoa East Road (figure 4.1).

Seismic and gravity profiles were collected and interpreted along Muhunoa East Road by Aharoni [1991]. The seismic profile was reprocessed and the gravity dataset remodelled by Ewig [2008] (figures 4.2, 4.3). The reprocessing of the Muhunoa East Road seismic profile by Ewig [2008] revealed a reflected arrival at the eastern end of the line near the Tararua range front (figure 4.2,

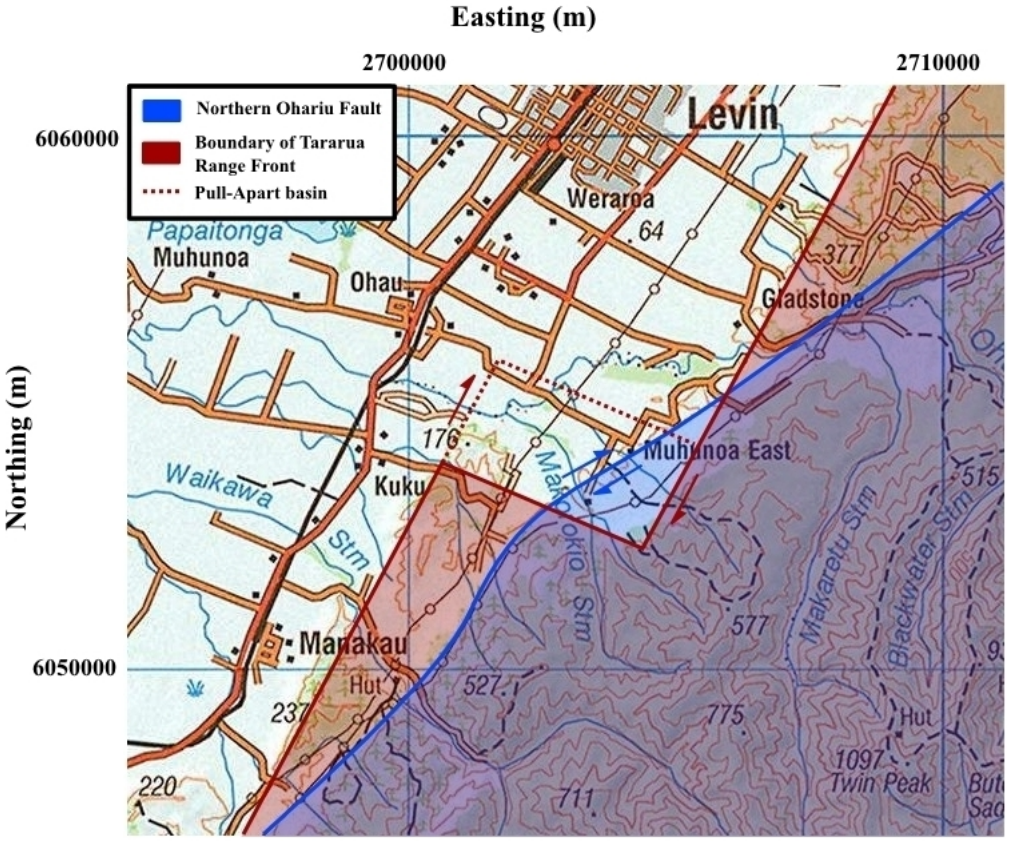

Figure 4.1: Map of Muhunoa East Road study area south of Levin showing the surface trace of the Northern Ohariu Fault, the step in the boundary of the exposed greywacke basement of the Tararua range front and the location of the potential pull-apart basin. Scale is in New Zealand Map Grid (NZMG), squares are 10 km.

grey dashed line) which was deeper than the accepted basement depth (purple dashed line). The basement depth from the reprocessed seismic line (figure 4.2) was confirmed by the remodelled gravity profile (figure 4.3). This intra-basement reflector could be the result of either side-swipe from a steeply dipping basement structure to the south where the Tararua range front steps laterally, or an intra-basement low-angle thrust fault.

Palmer [1993] identified a series of thrust systems at the eastern margin of the Taranaki Basin formed by reverse movement along the Taranaki Fault Zone. This motion commenced during the late Eocene and continued to the Pliocene with major movement during the Miocene. A number of similar low-angle intra-basement reflections are visible on seismic lines across the South Wanganui Basin. These were investigated by Ewig [2008] who provided two possible explanations. As in the Taranaki Basin these reflections could be interpreted as low-angle thrust faults that resulted from 75±35 km of shortening during the Miocene across the Taranaki and Wanganui basins due to plate convergence [Stern *et al.*, 2006; Nicol *et al.*, 2007]. Alternatively if a seismic line runs subparallel to the trend of nearby steeply-dipping faults then side-swipe from the surrounding faults could appear as intra-basement reflections on that seismic line [Ewig, 2008].

In the case of the Muhunoa East Road seismic line, if a pull-apart basin has formed at the step in the Tararua range front then the intra-basement arrival (figure 4.2, grey dashed line) could be side-swipe from a faulted and steeply dipping basement structure to the south. Alternatively the intra-basement arrival could be a reflection from a low-angle thrust within the greywacke basement. The aim of this survey was to resolve this fundamental

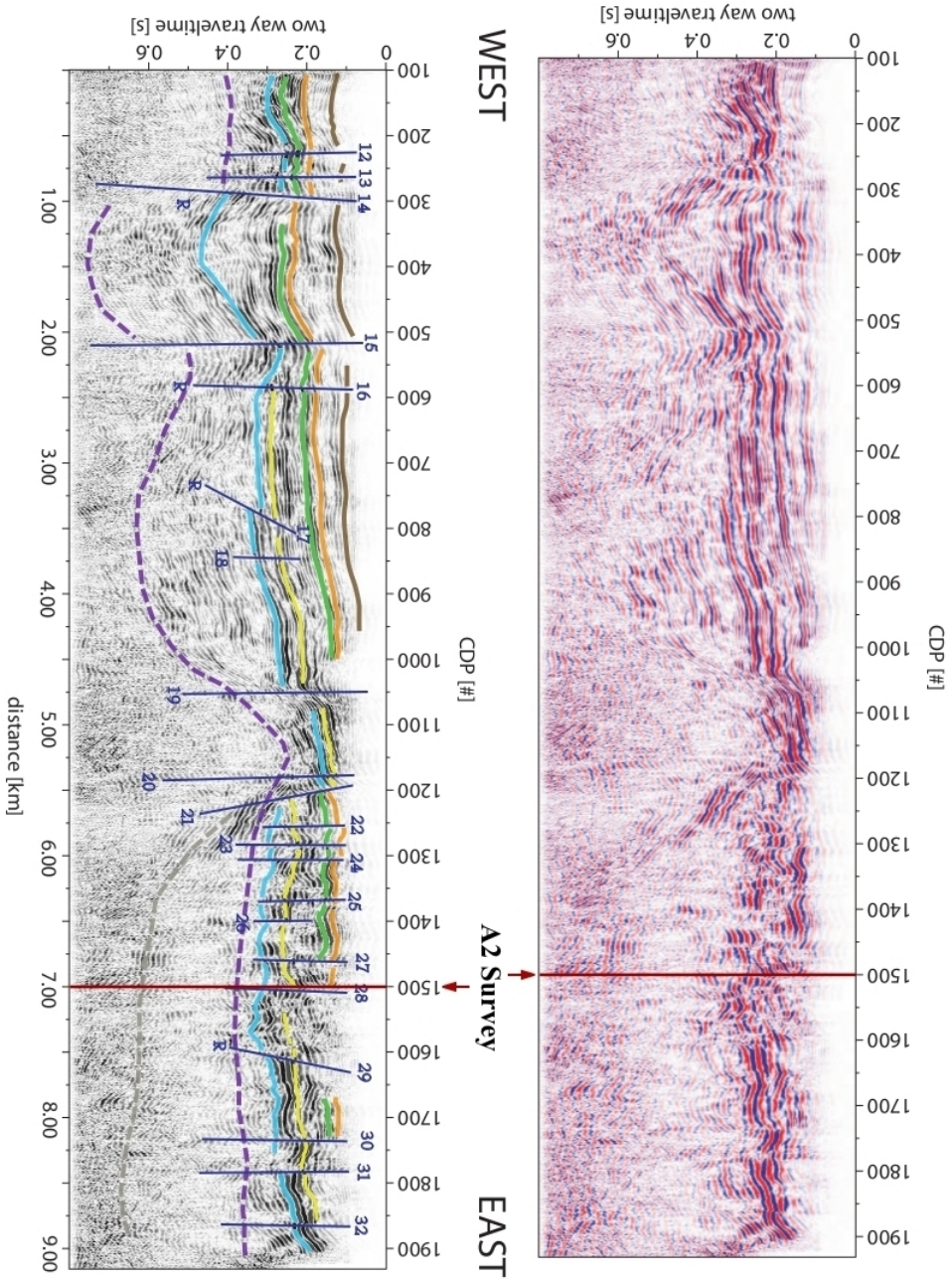

Figure 4.2: Reprocessed seismic reflection line and interpretation along Muhunoa East Road from Ewig [2008]. The deeper arrival (dashed grey line) does not follow the accepted basement topography above (dashed purple) or the bottom of a band of high-amplitude reflectivity (light blue), so could be either a reflection from out of line (side-swipe) or a low angle thrust. This survey intersects with the north end of A2 seismic line at CDP 1500 (indicated). Reproduced from Ewig [2008].

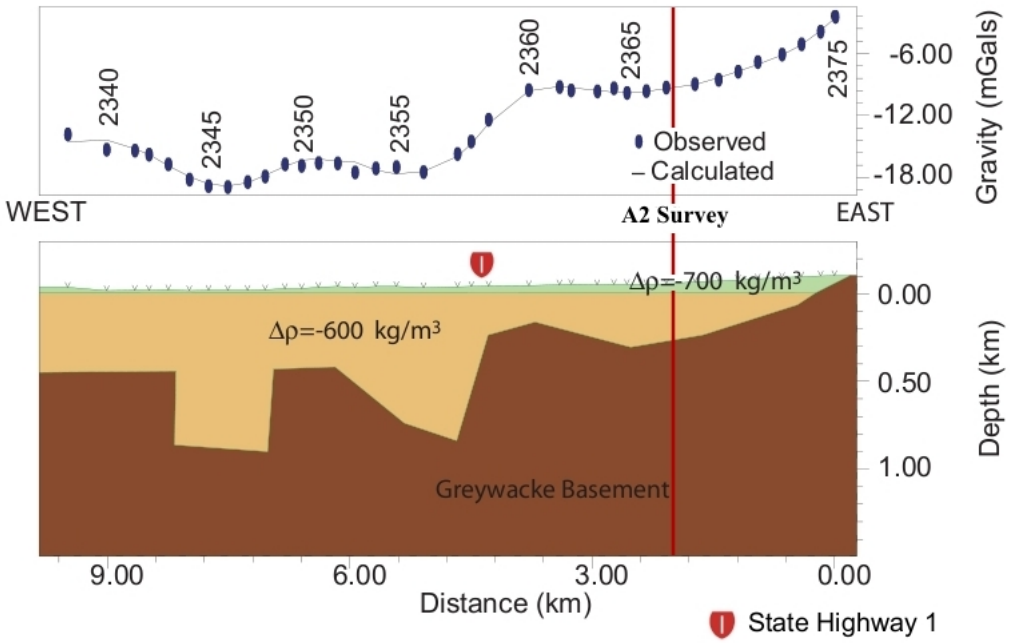

Figure 4.3: Gravity profile showing basement depth along Muhunoa East Road from Ewig [2008]. At the eastern end of the profile the Bouguer anomaly is 0.5 mGal because of basement greywacke exposed at the surface in the Tararua Ranges. The location of the intersection with the A2 seismic line is indicated. Reproduced from Ewig [2008].

structural ambiguity related to basement structure and faulting beneath the eastern edge of the Wanganui Basin. This is important on two counts: firstly, to resolve the true depth to basement beneath the eastern margin of the Wanganui Basin; and secondly to find the elusive evidence for the Miocene shortening in the North Island.

To do this, sixteen new gravity points were collected and added to existing gravity data near Muhunoa East Road, and a short gravity profile was modelled from the newly collected gravity points. Additionally two seismic refraction profiles (A1 and A2) were shot south of the existing Muhunoa East

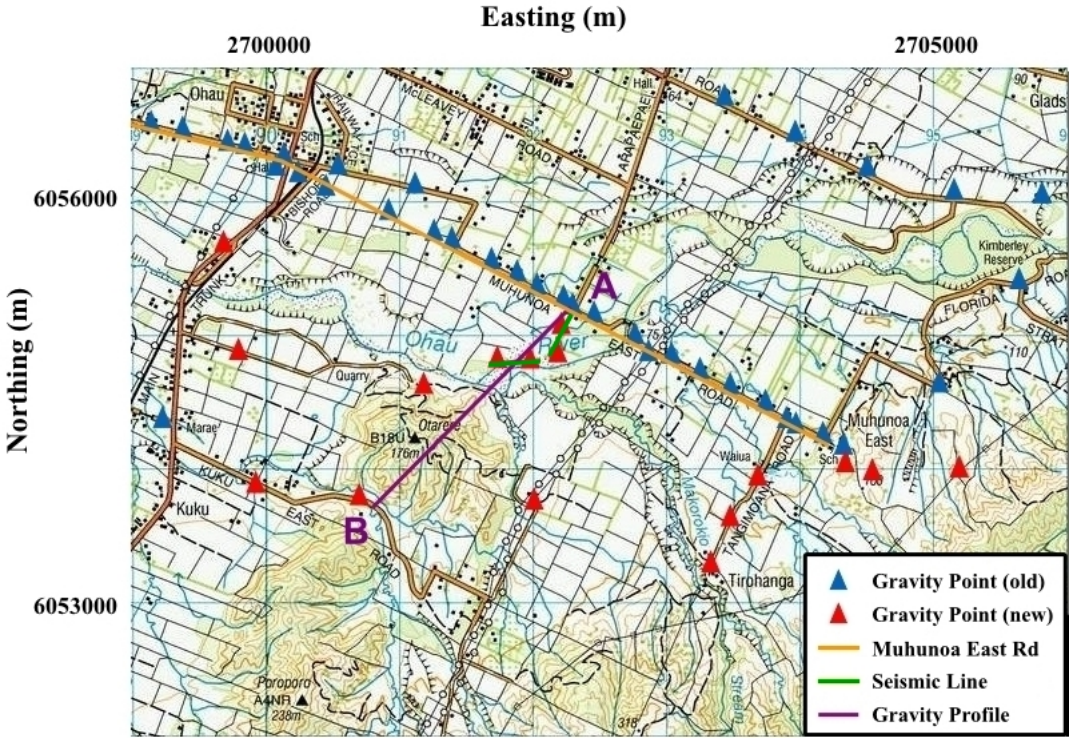

Figure 4.4: Map of Muhunoa East Road study area south of Levin showing the location of all seismic and gravity data. The location of the reprocessed Muhunoa East Road seismic and gravity lines (Aharoni [1991], Ewig [2008]) is shown in orange. New gravity points (red) were collected for this study while old gravity points (blue) are from previous surveys. The gravity profile (purple) was created using a combination of old and new gravity points. The seismic lines shot for this study (green), are A1 (east-west) and A2 (northeast-southwest). Scale is in New Zealand Map Grid (NZMG), squares are 1 km.

Road surveys (figure 4.4). The aim of the additional gravity points, gravity profile and seismic lines was to find the basement dip and depth south of Muhunoa East Road and determine if a pull-apart basin had formed where the Tararua range front steps laterally. Any such basin would have filled with sediments washed down from the Tararua Ranges and so would have no surface features.

4.1 Muhunoa East Road gravity

The gravity profile along Muhunoa East Road collected by Aharoni [1991] used a sediment density $\rho = 2070$ kg/m^3 and calculated a regional gravity field based on seismic data collected along the same profile. Ewig [2008] remodelled the same profile using a sediment density $\rho = 2000$ kg/m^3 and calculating the regional field from a 3-D gravity model of the crustal structure and subducting slab. This different approach to the regional field calculations resulted in a depth to basement in Ewig [2008] 50% greater the initial depths by Aharoni [1991]. The basement depth modelled from this gravity profile (figure 4.3) compares well with the interpreted basement on the reprocessed seismic line (figure 4.2).

4.1.1 Muhunoa East Road gravity method

This survey measured gravity at sixteen new points together with a base station at the one of the points collected by Aharoni [1991]. Five of the new points were in the foothills of the Tararua Ranges while eleven were on the sediments of the Manawatu Plains (figure 4.4). For each point the raw gravity measurement was converted to a Bouguer gravity value. A detailed discussion of the methods used for gravity data analysis can be found in appendix A. These gravity points were then combined with the remodelled profile from Ewig [2008] and other nearby points taken from the IGNS database to create a Bouguer gravity contour map (figure 4.5).

From these new gravity points a short profile was created south of Muhunoa East Road (figures 4.4, 4.6). Because the Bouguer slab (appendix A.1.3) is

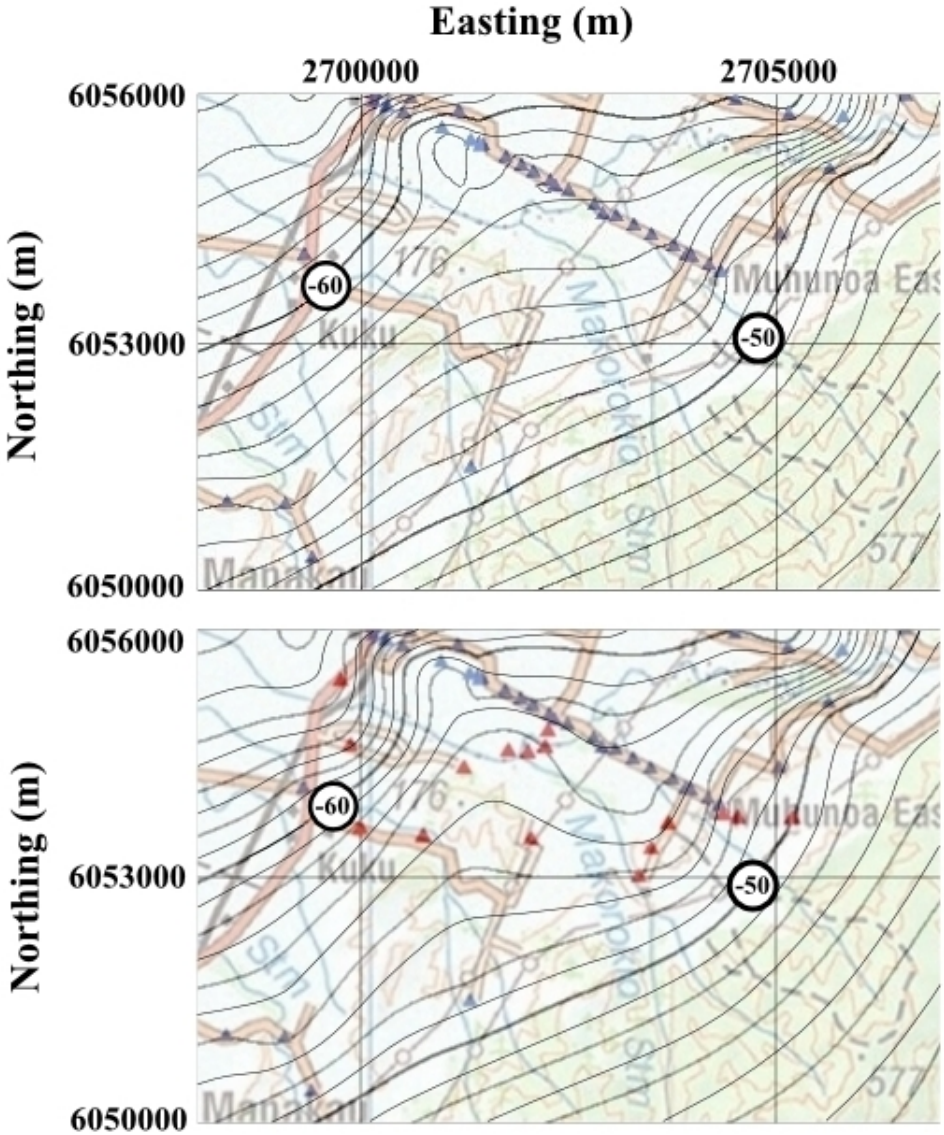

Figure 4.5: Bouguer gravity contour maps at Muhunoa East Road showing before (top) and after (bottom) the addition of this study's gravity points. Prior gravity points are shown in blue while gravity points collected for this study are shown in red. After new gravity points are added the gravity contours are seen to more closely follow the step in the Tararua range front. The heavy contour lines show -60 mGal and -70 mGal Bouguer anomalies and the contour spacing is 1 mGal. Scale is in New Zealand Map Grid (NZMG).

assumed to be greywacke basement rock with density of 2670 kg/m^3, any gravity point located on exposed greywacke basement rock theoretically has a residual anomaly of 0 mGal. Because of the proximity of the basin, the missing mass where less dense sediments have replaced greywacke basement does not allow the residual anomaly to quite reach 0 mGal, even for points on exposed greywacke basement.

All points on the G1 gravity profile had a regional field subtracted from the Bouguer anomaly values to calculate the residual gravity field. The contours of the regional gravity field were shown to run north-south in this area [Ewig, 2008]. This regional field value was picked using a set residual gravity field value of -0.5 mGal at the southern end of the G1 profile due to intersection with exposed greywacke basement. Because the G1 gravity profile runs northeast-southwest in this area, semi-parallel to the regional field contours, the regional gravity field was found to vary by 1 mGal along the length of the G1 profile. After the residual gravity field was calculated, this profile was modelled using gravity modelling software (see appendix A.4) using a sediment density of $\rho = 2070$ kg/m^3 and basement density of $\rho = 2670$ kg/m^3 [Ewig, 2008]. (The lack of points in the southern half of the gravity profile was due to the profile's running across a working quarry that was private land.)

4.1.2 Muhunoa East Road gravity interpretation

The additional gravity points from this study help to constrain the basement depth near the step in the boundary of the Tararua range front. From

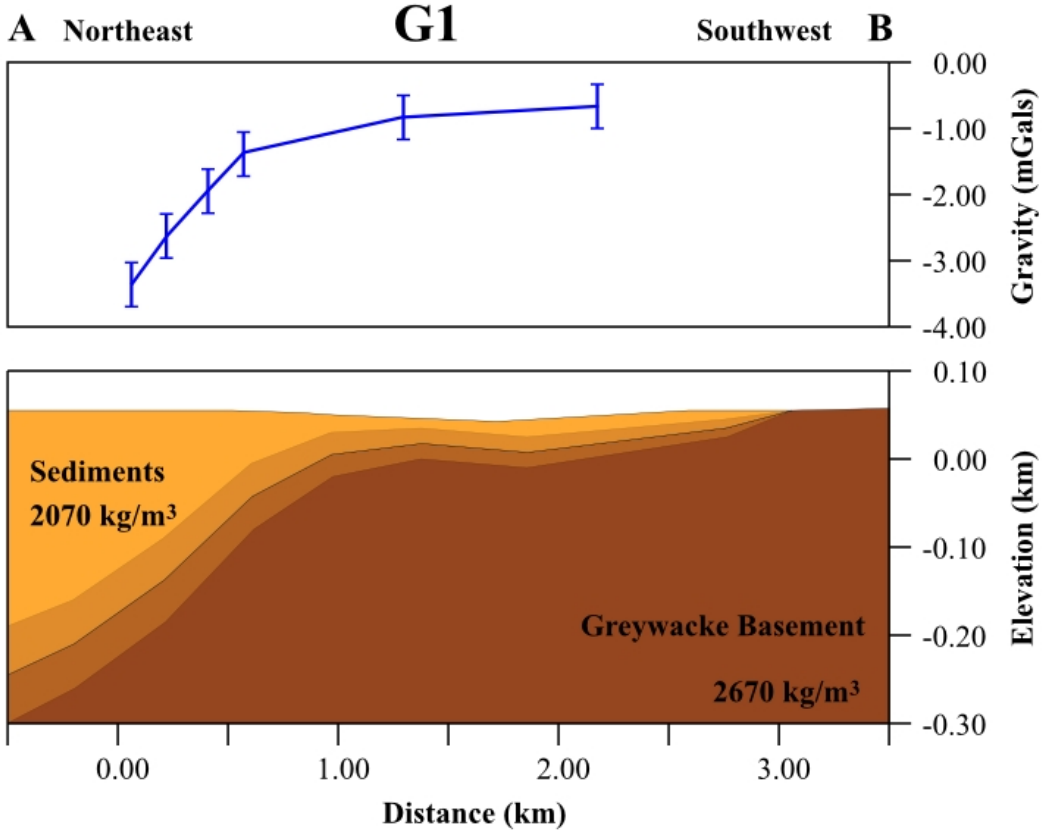

Figure 4.6: Gravity profile showing basement depth south of Muhunoa East Road. The location of the gravity profile is shown in figure 4.4. Observed gravity with uncertainties (blue error bars) and modelled gravity (blue line) are shown. Densities of $\rho = 2070$ kg/m^3 for sediments and $\rho = 2670$ kg/m^3 for greywacke basement rock were used. At the southwestern end of the profile the residual gravity field is -0.5 mGal because of greywacke basement exposed at the surface in the Tararua Ranges. The intersection with Muhunoa East Road occurs at 0 km distance on the horizontal scale. The steepest apparent basement dip observed is 12 ± 4^{o} northeast.

the gravity profile along Muhunoa East Road, (figure 4.3), the basement is known to gradually dip west beneath the sediments and river gravels of the Manawatu plains. The new perpendicular gravity profile constructed for this study shows the greywacke basement shallowing to the south as it approaches the exposed greywacke at the step in the Tararua range front.

Where the profiles intersect, according to the new profile (figure 4.6) there are 230±50 m of sediments overlying the greywacke basement, while according to the reprocessed Muhunoa East Road gravity profile (figure 4.3) there are ≈ 350 m. This discrepancy arises from the two profiles' having different regional gravity corrections where they intersect. The east-west gravity profile along Muhunoa East Road is tied to exposed greywacke 2.5 km to the east and has a spatially varying regional correction along it calculated by Ewig [2008]. In comparison the new north-south gravity profile is tied to exposed greywacke 1 km to the southwest and has 1 mGal of variation in its regional correction based on the regional gravity field calculated by Ewig [2008]. This leads to a difference of 5 mGal between the regional corrections used on the two gravity profiles and therefore also residual graivty fields (-4 mGal for this profile compared with -9 mGal for Muhunoa East Road gravity survey [Ewig, 2008]) at the point where the profiles intersect.

The steepest basement dip observed on this new gravity profile is estimated to be 12±4° north. Pull-apart basins often have sub-vertical drops in basement depth which should be observable on the gravity profile (figure 4.6) with a corresponding close contour spacing on the gravity contour map (figure 4.5). From the gravity profile and contour map constructed there is no evidence for the presence of a strongly developed pull-apart basin at the

step in the Tararua range front south of Muhunoa East Road.

4.2 Muhunoa East Road seismic reflection survey

A seismic reflection survey shot along Muhunoa East Road by Aharoni [1991] was used to determine basement depth in conjunction with a gravity profile. This survey was reprocessed and reinterpreted by Ewig [2008]. The reprocessing identified a deeper, undulating event (dashed grey line, figure 4.2) which was initially interpreted as the basement reflector. However, Ewig [2008] notes that the gravity profile along Muhunoa East Road indicates a shallow basement at the eastern end of the line (figure 4.3). Because of this gravity profile the basement horizon was reinterpreted to be a shallower, undulating, low frequency horizon just beneath the bottom of a band of high amplitude reflectivity (dashed purple line beneath light blue line, figure 4.2).

4.2.1 New Muhunoa East Road seismic surveys

Two seismic refraction surveys were collected south of the seismic profile [Aharoni, 1991] along Muhunoa East Road. The east-west seismic refraction line was labelled A1 and the north-south seismic refraction line was labelled A2 (figure 4.7). On both surveys geophones were placed at 10 m intervals. The slightly curved shape of survey A1 was due to terrain constraints. On survey A1 48 geophones were used, while 43 geophones were used on survey A2 owing to the length of the service road. The seismic source was a hydraulic

thumper and shots were recorded using a Geometrics^{TM} Strataview^{TM} R48. For survey A1 six shot points were used: 15 m and 127 m off the east end of the line, 16 m and 104 m off the west end of the line, one mid shot and one at a large offset to the north of the line. For survey A2 five shot points were used: 7 m and 315 m off the north end of the line, 10 m and 173 m off the south end of the line and one in the middle (figure 4.7). Single thumper shots were recorded at all shot points, with stacks of 4-8 shots also recorded at shot points off the ends of each line. In survey A2 there was trouble triggering the R48 for records with large shot offsets, because electric fences in the area induced a current in the trigger cable. The affected shots were triggered manually and then adjusted using a bulkshift static correction during data processing to compensate for this problem. A shot record length of 2048 ms and sample rate of 0.5 ms was used for all automatically triggered shots, while a record length of 8192 ms and sample rate of 2 ms was used for all manually triggered shots.

The aim of these surveys was to investigate basement depth south of Muhunoa East Road, and whether the deep, undulating reflection on the Muhunoa East Road seismic reflection line (dashed grey line, figure 4.2) was due to side-swipe from dipping basement to the south. Having the two surveys perpendicular to each other allowed for the arrival direction of any deep seismic reflections to be modelled accurately, and the depth and dip of the basement to be determined.

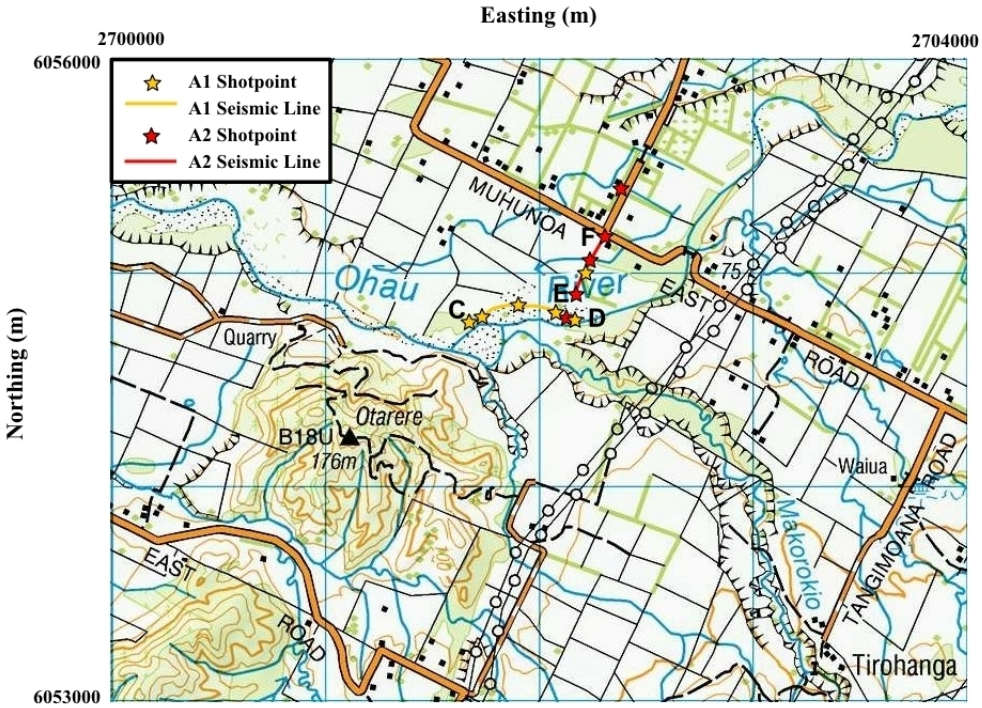

Figure 4.7: Map of Muhunoa East Road showing geophone deployment and shot locations for surveys A1 (labelled C to D) and A2 (labelled E to F). Scale is in New Zealand Map Grid (NZMG), squares are 1 km.

4.2.2 New Muhunoa East Road seismic survey processing

A detailed discussion of the methods used for seismic refraction survey analysis can be found in appendix B.3. The aim of this processing was to resolve arrivals with a two way travel time (TWTT) of less than 600 ms. The following list summarises the processing operations.

- Bulkshift static correction on non-triggered shots
- Dead/noisy trace removal

- Frequency-wavenumber filter
- Frequency domain filter: BP (30 40 70 80) Time Window (0-250 ms)
- Frequency domain filter: BP (20 30 70 80) Time Window (250-350 ms)
- Frequency domain filter: BP (10 20 70 80) Time Window (350-1000 ms)
- Balance
- AGC: 200 ms window

4.2.3 New Muhunoa East Road seismic survey interpretation

Survey A1

Refraction 1: A single shot from each end of the survey was taken (figure 4.8) and the plus-minus method was applied using the direct arrival and first refraction (see appendix B.2.4). This obtained the velocity of the near surface layer (480±50 m/s), the second layer (3500±200 m/s) and the depth of the layer boundary. The slow near-surface layer of sediment was found to be 5±1 m thick beneath survey line A1 (figure 4.9).

Refraction 2: A refraction from a third layer was apparent in shots from both directions (figure 4.8). This refraction appeared to have different velocities in different directions, leading to the conclusion that it was a refraction from a dipping layer. In order to analyse this a static correction was used to remove the slow near-surface layer, then the refraction from a dipping layer

method (see appendix B.2.3) was applied to find the velocity, depth and dip of the third layer. It was found to have an updip velocity of 5250±200 m/s (refraction 2a, figure 4.8) and a downdip velocity of 4050±200 m/s (refraction 2b, figure 4.8) which resulted in a true velocity of 4530±200 m/s (see appendix B.2.3). This is a reasonable velocity for weathered greywacke so this refraction was interpreted to be refraction from the top of the buried basement. This third layer was found to dip 9±4° east at an azimuth of 082° resulting in depths of 85±20 m at the west and 202±50 m at the east end of the A1 line (figure 4.9).

Survey A2

Refraction 1: A single shot from each end of the survey was taken (figure 4.10) and the plus-minus method was applied using the direct arrival and first refraction (see appendix B.2.4). This obtained the velocity of the near surface layer (480±50 m/s), the second layer (3500±200 m/s) and the depth of the layer boundary. The slow near-surface layer of sediment was found to be ≈ 11±1 m thick beneath survey line A2 (figure 4.11).

Reflection 2: A series of reflections were observed in the middle shot of survey A2 (see figure 4.10). The first of these is only visible to the southern part of the survey, and the peak of the reflection curve is possibly south of the shotpoint indicating a layer dipping north. Not enough of the reflection curve is visible to accurately measure its curvature, however, so this reflectivity zone is interpreted as being flat (figure 4.11). The depth of the reflector was calculated using seismic reflection analysis (see appendix B.4.3), and was found to be 170±10 m.

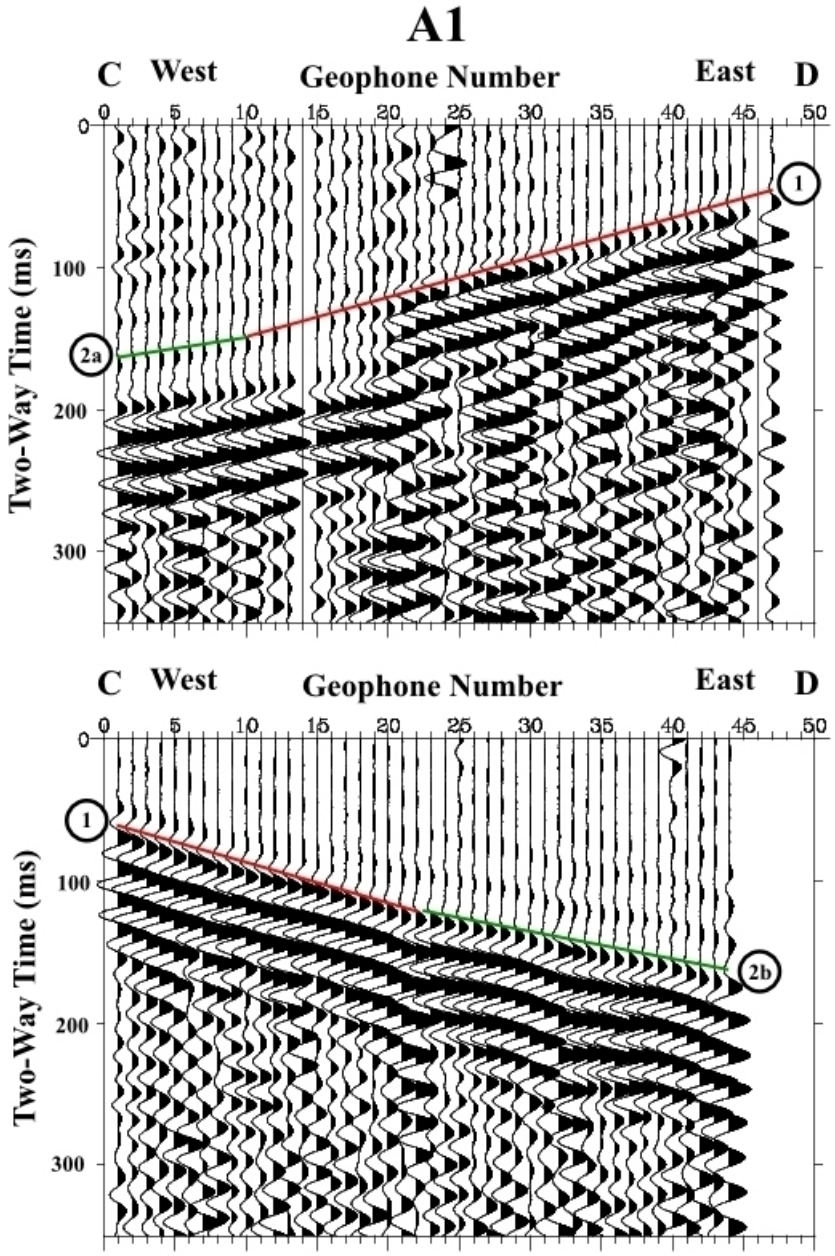

Figure 4.8: Seismic refraction shots from the A1 survey in updip (top) and downdip (bottom) directions. Refractions from the second layer are shown in red, while refractions from the third layer are shown in green. The crossover distance is smaller and the apparent velocity of the third layer is slower in the downdip direction. Velocities of arrivals are 3500±200 m/s (red, 1), 4050±200 m/s (downdip, green, 2b) and 5250±200 m/s (updip, green, 2a). This gives a true layer velocity of 4530±200 m/s for the third layer.

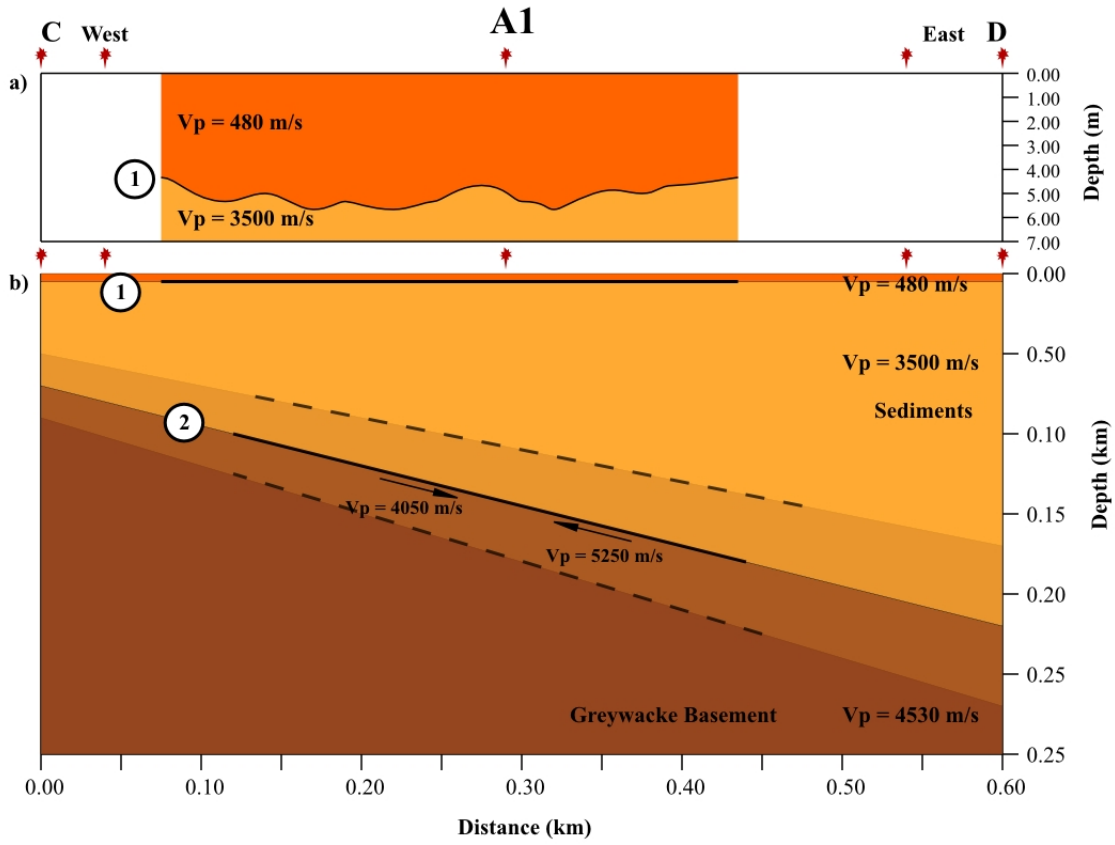

Figure 4.9: Diagram showing layer depths and velocities for A1 refraction survey. a) shows near surface layer depth calculated using the plus-minus method (see appendix B.2.4). b) shows depth to greywacke basement calculated using the refraction from a dipping layer method (see appendix B.2.3) with updip and downdip refraction velocities. In this survey the top of the greywacke basement was found to dip east at 9 ± 4^{o}. Heavy black lines show which sections of the interfaces were imaged by the seismic survey.

Reflection 3: In the middle shot of survey A2 (see figure 4.10) a reflection with more pronounced curvature than reflections 2 and 4 was observed. This stronger curvature indicating a slower velocity leads to the conclusion that reflection 3 is a conversion, a P-wave reflected as an S-wave or an S-wave reflected as a P-wave. The TWTT is too short and curvature of this reflection too strong for it to be a conversion from the same interface as reflection 2. Without this arrival being visible across enough traces or apparent on any other shot records there is not enough information to determine the correct velocity, depth or dip for this reflection.

Reflection 4: In the middle shot of survey A2 (see figure 4.10) another reflection was only visible across a few traces at the southern end of the shot record. Not enough of the reflection curve is visible to accurately measure its curvature, which appears similar to the curvature of reflection 2 above.

The slow near-surface layer of sediment is thicker to the north (11±1 m thick beneath survey A2) and slowly thins to the south as it approaches the exposed basement at the step in the Tararua range front (5±1 m thick beneath survey A1). In addition the reflection curve peaks in survey A2 all appear to be south of the shotpoint (geophone 24) and the reflections are not visible on the northern half of the survey. This indicates that beneath survey A2 the layers dip north, but unfortunately not enough of the reflection curves are visible to allow the layer dips to be calculated.

To identify the layer boundaries beneath survey A2 the arrivals were extrapolated south to survey A1 and north to beneath Muhunoa East Road (see figure 4.2). The eastern end of survey A1 lies directly south of survey A2 (see figure 4.7). Reflection 2 on survey A2 lies at 200±50 m depth,

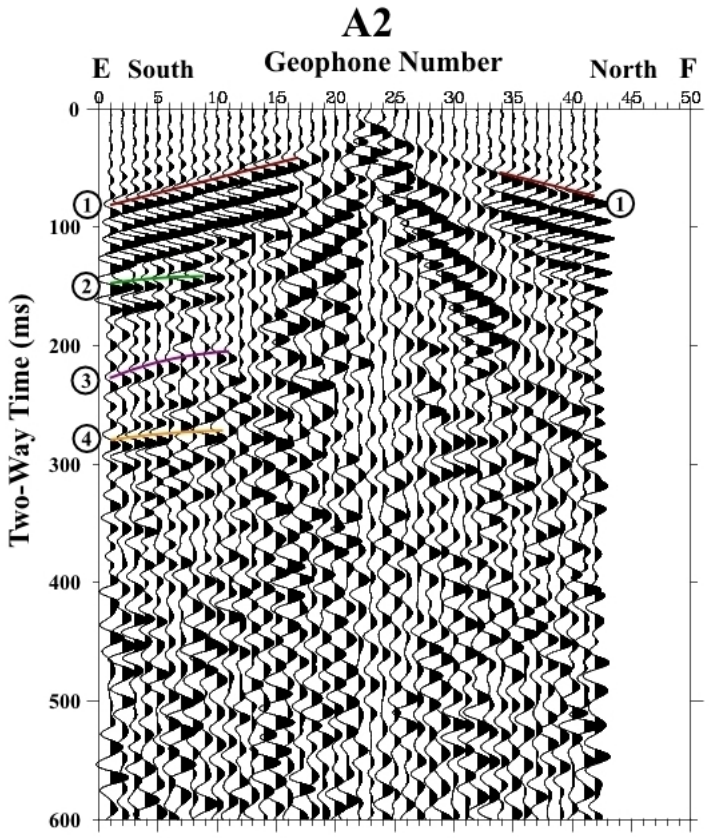

Figure 4.10: Seismic reflection shot from the A2 survey. Shallow refractions are shown in red while the deeper reflections are shown in green (reflection 2, top of basement), purple (reflection 3, conversion) and orange (reflection 4, intra-basement layer). The stronger curvature of reflection 3 (purple) shows that it has a slower velocity, indicating that it might be a P-S or S-P conversion from a shallow layer. Beneath 280 ms the change in frequency content shows the presence of a zone of intra-basement low frequency reflectivity. This is a common feature of greywacke basement rock.

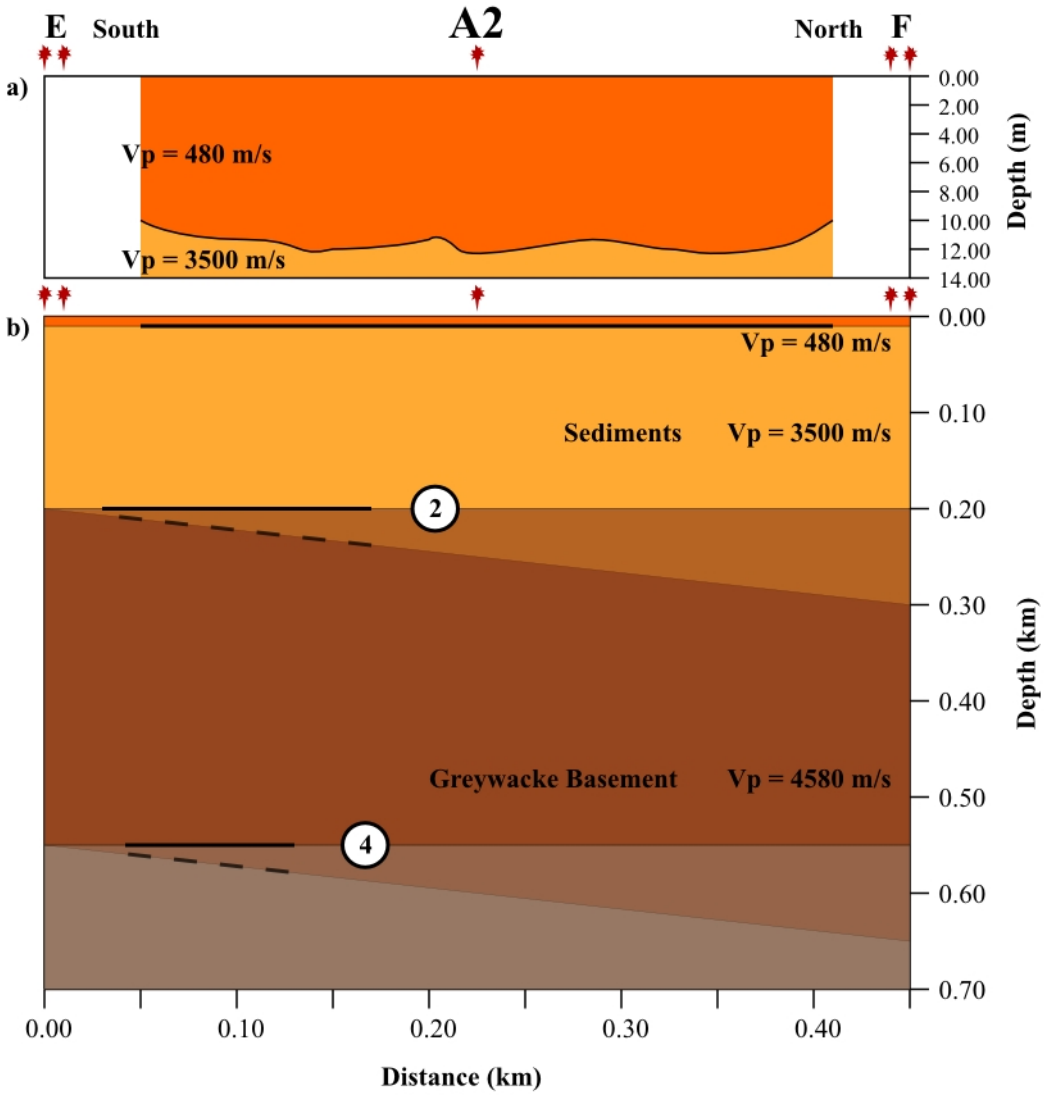

Figure 4.11: Diagram showing layer depths and velocities for A2 survey. a) shows near surface layer depth calculated using the plus-minus method (see appendix B.2.4). b) shows depth to two reflectors (2) and (4). The peaks of both reflection curves (see figure 4.10) are not visible so there is not enough evidence from seismic reflection data to say that the layers are dipping. The heavy black lines that show which sections of the interfaces were imaged by the seismic survey are shown not dipping. The dashed lines show the maximum possible layer dip of 12° north from gravity data (see figure 4.6). Reflection (2) is determined to be from the same interface as refraction (2) in survey A1 and the interval velocity between reflections (2) and (4) is 4580±250 m/s indicating that reflection (2) is from the top of the greywacke basement while reflection (4) is from an intra-basement layer (see appendix B.4.4).

which corresponds well to the greywacke basement depth at the eastern end of survey A1. This indicates that reflection 2 in survey A2 is from the top of the buried greywacke basement and therefore reflection 4 must be from a deeper, intra-basement layer. As reflection 2 is interpreted as the top of the greywacke basement, the interval velocity between reflections 2 and 4 must be 4580±250 m/s of the greywacke basement. Given the interval velocity and observed TWTT of reflection 4, the depth of reflection 4 can be calculated to be 500±100 m using the Dix equation (see appendix B.4.4).

Assuming flat layers, if reflections 2 and 4 are extrapolated to the northern end of survey A2 where it intersects Muhunoa East Road, they would have TWTT's of 0.15 s and 0.27 s respectively. The gravity survey carried out south of Muhunoa East Road (figure 4.6) found the steepest basement dip to be 12° north. Assuming a layer dip of 12° north then the TWTT's of reflections 2 and 4 extrapolated to beneath the northern end of survey A2 would be 0.21 s and 0.32 s respectively. This means that, dependent on layer dip, beneath Muhunoa East Road reflector 2 (greywacke basement) must have a TWTT between 0.15–0.21 s and reflector 4 (intra-basement layer) must have a TWTT of 0.27–0.32 s.

On the Muhunoa East Road seismic survey, (figure 4.2), at the point where the surveys intersect there are reflectors with TWTT's of 0.13 s (orange), 0.18 s (green), 0.24 s (yellow), 0.30 s (light blue) and 0.38 s (dashed purple). Ewig [2008] describes the green reflector as being located within a high-amplitude zone beneath a high amplitude shallow reflector, the yellow reflector as a distinct, clear, high-amplitude reflector within a high amplitude zone, the light blue reflector as marking the bottom of a band of high ampli-

tude reflectivity that can be traced across the entire section and the dashed purple reflector is interpreted to be an irregular, undulating, low frequency basement reflector. According to the TWTT information on survey A2, reflection 2 would correspond to the green reflector and reflection 4 to the light blue reflector. In survey A2 reflection 2 is an energetic zone of reflections which corresponds well with the green reflector's characteristics (see figure 4.2).

The sediment velocities above the greywacke basement in surveys A1 and A2 are found to be 480±50 m/s (near-surface) and 3500±200 m/s (second layer). The velocity in the near-surface layer is normal but the second layer velocity is unusually fast for young, shallow sediments. Rounded boulders in river gravels allow for faster transfer of seismic energy leading to high velocities closer to those of the parent rock. Erosion from the Tararua Ranges has led to well packed and sorted gravels similar to those present in the Canterbury Plains which have been found to have velocities as high as 3350 m/s [Woodward and Kicinski, 1987], so the velocity observed here is not unreasonably fast for shallow sediments.

Using the extrapolated TWTT of 0.15–0.21 s dependent on layer dip for reflection 2 at the north end of the line (figure 4.10) and layer velocities of 480±50 m/s and 3500±200 m/s (figure 4.11) for the sediments overlying the greywacke basement, a basement depth of 250±50 m at the north end of survey A2 beneath Muhunoa East Road is determined. This is similar to the 230±50 m of sediments found by the gravity survey (figure 4.6) and shallower than the ≈ 350 m of sediments found by the previous gravity survey along Muhunoa East Road (figure 4.3, from Ewig [2008]). The difference in

sediment thickness between the two gravity surveys was due to a difference between the regional gravity field corrections used. The uncertainty in the thickness of sediments from seismic survey A2 was due largely to uncertainty in the dip of greywacke basement in the area. Basement dip is important since the top of the greywacke basement was imaged beneath only the southern end of survey A2, not the northern end where it intersects Muhunoa East Road.

The dip of 9±4° east for the top of the greywacke basement on survey A1 is an apparent dip since the line does not run in the true dip direction of the layer. Unfortunately survey A2 did not provide any accurate information about the dip of the greywacke basement; however the gravity survey found an apparent dip for the top of the buried greywacke basement of 12±4° northeast. The two apparent dips plot on a stereonet (figure 4.12) with trends/plunges of 045/12±4 and 082/09±4. These points both fall onto the plane (great circle) with strike/dip direction/dip of 310/NE/12 which describes the true dip of the top of the greywacke basement. Due to uncertainties in the two apparent dip measurements, the strike of the greywacke basement lies at an azimuth between 278–008, while the dip lies between 12–19° (see figure 4.12).

4.3 Muhunoa East Road survey summary

The reprocessed Muhunoa East Road seismic line (figure 4.2) identified a deep reflection that was interpreted to be possibly a result of side-swipe from basement at the lateral step in the Tararua range front to the south

[Ewig, 2008]. Seismic and gravity studies were carried out south of Muhunoa East Road to investigate the basement depth near the step in the Tararua range front.

A gravity survey and two seismic surveys were carried out south of Muhunoa East Road (figure 4.4). The gravity survey found the greywacke basement south of Muhunoa East Road to dip northeast with a steepest apparent dip of 12±4° (figure 4.6). Combined with seismic survey A1 (figure 4.8) the top of the greywacke basement was found to dip 310/NE/12 (figure 4.12). Errors in the two apparent dips used to calculate the basement dip lead to uncertainty in azimuth between 278–008 and dip between 12–19°. Surveys A1 and A2 found the basement to have a seismic velocity of 4530±250 m/s indicative of weathered greywacke, while the overlying sediments have a velocity of 3500±200 m/s, which is fast but not unreasonable for river gravels. None of the surveys found evidence for any sub-vertical drop in basement that would provide a favourable surface off which a laterally travelling seismic wave could reflect.

Where the surveys intersect Muhunoa East Road the basement depth found from these new gravity and seismic surveys was shallower than the depth from the Muhunoa East Road surveys (figures 4.2, 4.3) [Ewig, 2008]. The new gravity survey found a basement depth of 230±50 m rather than 350 m owing to different regional gravity models. The A2 seismic survey (figure 4.10) found reflections with TWTT's of 0.15-0.21 s and 0.27-0.32 s beneath the Muhunoa East Road end of the survey dependent on layer dip. These correspond roughly with reflections observed on the Muhunoa East Road seismic survey at 0.18 s and 0.30 s (green and light blue, figure 4.2)

that were previously interpreted as layers in the sediments overlying the greywacke basement (Ewig, [2008]). On the A2 seismic survey, reflection 2 is interpreted to be from the top of the greywacke basement and reflection 4 from an intra-basement reflector (figure 4.11) while on the Muhunoa East Road seismic survey the top of the greywacke basement was interpreted at 0.38 s (dashed purple, figure 4.2). Given layer velocities this TWTT for reflection 2 corresponds to a greywacke basement depth of 250±50 m beneath Muhunoa East Road from survey A2 dependent on layer dip.

The currently accepted location of the Northern Ohariu Fault and the location for the potential pull-apart basin are shown (figure 4.1). From the surveys conducted in this study there is no evidence for a distinct hypothesised pull-apart basin at the step in the Tararua range front due to dextral strike-slip motion on the Northern Ohariu Fault. Without any steeply dipping surface at a favourable offset from the Muhunoa East Road seismic line, the intra-basement reflected arrival observed is likely to be due to an in-plane low angle intra-basement thrust fault similar to those seen on other seismic lines across the South Wanganui Basin (figure 4.2, Ewig [2008]).

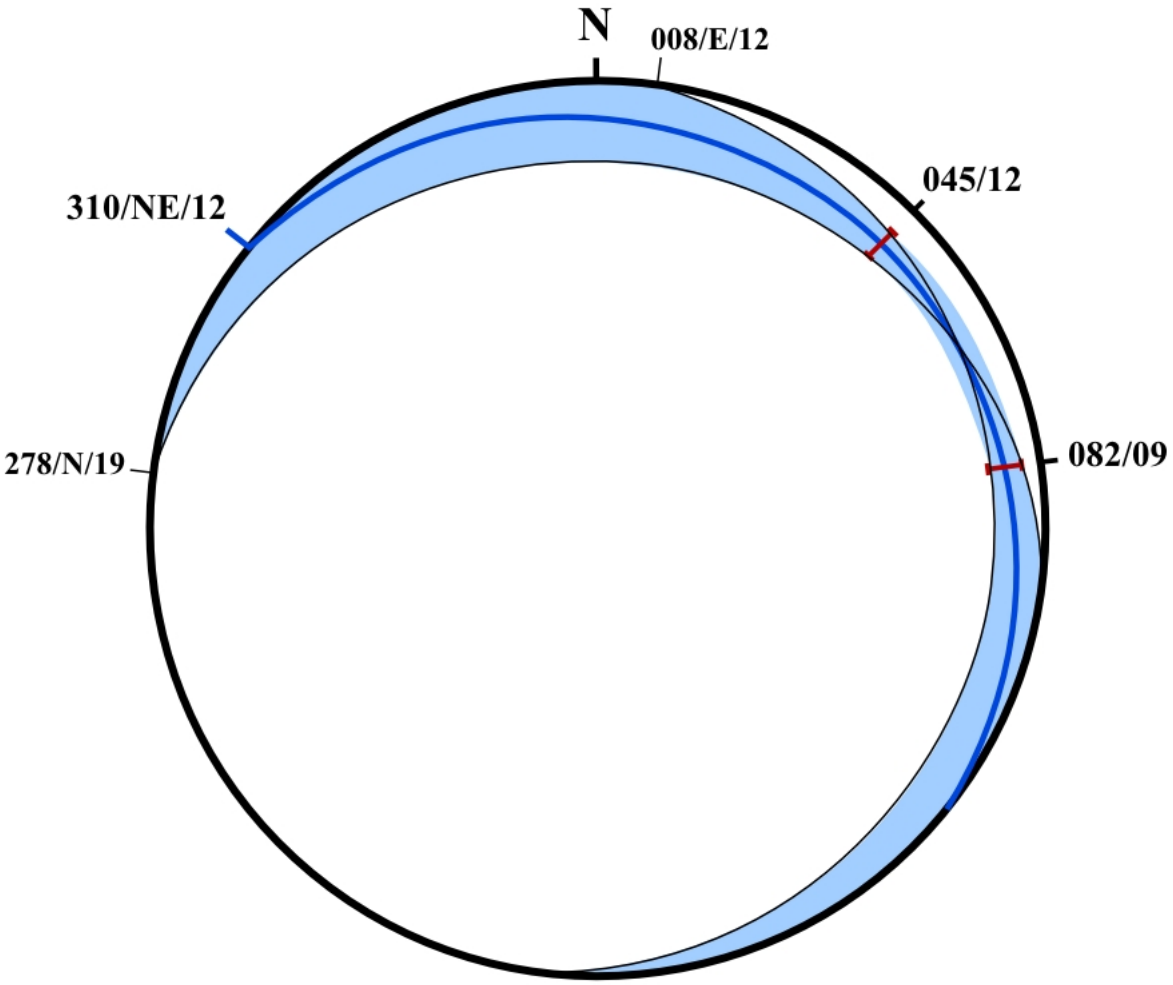

Figure 4.12: Stereonet showing the calculation of the true dip of the top of the greywacke basement south of Muhunoa East Road. The apparent dips and uncertainties of refraction 2 (A1 survey, 082/09) and the gravity profile (045/12) are described by trend/plunge points on the stereonet (red error bars). These two points fall on a unique great circle, 310/NE/12 that describes the strike and dip of the top of the greywacke basement. The error in the two apparent dips leads to uncertainty in the strike and dip of the great circle (shown by blue area). The strike lies at an azimuth between 278–008, while the dip lies between 12–19°.

Chapter 5

Wallace Road – Biogenic gas survey

The biogenic gas site near Wallace Road is the second survey in this study (figure 5.1). A water well drilled in a valley on the northwest side of a property on Wallace Road in 1970 flowed gas for 48 hours before it was extinguished and cased. The flow of gas was as strong after 48 hours as it was to start, indicating the presence of a significant quantity of gas. The well log shows that the gas flowed from the top 1.5 m of a dry sand layer at a depth of 19.2 m [Proposed Geoprobe Programme, PEP 38771 Report, Ian R Brown Associates Ltd].

For this study seismic refraction lines were collected east-west and north-south over the biogenic gas accumulation. The aim was to use this survey as a control for the survey at Campion Road (chapter 6). In this location the presence of gas had been confirmed and the depths and lithology known from well log data (table 5.1). The seismic characteristics observed in this survey

Depth (m)	Description
0 - 1.20	Clay, topsoil
1.20 - 6.10	Peat, black
6.10 - 12.19	Clay, blue, with areas of mixed clay and sand
12.19 - 15.70	Sand, grey, heaving, fairly fine
15.70 - 17.07	Sand, water-bearing, produced 60 gal/hr water
17.07 - 19.05	Sand, grey, very hard (sandstone)
19.05 - 19.20	Peat
19.20 - 24.40	Sand, dry, grey, hard. Gas at 19.20-20.73 m
24.40 - 31.09	Sand, grey, very fatty, no good for screening
31.09 - 31.70	Clay, blue
31.70 - 33.15	Gravel, blue, water-bearing. Cased to 31.62 m

Table 5.1: Table detailing lithologies present from water well log at biogenic gas site [Proposed Geoprobe Programme, PEP 38771 Report, Ian R Brown Associates Ltd]. Biogenic gas was produced from dry sand layer at 19.20-20.73 m.

could be used to help interpret the Campion Road survey. An additional seismic line and gravity profile were collected to the south of the biogenic gas accumulation running perpendicular to the Tararua range front to investigate basement depth and help understanding of the deeper structure in the area (figure 5.1).

5.1 Wallace Road south – Basement depth survey

The seismic profile [Aharoni, 1991] along Muhunoa East Road shows the basement rock of the Tararua range front dipping down in a series of fault blocks beneath the sediment of the Manawatu plains. In this study a seismic

refraction line (B1) was shot along Wallace Road to determine the depth and dip of basement rock near the biogenic gas survey site. This new seismic line ran perpendicular to the Tararua range front as in the 1991 Muhunoa East Road survey (figure 5.1). Four gravity points were collected and a gravity profile constructed along Wallace Road supplemented by existing points, to help develop a model for a first order examination of basement structure in the area.

5.1.1 Wallace Road south – gravity method

Four gravity points were collected around the Wallace Road loop, while two more points were collected at known gravity points at the west end of Wallace Road and the east end of Muhunoa East Road to be used as base stations for survey calibration and drift correction. These gravity points had the same processing as the Muhunoa East Road gravity survey (see appendix A) and a Bouguer gravity contour map was created using the four new points together with nearby points from the IGNS database (figure 5.2). A regional gravity field, [Ewig, 2008], was subtracted to calculate the residual gravity field at each point. The G2 gravity profile was constructed using the residual gravity field along the southern branch of Wallace Road and tied to the exposed greywacke basement of the Tararua Ranges at the eastern end of the line (see figure 5.1). The regional gravity field varied by 4 mGal along the length of the G2 profile, leading to a change of 10 mGal in Bouguer gravity and 14 mGal in residual gravity along the profile.

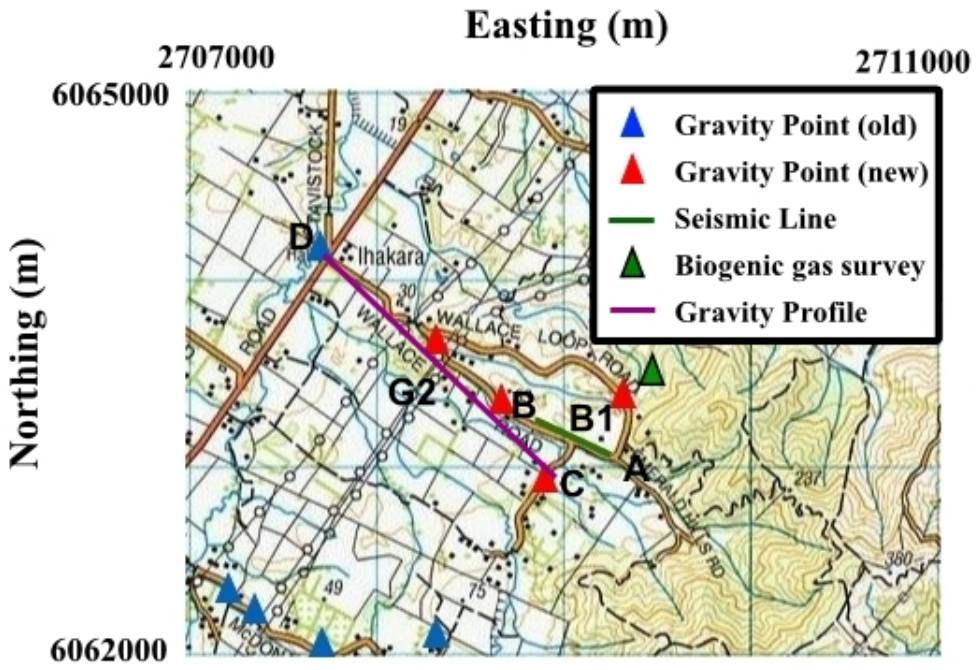

Figure 5.1: Map of Wallace Road study area northeast of Levin showing existing gravity points (blue), new gravity points taken for this study (red), gravity profile (purple) and east-west seismic line (B1, green). The site of the biogenic gas survey (Chapter 5) is also shown. Scale is in New Zealand Map Grid (NZMG), squares are 1 km.

5.1.2 Wallace Road south – gravity interpretation

The additional gravity points help to constrain the gravity contours near Wallace Road, but do not change the overall picture (figure 5.2). The contours on the Bouguer anomaly gravity map still run approximately parallel to the edge of the Tararua range front. The gravity profile constructed along the southern branch of Wallace Road shows the basement dipping west with a steepest dip of 14±4° apart from where the basement is faulted (figure 5.3). This gravity profile has a very similar shape to the eastern end of the parallel gravity profile along Muhunoa East Road (see figure 4.3). Nothing in this

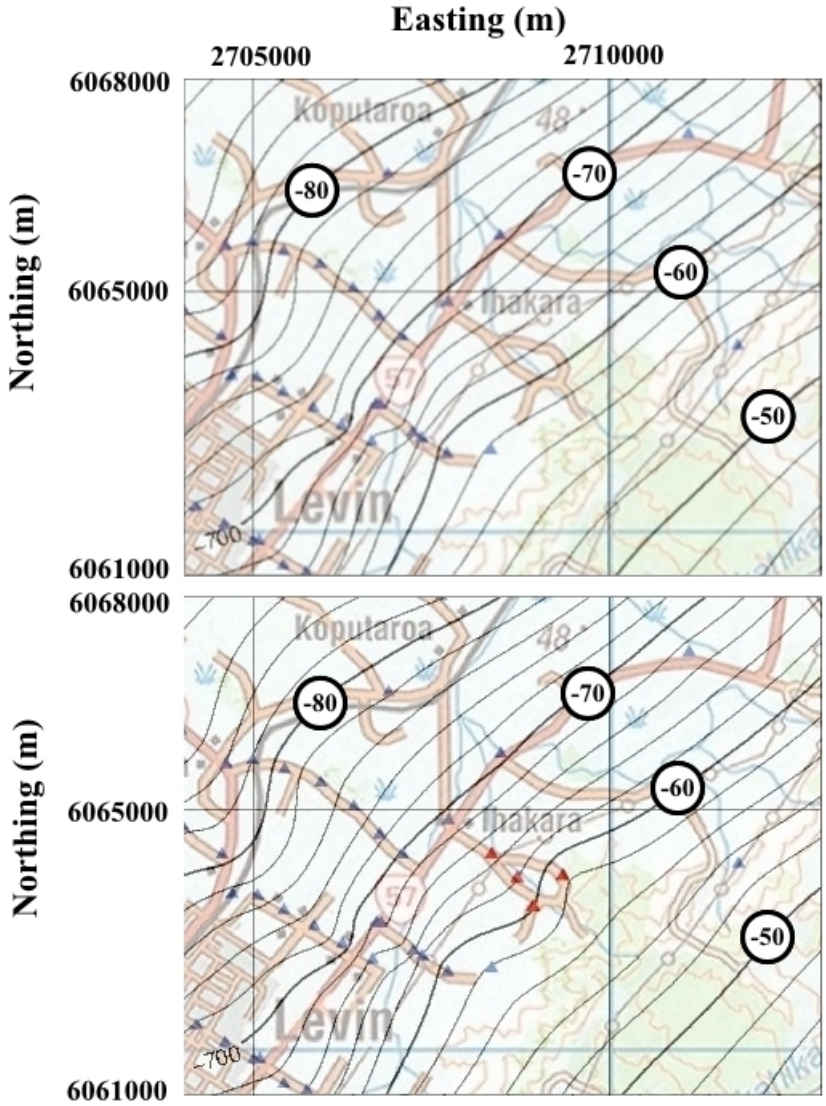

Figure 5.2: Bouguer gravity contour map at Wallace Road showing before (top) and after (bottom) the addition of this study's gravity points. Existing gravity points are shown in blue while new gravity points are shown in red. Little significant change is observed with the addition of the new points. The heavy contour lines show -60 mGal to -90 mGal anomalies and the contour spacing is 2 mGal. Scale is in New Zealand Map Grid (NZMG).

regional gravity survey indicates the presence of any unusual structures that could lead to gas accumulation.

5.1.3 Wallace Road south – seismic refraction survey

A seismic refraction survey was collected east-west along Wallace Road labelled B1 (figure 5.1). Geophones were placed at 5 m intervals on the grass verge of the road. The seismic source used was a hydraulic thumper and shots were recorded on a Geometrics^{TM} Strataview^{TM} R48. Five shot points were used: 20 m and 100 m off each end of the line, and a mid shot. At each shot point a stack of 5 thumper shots was recorded. A shot record length of 1024 ms and a sample rate of 0.5 ms were used.

The aim of this seismic survey, together with nearby gravity points and gravity profile, was to confirm greywacke basement depth and dip beneath Wallace Road and help define the broad scale basement structure at the nearby biogenic gas survey site.

5.1.4 Wallace Road south – seismic refraction survey processing

A detailed discussion of the methods used for analysis of seismic refraction survey B1 analysis can be found in appendix B.2. The aim of this processing was to resolve any refractions and find the depth and dip of the greywacke basement under Wallace Road.

- Dead/noisy trace removal

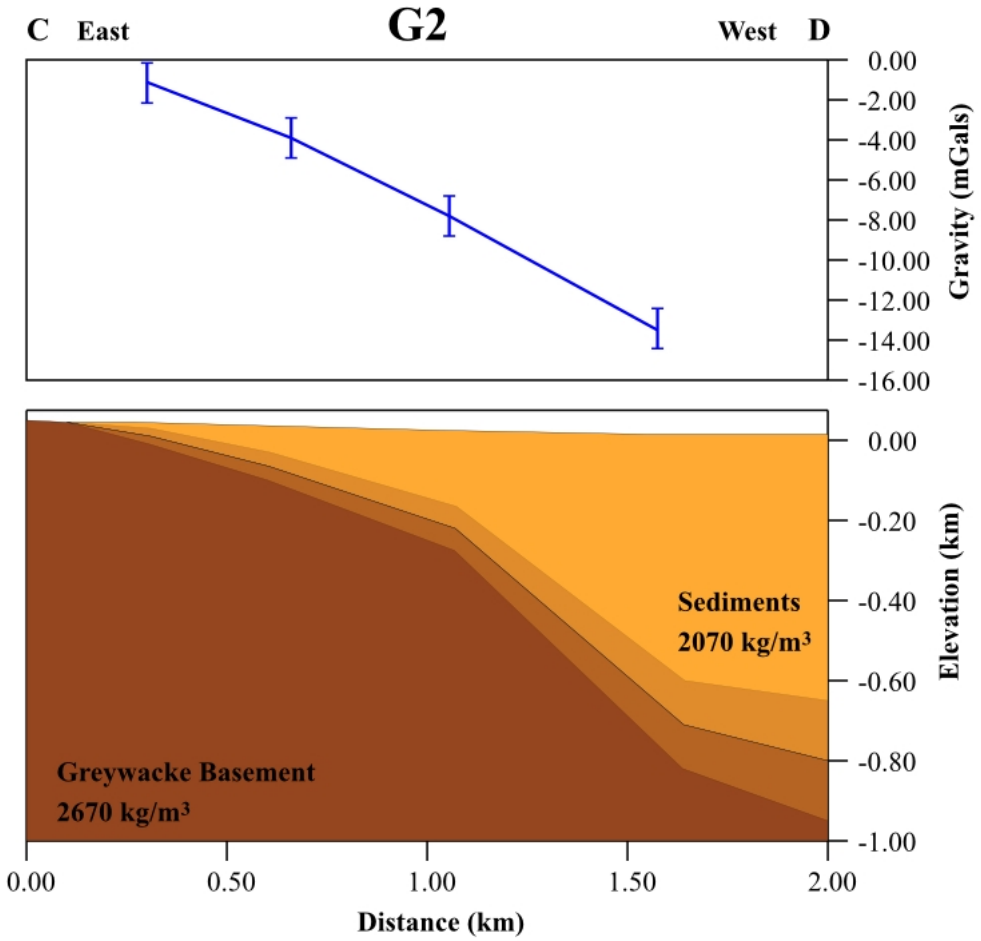

Figure 5.3: Gravity model showing basement depth along Wallace Road. The location of the gravity profile is shown in figure 5.1. Observed gravity with uncertainties (blue error bars) and modelled gravity (blue line) are shown. Densities of $\rho = 2070$ kg/m^3 for sediments and $\rho = 2670$ kg/m^3 for greywacke basement rock were used. Greywacke basement is found to dip gently west then drop sharply near the west end of the line, as in the parallel survey along Muhunoa East Road (figure 4.3). Greywacke basement reaches the surface at the eastern end of the profile where it meets the edge of the Tararua range front, resulting in a residual gravity field of -0.5 mGal. Apart from where it is faulted between 1.1–1.6 km on the profile, the steepest basement dip observed is 14±4° west.

- Frequency domain filter: BP (10 30 80 100) Time Window (0-200 ms)
- Frequency domain filter: BP (30 50 90 110) Time Window (200-600 ms)
- Balance
- AGC: 250 ms window

5.1.5 Wallace Road south – seismic refraction survey interpretation

Refraction 1: Shots from each end of survey B1 refracted along a shallow interface. Analysis of the direct arrival and first refraction in both directions found the velocity in the near surface layer (700±50 m/s), the second layer (1660±100 m/s) and the depth of the layer boundary (2.5±0.5 m).

Refraction 2: In survey B1 a refraction from a third layer was apparent in shots from both directions (figure 5.4). This refraction appeared to have different velocities in different directions leading to the assumption that it was from a dipping layer. In order to analyse this the seismic refraction from a dipping layer method (see appendix B.2.3) was applied to find the velocity, depth and dip of the third layer. It had an updip velocity of 2850±150 m/s (refraction 2a, figure 5.4) and a downdip velocity of 2100±150 m/s (refraction 2b, figure 5.4) which results in a true velocity of 2450±200 m/s (see appendix B.2.3). This third layer was found to have an apparent dip of 9±5^{o} at an azimuth of 292^{o} (figure 5.5). While this is not the true dip, it is likely to be close to the true dip as the B1 line runs perpendicular to the edge of the

Tararua range front.

This third layer does not have a high enough seismic velocity to be greywacke basement, so it is interpreted to be a layer within the river gravels and sediments of the Manawatu plains that overly the basement. The offsets used in the B1 survey were too small to observe refractions from the greywacke basement layer. The older layers of the Manawatu plains would have been laid down horizontally over the greywacke basement, which would subsequently have become tilted with the uplift of the Tararua Ranges. Assuming that no other processes were involved it follows that the dip of the greywacke basement must be at least as great as the dip of overlying layers. This is supported as the maximum dip of the greywacke basement found by the gravity survey G2 was 14±4° west while the dip of an overlying sediment layer found by seismic refraction survey B1 was 9±5° west.

5.2 Wallace Road north – Biogenic gas seismic surveys

The water well (see table 5.1, figure 5.1, 5.6) was drilled at the floor of a narrow east-west trending valley, so the topography limited the lengths of the seismic lines. Both surveys used a geophone spacing of 1 m. This allowed for 48 geophones on the east-west B2 survey and 24 geophones on the north-south B3 survey. Shot offsets from the two ends of the survey lines differed owing to the topography of the site (figure 5.7). Both surveys were also reshot using three-component geophones at 3 m spacing (resulting in

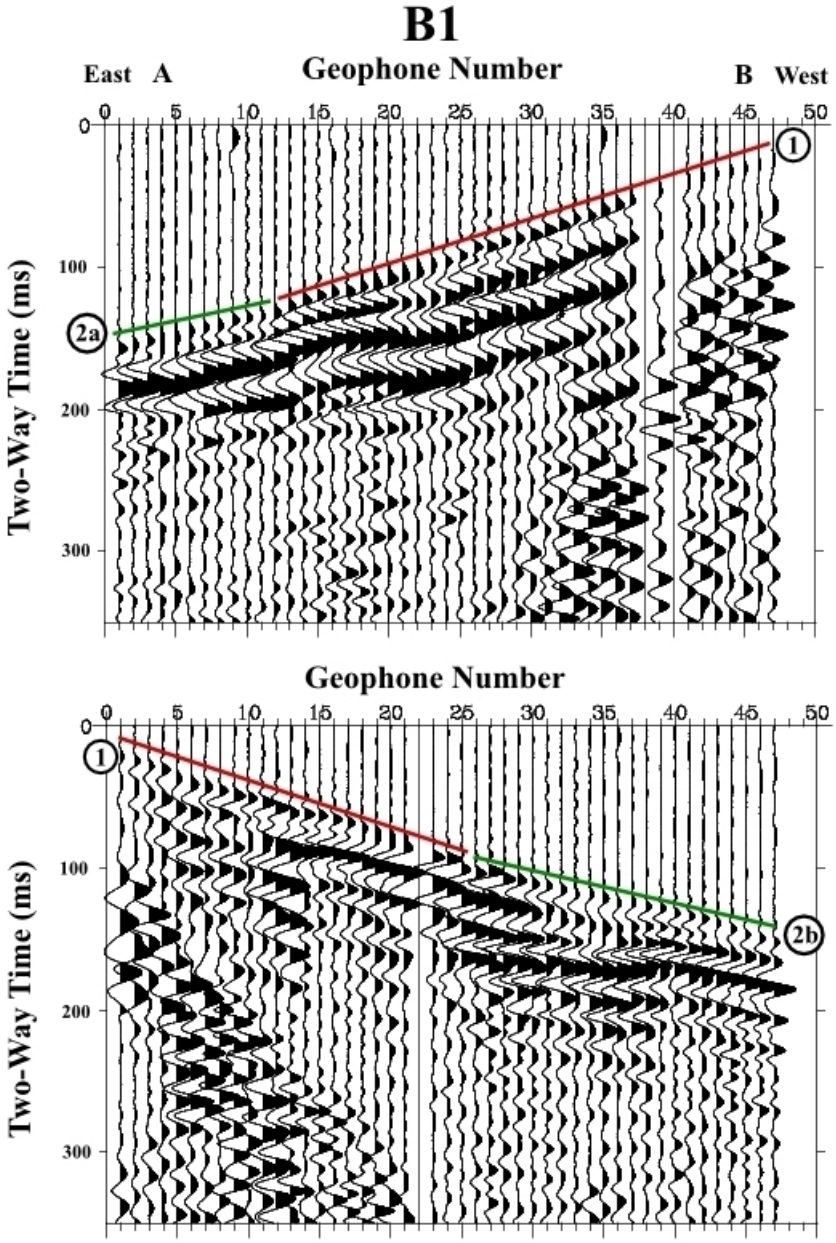

Figure 5.4: Seismic refraction shots from the B1 survey in updip (top) and downdip (bottom) directions. Refractions from the second layer are shown in red, while refractions from the third layer are shown in green. The crossover distance is smaller and the apparent velocity of the third layer is slower in the downdip direction. Velocities of arrivals are 1660±100 m/s (red, 1), 2100±150 m/s (downdip, green, 2b) and 2850±150 m/s (updip, green, 2a). This gives a layer velocity of 2450±200 m/s for the third layer which is slower than the expected velocity range for weathered greywacke.

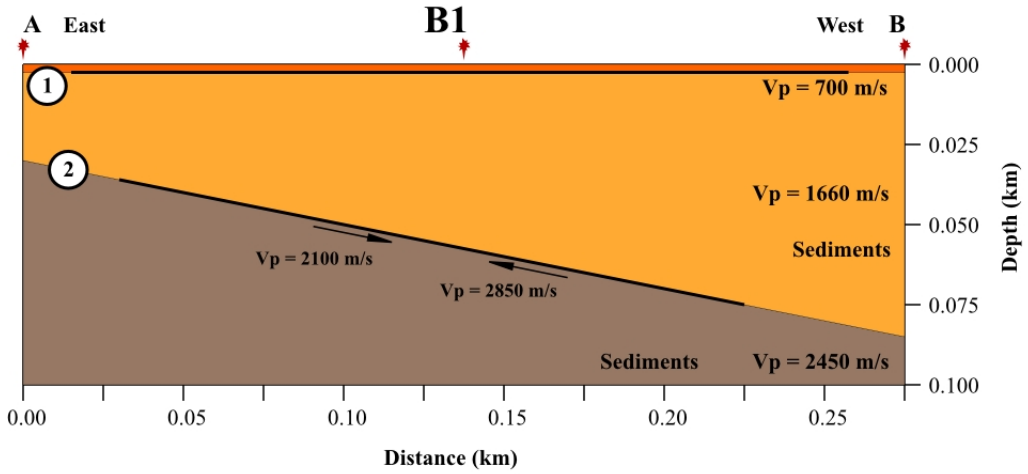

Figure 5.5: Diagram showing layer depths and velocities for B1 refraction survey. The 9±5° dip of the third layer was calculated using the refraction from a dipping layer method (see appendix B.2.3) with updip and downdip refraction velocities. Heavy black lines show which sections of the interfaces were imaged by the seismic survey.

16 three-component geophones for B2 and 8 three-component geophones for B3) to help identify S-wave arrivals. (See appendix B.1.2 for explanation of three-component geophones.) The water table was very close to the surface at the western end of the B2 line, which limited possible shot offset and caused problems for data collection.

The initial aim of these surveys was to resolve seismic refraction and reflection arrivals from the gas sand while preserving amplitude information in order to perform AVO analysis. The known lithology and confirmed presence of gas made this a suitable location to test for amplitude variation with changing offset in the reflection from the known gas layer. This response could then be compared with the seismic signature of the Campion Road survey to determine if the shallow structure at Campion Road was similar to

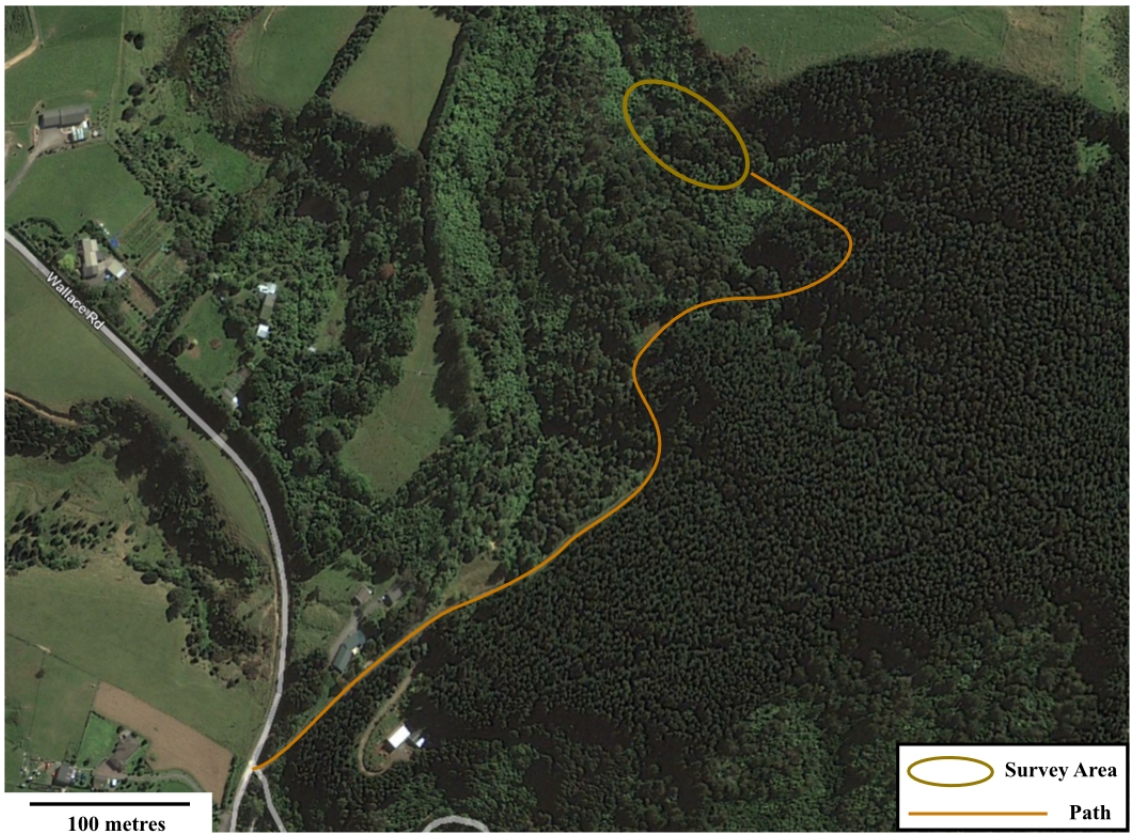

Figure 5.6: Map showing the location of the Wallace Road Biogenic gas seismic surveys. Because of canopy cover a diagram of the seismic survey layout is also provided (see figure 5.7).

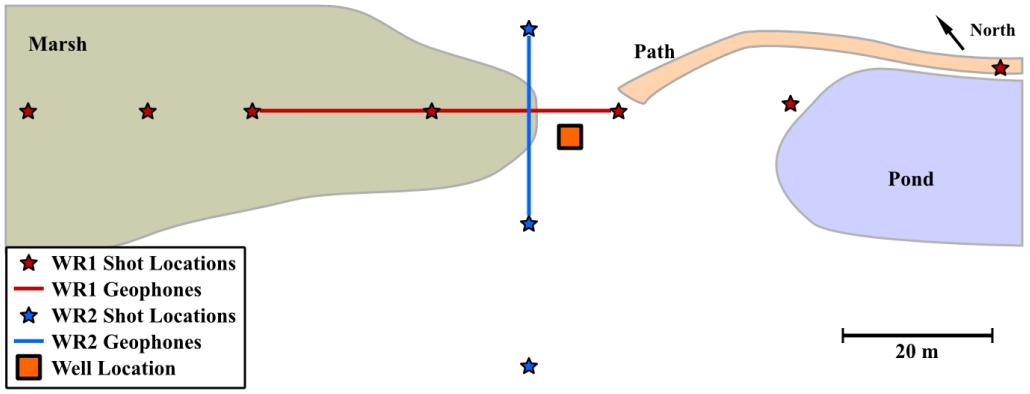

Figure 5.7: Diagram showing geophone deployment and shot locations for B2 and B3 surveys. The surveys were carried out on the floor of an east-west trending valley with survey B2 along the valley floor and survey B3 perpendicular across the valley. Drainage was west down the valley resulting in standing surface water over the western half of survey B2 and the centre of survey B3.

the Wallace Road survey site.

5.2.1 Wallace Road north – seismic survey processing

A detailed discussion of the methods used for analysis of seismic surveys B2 and B3 can be found in appendix B.3. The main aim of this processing was to resolve any seismic refractions and reflections, to determine the shallow structure and to compare calculated depths with the well log. The secondary aim of this processing was to be able to locate reflections from the top of the gas bearing layer and measure how their amplitude varied with changing angle of incidence.

- Dead/noisy trace removal
- Static shift to correct for near-surface effects
- Frequency domain filter: BP (20 40 70 100)

- Balance
- AGC: 100 ms window

Examination of three-component geophone data from both surveys B2 and B3 showed a lack of arrivals with coherent energy in the horizontal directions, probably due to poor coupling between the geophones and the ground from a high water table causing swampy conditions. Because of this, analysis of surveys B2 and B3 was completed using entirely vertical geophone data.

5.2.2 Wallace Road north – seismic survey interpretation

Survey B2

Direct arrival 1: Direct arrival velocity observations in both directions on survey B2 found the near-surface layer to have a velocity of 400±50 m/s.

Refraction 2: A single shot from each end of survey B2 was taken and the plus-minus method (see appendix B.2.4) was applied using the direct arrival and first refraction to obtain the velocity of the second layer (1800±150 m/s) and the depth of the interface (figures 5.9, 5.8). This interface depth was found to vary from 0.5±0.2 m at the western end to 6±0.5 m at the eastern end. This depth at the eastern end of the B2 line corresponded to the base of a peat layer in the well log. The changing thickness of the near surface slow layer on survey B2 was attributed to the shallowing of the water table depth down the valley (to the west).

Reflection 3: was observed in shots from the east end of survey B2 (figures 5.9, 5.8). Curvature and travel time determined it to be a conversion, either a P-wave being reflected as an S-wave or an S-wave being reflected as a P-wave, from a layer interface at 19±1 m. This was compared to the layer depths from the well log data and was determined to be a reflection from the top of the 19.2 m gas-charged sand layer.

Reflection 4: Observed in shots from the east end of survey B2. Curvature and travel time determined it to be a S-wave reflection from the base of the gas-charged sand layer.

Reflection 5: Observed in shots from the east end of survey B2. Curvature and travel time determined it to be a S-wave reflection from a layer interface at 31±2 m. This was compared to the layer depths from the well log data and was determined to be a reflection from either the sand-clay or the clay-gravel boundary at 31 m depth.

Survey B3

Direct arrival 1: Direct arrival velocity observations in both directions on survey B3 found the near-surface layer to have a velocity of 400±50 m/s.

Refraction 2: A single shot from each end of survey B3 was taken and the plus-minus method (see appendix B.2.4) was applied using the direct arrival and first refraction to obtain the velocity of the second layer (1800±150 m/s) and the depth of the interface (figures 5.11, 5.10). This interface depth was found to lie at 6±0.5 m along the whole length of survey B3. This depth corresponded to the base of a peat layer in the well log.

Reflection 3: Observed in shots from both ends of survey B3 (figures 5.11,

5.10). Curvature and travel time determined it to be a conversion, either a P-wave being reflected as an S-wave or an S-wave being reflected as a P-wave, from a layer interface at 19±1 m. This was compared to the layer depths from the well log data and was determined to be a reflection from the top of the 19.2 m gas-charged sand layer.

In survey B2 shots propagating in different directions had distinctly different characteristics (see figure 5.8). The swampy ground conditions over the western half of survey B2 (see figure 5.7) that caused the poor geophone coupling could also have caused a lack of S-wave generation from shots at that end of the survey. It was still possible to record arrivals from S-waves propagating in non-vertical directions as they would have a component of their motion in the vertical direction. This led to the only arrivals recorded from western shots in survey B2 being P waves or P-S conversions. The conversion from the top of the gas-charged sand layer (reflection 3) was visible only on the eastern shots, leading to the conclusion that it was from an S-P conversion not P-S conversion.

In survey B3 reflection 3 was visible but no deeper reflections were observed because of the noisy nature of the data, the limited length of the line and lack of large offset shots (figures 5.11, 5.10). In both surveys B2 and B3 a P-P reflection from the top of the gas-charged sand would be expected to have $t_0 = 30 \pm 2$ ms (see appendix B.4.3). This is the same travel time as for refraction 2, so all P-P reflections were masked by higher amplitude refracted arrivals. The topography of the valley allowed only a limited range of shot offsets to be used so this problem was not overcome.

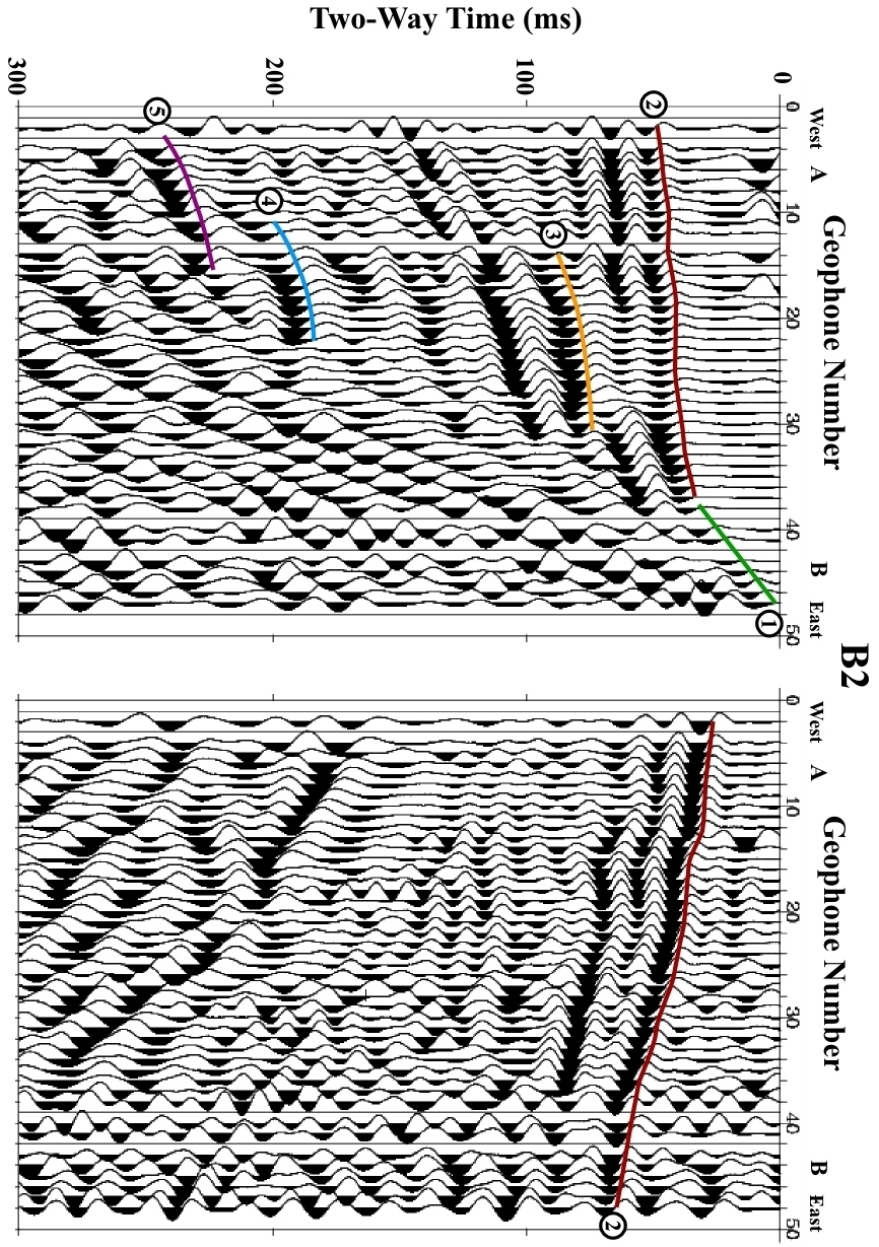

Figure 5.8: Seismic shots from survey B2. Direct arrivals (green, 1, $V_P = 400 \pm 50$ m/s) and refractions from the base of the surface layer (red, 2, $V_P = 1800 \pm 150$ m/s) are shown. Three seismic reflections are also visible in the eastern shot (top); reflection 3: an S-P conversion from the top of the gas-charged sand (orange, 3), reflection 4: an S-S reflection from the base of the gas-charged sand (blue, 4) and reflection 5: an S-S reflection from a deeper interface (purple, 5).

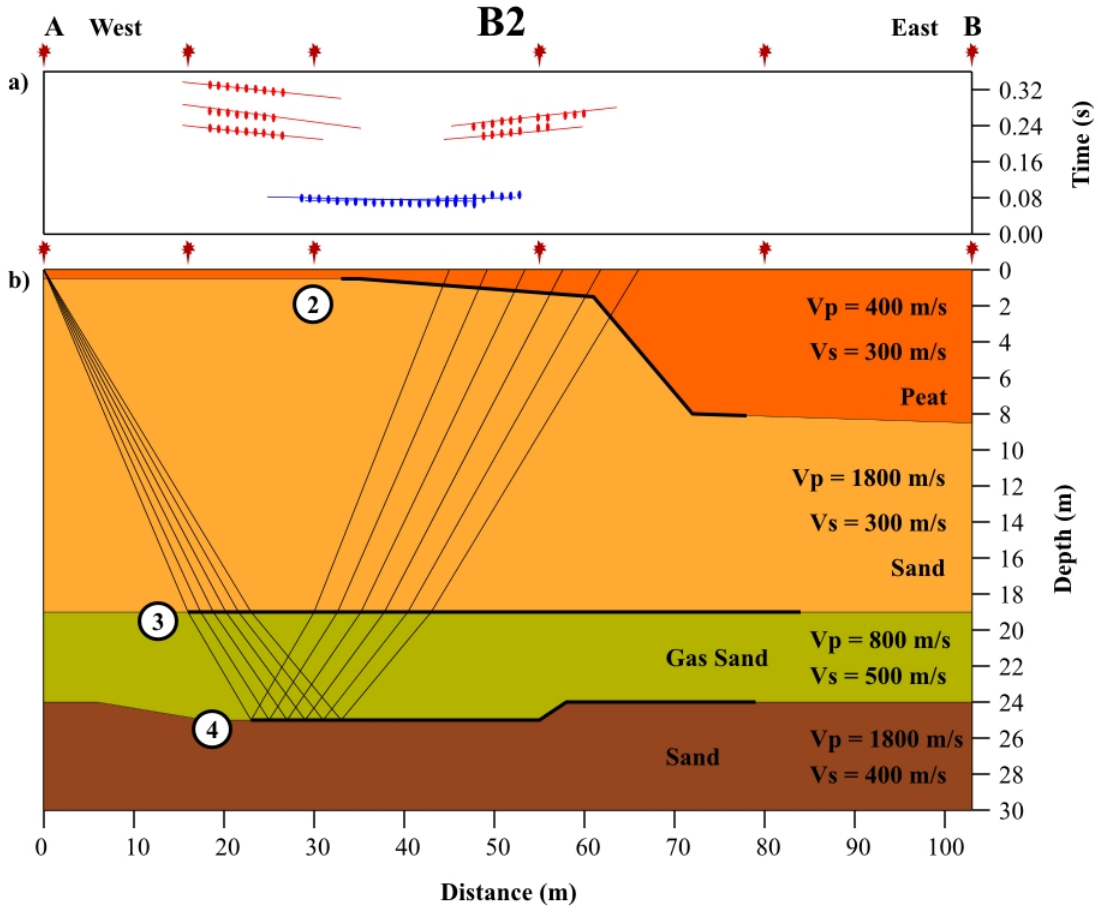

Figure 5.9: Diagram showing layer depths and velocities for survey B2. a) shows the travel times for reflection 3 (blue) and reflection 4 (red) from the top and base of the gas-charged sand layer. Observed travel times are shown as points while predicted travel times from the raytracing model are shown as lines. b) shows layer depths calculated using the plus-minus method (see appendix B.2.4) (top layer boundary) and the reflection from a dipping layer method (see appendix B.4.5) (other two layer boundaries). The third layer (green) is the gas-charged sand layer. Heavy black lines show which sections of the interfaces were imaged by the seismic survey.

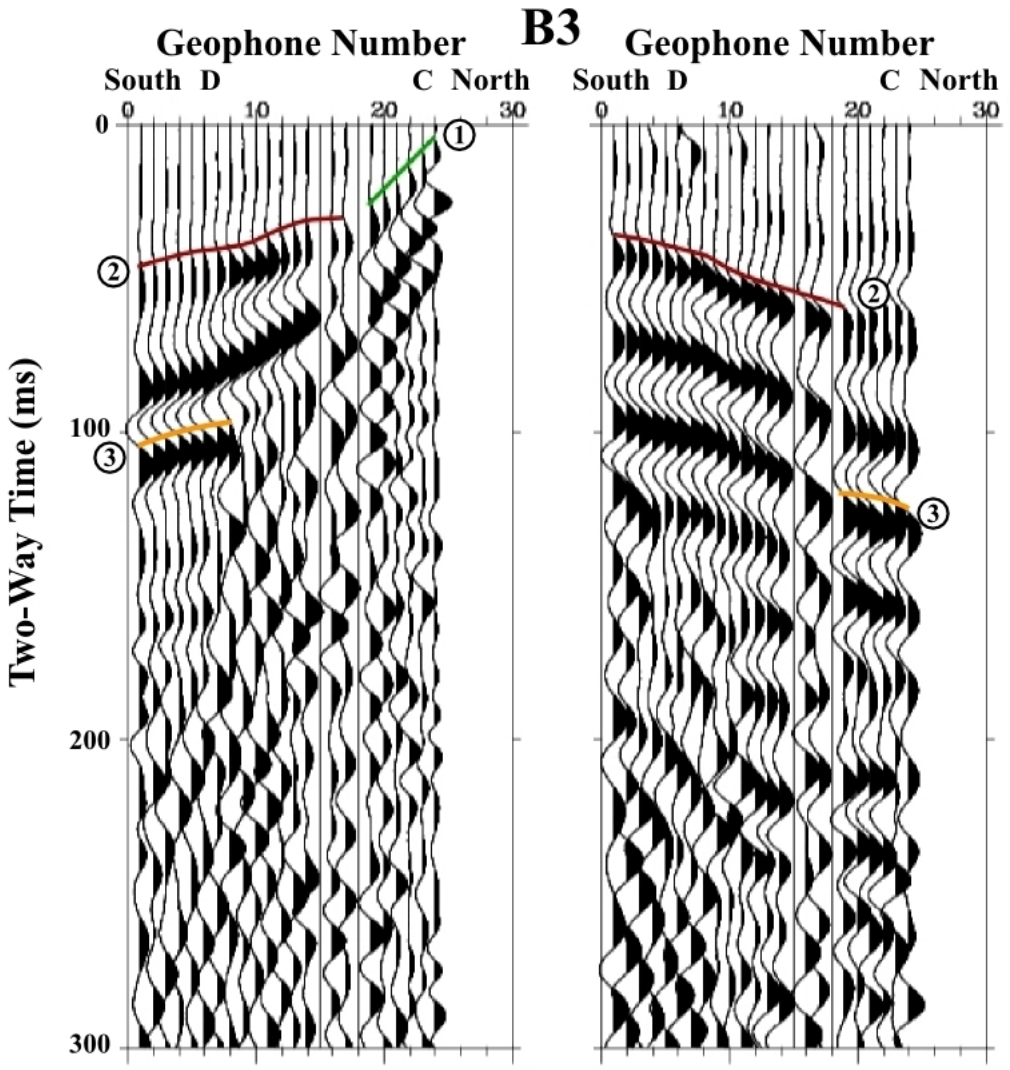

Figure 5.10: Seismic shots from survey B3. Direct arrivals (green, 1, $V_P = 400 \pm 50$ m/s) and refractions from the base of the surface layer (red, 2, $V_P = 1800 \pm 150$ m/s) are shown. Reflection 3: an S-P conversion from the top of the gas-charged sand layer is visible in both directions (orange). No deeper seismic reflections are visible on this survey because of the limited shot offset due to topography.

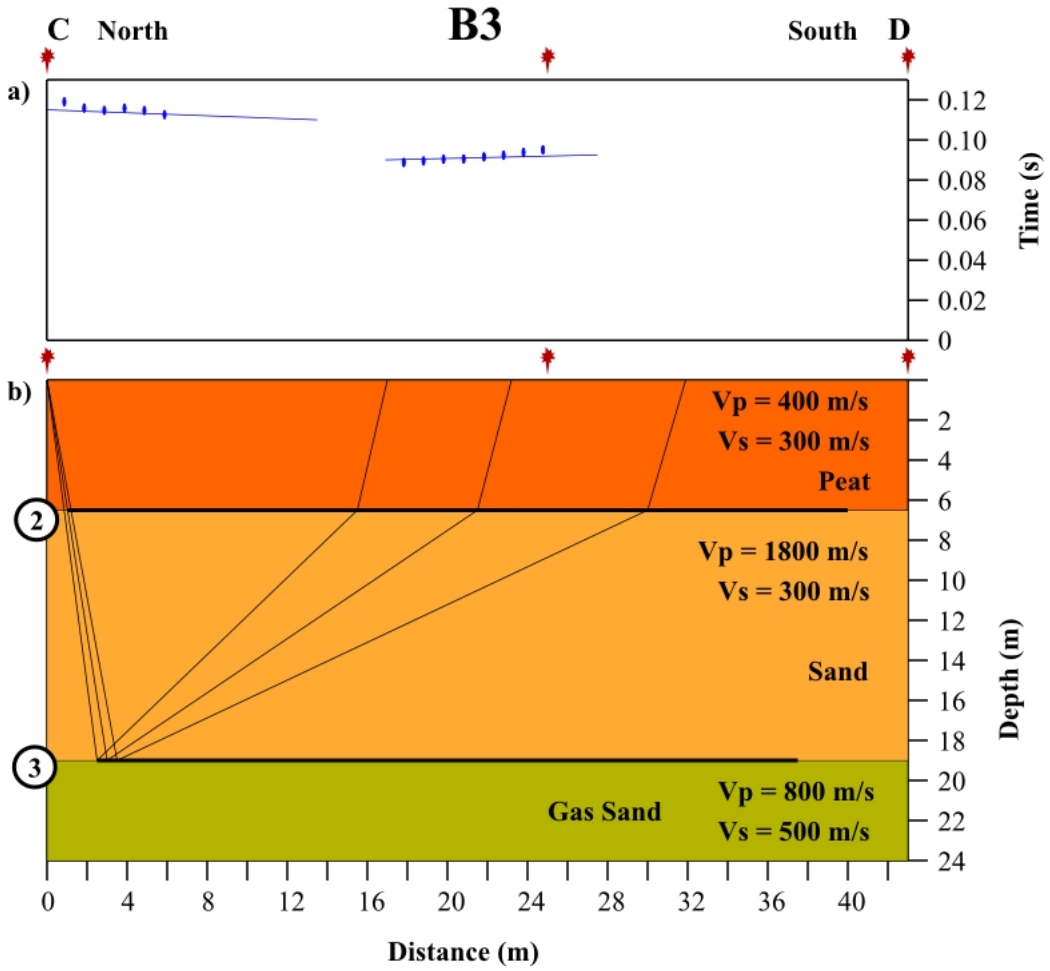

Figure 5.11: Diagram showing layer depths and velocities for survey B3. a) shows the travel times for reflection 3 from the top of the gas-charged sand layer (blue). Observed travel times are shown as points while predicted travel times from the raytracing model are shown as lines. b) shows layer depths, with the depth to the top of the gas-charged sand layer calculated using the reflection from a dipping layer method (see appendix B.4.5). Heavy black lines show which sections of the interfaces were imaged by the seismic survey.

5.3 Wallace Road north – Synthetic modelling and AVO analysis

5.3.1 E3D software modelling

E3D software was used to create synthetic seismograms which were compared with the collected data (see appendix B.6). For the construction of the synthetic seismograms layer depths were constrained using the well data (table 5.1), and the velocity field was constructed using typical velocities for the lithology present. This velocity field was then varied to create a range of synthetic seismograms which were compared to the original data to determine which velocity field gave the best fit (figure 5.12).

The curvatures of the reflections in the synthetic seismogram do not correspond well to the observed reflection curvatures in the survey B2 seismic data (see figure 5.12). A combination of factors could contribute to this discrepancy: variation of the thickness and velocity of the near surface layer or a dipping reflector leading to a seismic reflection where the peak of the curve lies to one side of the shot point (see appendix B.4.5). A static correction was performed on the data using the direct arrival and refraction 2 as guidelines to remove near-surface variation from travel times. If this was successful it would mean that the discrepancy in reflection curvature between the synthetic seismogram and the actual data would be due to the layers' dip or curvature. If this is the case then the direction of offset of the reflection peaks would indicate a westward layer dip which corresponds to the expected slope of layers in the area due to uplift of the Tararua Ranges.

The narrow range of traces over which the reflections are visible in the shot record makes it difficult to determine the angle of dip of the reflector. E3D software is unable to model dipping blocks so this could not be accounted for in the synthetic seismogram. It is unlikely that the near surface effects were completely removed so measuring reflection curvature would not accurately provide layer dip. Also the distance between the observed parts of the reflection curves and the peaks of those curves would introduce a large error into any layer dip estimate.

The velocities used in the synthetic model were reasonable for the sediments present (table 5.2, figure 5.12). The model ignored the slow near-surface layer, so refraction 2 was not present. This layer was not modelled because its presence in the synthetic model introduced multiples throughout the model, making the identification of other arrivals difficult. Not modelling the slow near-surface layer led to the direct S-wave arrival having a similar travel time as reflection 3 at offsets between 10-30 m, making it hard to observe the conversion. In the actual shots the direct S-wave was slower owing to the presence of a slow near-surface layer. All three reflections are present on the synthetic model at correct travel times showing that the model velocities are appropriate.

The expected Poisson ratios for marine sediments at burial depths of less than 600 m tend to fall between 0.45–0.50, but 0.02–0.14 for gas-saturated sediments [Ostrander, 1984]. While Poisson's ratio for the gas-charged sand from the synthetic model does not all fall within the predicted range, there is still a strong change from the gas-charged sand layer to the other layers (see table 5.2). This discrepancy probably arises from the extremely shallow

Depth (m)	**V_P (m/s)**	**V_S (m/s)**	**Density (ρ)(g/cm^3)**	**Poisson's Ratio (σ)**
0 - 19	1800	300	2.20	0.485
19 - 24	800	500	2.10	0.180
24 - 31	1800	400	2.20	0.474
31 +	2000	800	2.20	0.405

Table 5.2: Table detailing layer velocities calculated from E3D synthetic model for use in AVO analysis. Layer depths were constrained using water well log data (see table 5.1), lithology densities from Aharoni [1991] and Ewig [2008] and Poisson's Ratios were calculated from V_P and V_S for each layer.

burial depth of this gas body. Since the Poisson ratios described by Ostrander [1984] were for 600 m burial depth and this body sits at 19 m the overburden pressures are different and the Poisson ratios are not directly comparable.

5.3.2 AVO analysis

Densities and velocities from synthetic modelling were used with Zoeppriz's equations to calculate the reflection coefficients for reflections 3 and 4 at varying incidence angles. The reflection coefficient describes what proportion of the original energy is reflected or converted rather than transmitted at a layer boundary at a certain incidence angle. Reflection 3 was modelled as both a S-P and P-S conversion and reflection 4 was modelled as a S-S reflection. These predicted amplitudes were then compared with the observed data (figure 5.13). Only minimal processing was performed prior to extracting amplitude information from the shot records. Any background seismic noise would contribute to inaccurate amplitude measurements so a frequency

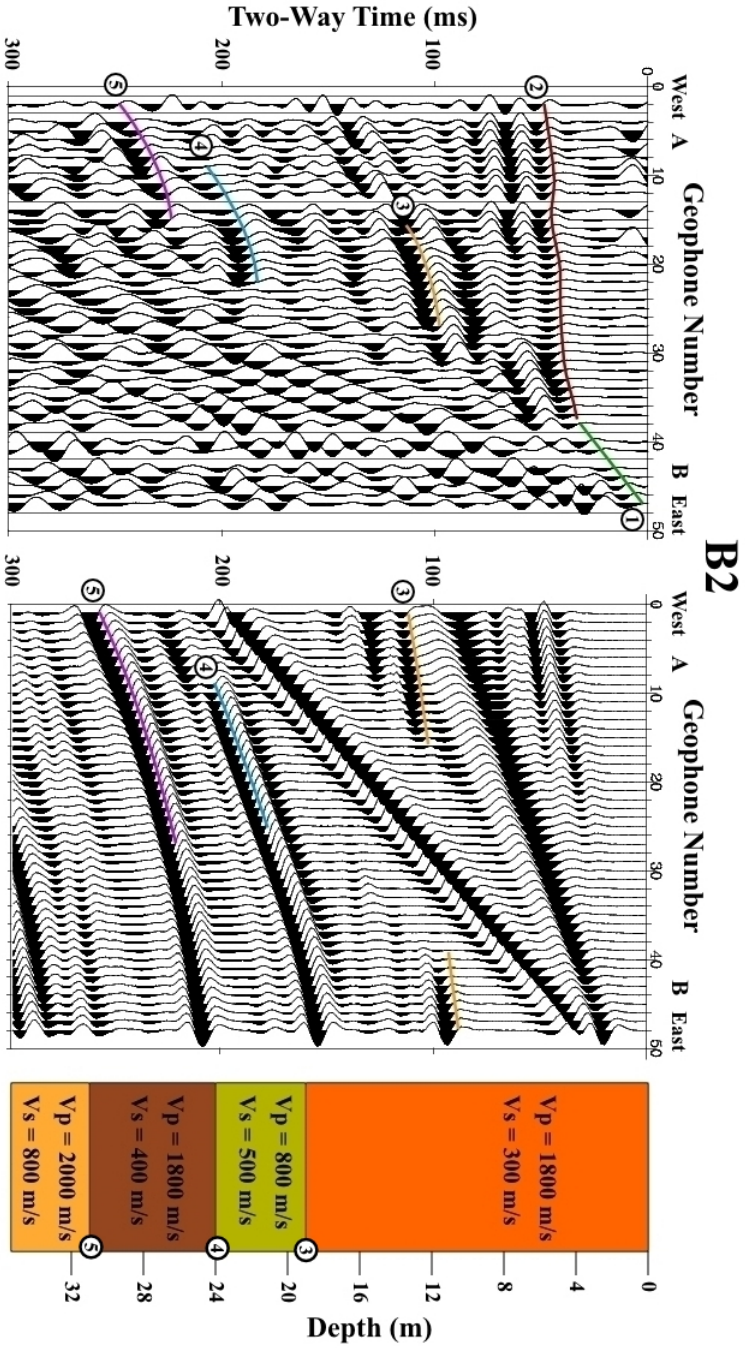

Figure 5.12: Figure comparing a 1 m offset shot from survey B2 (top) with a 1 m offset synthetic seismogram (middle). Reflections 3, 4 and 5 are all identified on the synthetic seismogram. The layer depths and velocities used to construct the synthetic seismogram are also shown (bottom, see table 5.2).

domain filter: BP (30 40 55 75) was applied (see appendix B.5.1). The corner frequencies of this bandpass filter were carefully selected to preserve the frequency content of the reflected arrival.

For reflection 3 the predicted P-S and S-P conversion amplitudes with changing offset show distinct differences from each other (see figure 5.13). Unfortunately due to the large scatter in the reflection 3 data it is not possible to determine which conversion is being observed. The observed S-S reflection 4 amplitudes from the base of the gas-charged sand also show large scatter with no obvious correlation with the predicted amplitudes.

Shots from the western end of the B2 line show a distinctly different character with little ground roll, indicating that the surface conditions at that end of the line were too wet to allow generation of significant S-waves from the source (figure 5.8). The conversion from the top of the gas-charged sand is not visible on shots from the west end of the line, indicating that the conversion observed is the S-P conversion.

5.4 Wallace Road survey summary

Four new gravity points (figure 5.2) were collected along Wallace Road and a gravity profile (figure 5.3) was constructed in the same location as seismic line B1 (figure 5.5) perpendicular to the Tararua range front. The gravity profile found basement depth to be similar to that found beneath Muhunoa East Road (see figure 4.3). Seismic line B1 showed an interface between sedimentary layers to dip 9 ± 5^{o} at an azimuth of 292^{o} while gravity survey G2 found the greywacke basement to dip 14 ± 4^{o} west. Sedimentary layers in

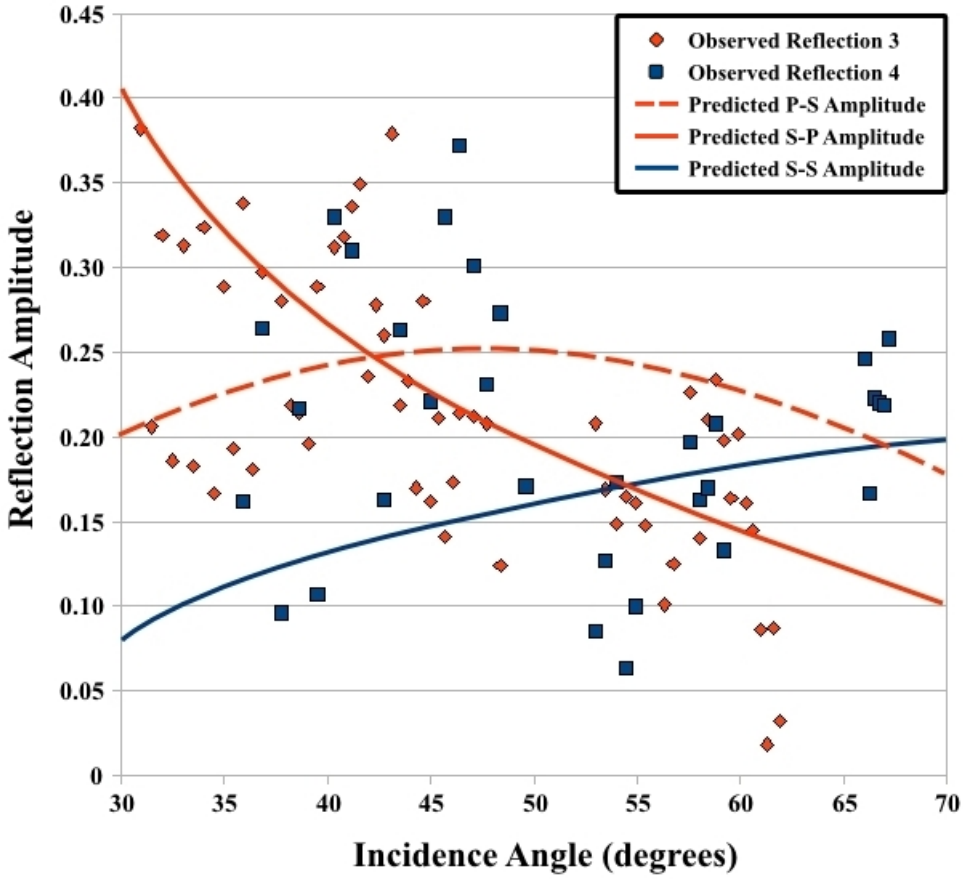

Figure 5.13: Plot showing the predicted and observed amplitudes of reflections 3 and 4 for varying angle of incidence in survey B2. The points are calculated from seismic traces showing the observed amplitude relative to the source energy of either the conversion from the top of the gas-charged sand or the reflection from the base of the gas-charged sand. The predicted reflection amplitudes were calculated using Zoeppritz's equations and refer to the proportion of the incident energy at the layer boundary that is reflected or converted rather than transmitted. The dashed orange line is the predicted P-S conversion amplitude, the hard orange line is the predicted S-P conversion amplitude and the hard blue line is the predicted S-S reflection amplitude.

this area would have been laid down horizontally and subsequently tilted by the uplift of the Tararua Ranges, so the greywacke basement having a similar or greater dip to the overlying sedimentary layer is a reasonable result. This seismic line combined with new gravity data points and gravity profile shows nothing unusual about the basement structure near Wallace Road that should lead to gas accumulation.

Seismic survey B2 was able to resolve 3 reflected arrivals from different layers: reflection 3, an S-P conversion from the top of the gas-charged sand layer at 19 m depth; reflection 4, an S-S reflection from the base of the gas-charged sand layer at 24 m depth; and reflection 5, an S-S reflection from a layer boundary at 31 m depth.

A synthetic seismogram was created with E3D software using layer depths from the water well data (table 5.1) and an initial velocity field based on the lithologies present. The velocity field was then varied and checked by comparing the reflection arrival times on the synthetic seismogram with the observed arrivals. Poisson's ratio was shown to be significantly lower in the gas-charged sand layer (0.180) than in the surrounding layers (0.485, 0.474). (See table 5.2.) This was the expected result for shallow gas-saturated marine sediments [Ostrander, 1984].

The expected amplitudes of reflections 3 and 4 were modelled with Zoeppritz's equations using layer depths from the water well log (table 5.1) and velocities from the E3D synthetic modelling (table 5.2), and compared with the amplitudes of the observed arrivals. The observed amplitudes showed a large scatter with no correlation to the predicted amplitudes because of a poor signal-to-noise ratio in the recorded data. For reflection 3 it was not

possible to determine if it was the P-S or S-P conversion being observed. The observed reflections were also visible over only a narrow range of traces, making it difficult to measure their curvature; so dip or curvature of the layers could not be determined.

The swampy nature of the ground limited S-wave generation from shots at the west end of survey B2 and led to a poor signal-to-noise ratio. This also supported the conclusion that reflection 3, the conversion from the top of the gas-charged sand, was an S-P not P-S conversion, since it was visible only on shots from the east end of B2. In survey B3 reflections 4 and 5 were not visible because the topography limited the shot offset and line length.

Chapter 6

Campion Road – Potential biogenic gas survey

An airborne resistivity survey carried out over the Manawatu region identified a high resistivity anomaly of approximately 1 km^2 near Campion Road (figure 6.1) [Proposed Geoprobe Programme, PEP 38771 Report, Ian R Brown Associates Ltd]. Campion Road is a side road off State Highway 1 approximately 8 km southwest of Sanson (figure 1.1). Groundwater is conductive, so one cause of high resistivity is the absence of groundwater. Groundwater can be displaced from the pore space of a rock by the presence of trapped gas, so a high resistivity anomaly could indicate the presence of a buried gas body. The resistivity survey showed the high resistivity zone to have an upper boundary at approximately 20 m depth.

The aim of this study was to use seismic surveys to find the depth and extent of the high resistivity anomaly (figure 6.2). An initial seismic refraction survey (C1) was shot over the anomaly to confirm the presence or

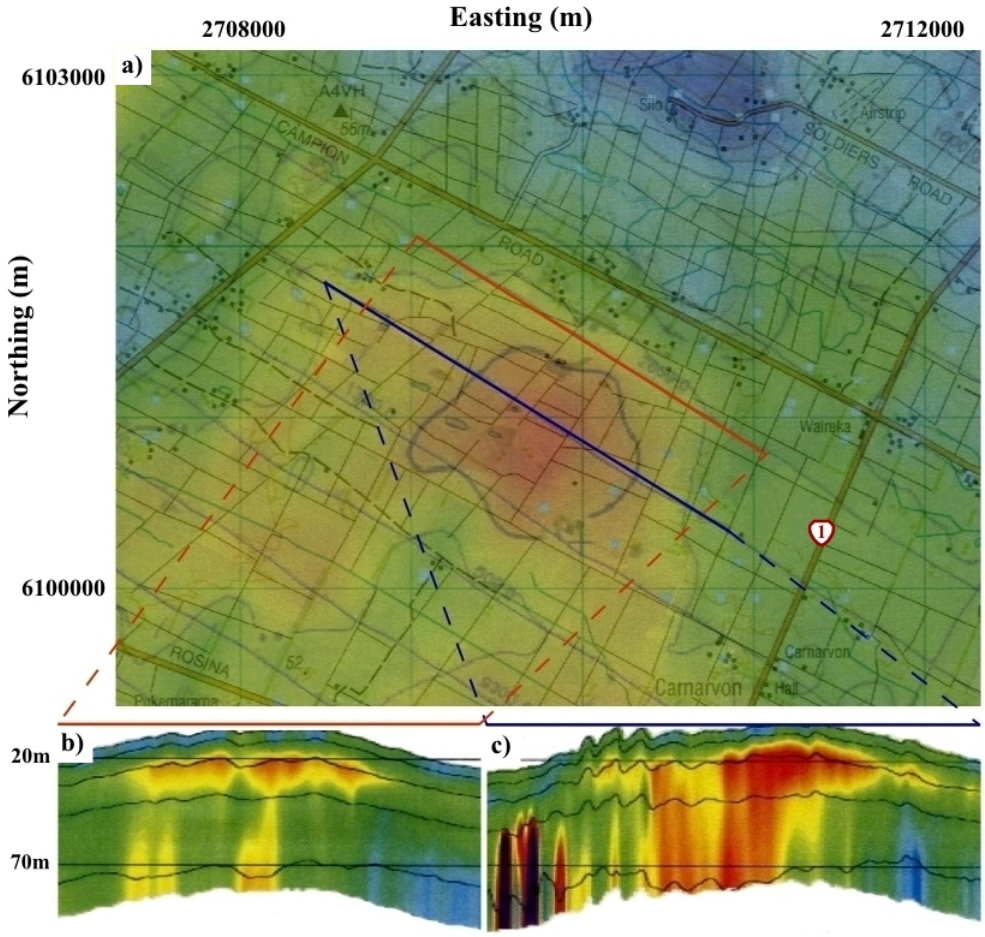

Figure 6.1: a) Plot showing the lateral extent of the high resistivity anomaly at Campion Road. The diagonal lines are the aerial transects flown. b) Aerial transect showing the northern edge of the high resistivity anomaly. c) Aerial transect passing through the centre of the high resistivity anomaly. Figure is from [Proposed Geoprobe Programme, PEP 38771 Report, Ian R Brown Associates Ltd]. The red areas indicate high resistivity and the blue areas low resistivity. Unfortunately airborne resistivity surveys don't produce consistant scales and no resistivity scale was supplied in the report. Map scale is New Zealand Map Grid (NZMG), squares are 1 km.

323031		**323092**	
Depth (m)	**Description**	**Depth (m)**	**Description**
1-7	Clay	1-11	Silt/Sand
7-14	Sand	11-13	Clay
14-24	Gravel Sand	13-26	Coarse Sand
24	Silty Clay	26-30	Clay
24-29	Gravel Sand		
29-36	Fine Sand		

Table 6.1: Table detailing lithologies present from water well logs near Campion Road survey site. See figure 6.2 for water well locations.

absence of a layer boundary at approximately 20 m depth. As a comparison a second seismic refraction survey (C2) was shot to the north of the anomaly to compare the layer depths and seismic velocities over the anomaly with those in the surrounding area. Seismic reflection surveys were then used to image the edge (D2 and D3) and middle (D1) of the anomaly. The results of these surveys could then be compared with the seismic signature of the known biogenic gas deposit at Wallace Road to determine if the high resistivity anomaly at Campion Road was caused by biogenic gas displacing the local groundwater.

Well logs from two nearby water wells 323031 and 323092 (figure 6.2, table 6.1) showed interspersed clay and sand layers. Both wells fell approximately the same distance from the Rangitikei River as the resistivity anomaly (4 km east of the river) and were 2 km northeast and 1 km southwest of the anomaly. Because of the fairly even subsidence of this region both well logs gave a good indication of the subsurface structure expected near the anomaly, particularly for surveys C2 and D3 which were not over the anomaly itself.

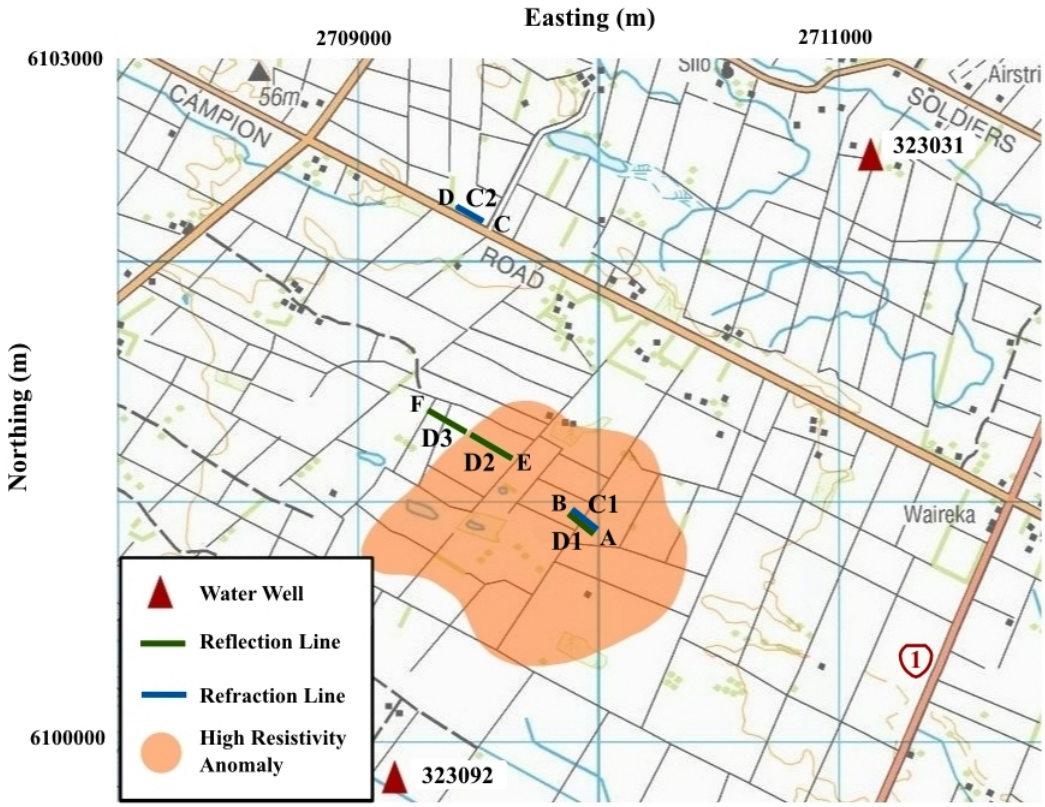

Figure 6.2: Map of Campion Road survey site showing the extent of the high resistivity anomaly, the locations of the seismic lines and water wells in the area. Scale is in New Zealand Map Grid (NZMG), squares are 1 km.

6.1 Campion Road seismic refraction surveys

Two preliminary seismic refraction surveys were carried out, one over the centre of the anomaly (C1, figure 6.2) and one running parallel along Campion Road (C2). The aim of survey C1 over the centre of the anomaly was to confirm the presence or absence of a layer boundary at around 20 m depth, and whether this layer was flat or dipping. Survey C2 was shot north of the anomaly and compared with survey C1 to determine if the shallow structure changed from over the anomaly to the surrounding area.

For both refraction surveys 48 vertical geophones were used with a geophone spacing of 1 m. The seismic source was sledgehammer on an iron rail and shots were recorded using a Geometrics^{TM} Strataview^{TM} R48. Stacks of 5-8 shots were recorded for each shot location. Five shot locations were used for each survey: 1 m and 20 m off each end of the line, and a mid-shot. Both surveys were then repeated using 16 three-component geophones placed at 3 m intervals instead of vertical geophones. By shooting the same surveys again using three-component geophones the horizontal components of detected arrivals could be measured, potentially leading to the identification of S-wave arrivals and a better understanding of the layers and velocity structure present.

6.1.1 Campion Road seismic refraction survey processing

A detailed discussion of the methods used for analysis of seismic refraction surveys C1 and C2 can be found in appendix B.3. The aim of this processing

was to resolve any refractions and find the depth and dip of any layers in the near surface. The aim of the processing applied to the three-component geophone shots was to resolve any arrivals not observed on the geophone shots to build a more complete picture.

- Dead/noisy trace removal
- Frequency domain filter: BP (10 20 80 100)
- Balance
- AGC: 250 ms window

6.1.2 Campion Road seismic refraction survey interpretation

Survey C1 - Over the resistivity anomaly

Direct arrival 1: Direct arrival velocity observations in both directions found the near-surface layer to have a velocity of 750±50 m/s (figure 6.3, figure 6.4).

Refraction 2: A refraction from the second layer was apparent in shots from both directions (figure 6.3) and had a layer velocity of 1160±100 m/s. The refracted waves were observed to have the same velocity in both directions leading to the conclusion that they were from a horizontal layer. This refraction was calculated to come from an interface at a depth of 23±1 m (see appendix B.2.2).

Reflection 2: Analysis of the three-component geophone data (figure 6.5) showed an observable reflection in the in-line horizontal components of the

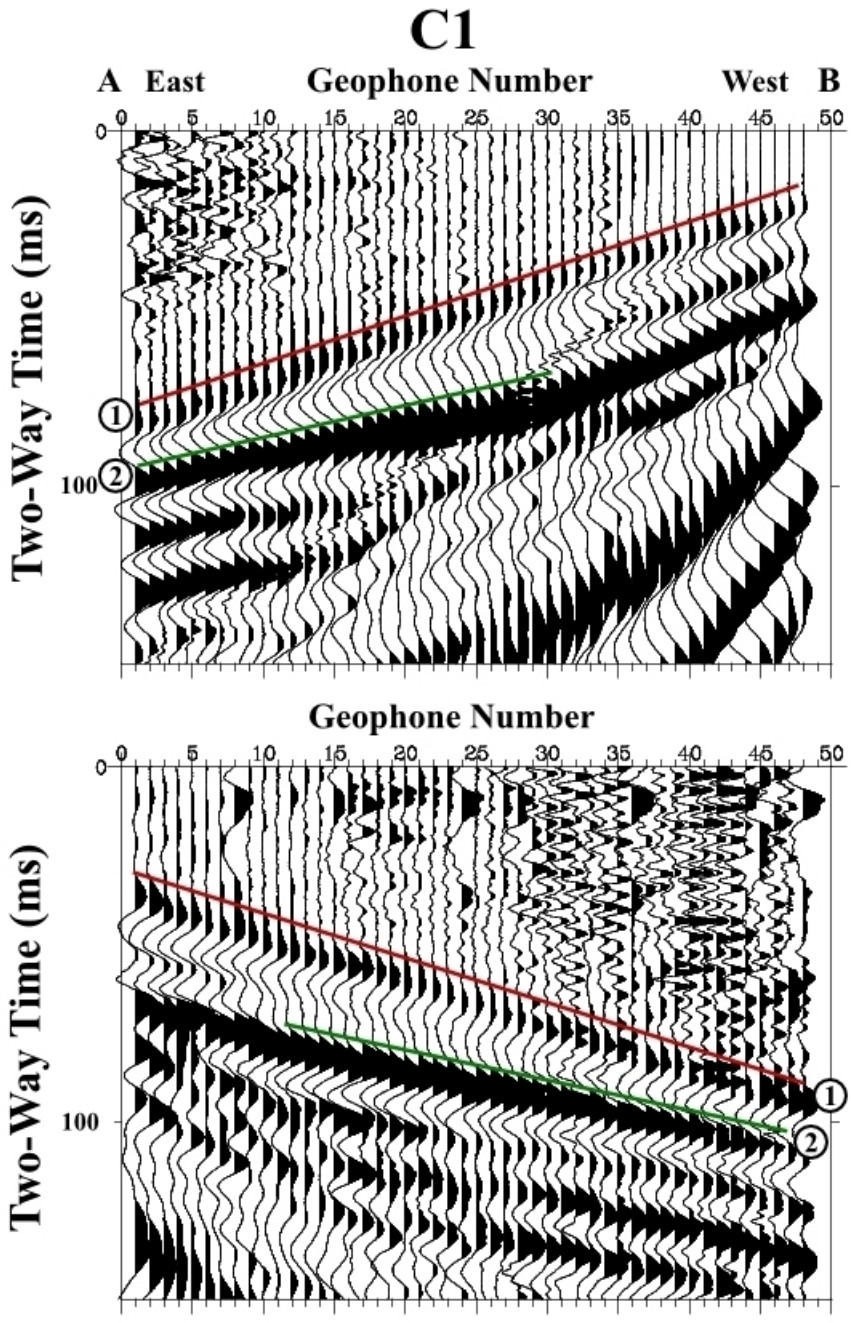

Figure 6.3: Seismic refraction shots from survey C1. Direct arrivals (red, 1, V_P = 750±50 m/s) and refractions from the second layer (green, 2, V_P = 1160±100 m/s in both directions). The shot offsets were not large enough for the crossover distance or any deeper arrivals to be observed.

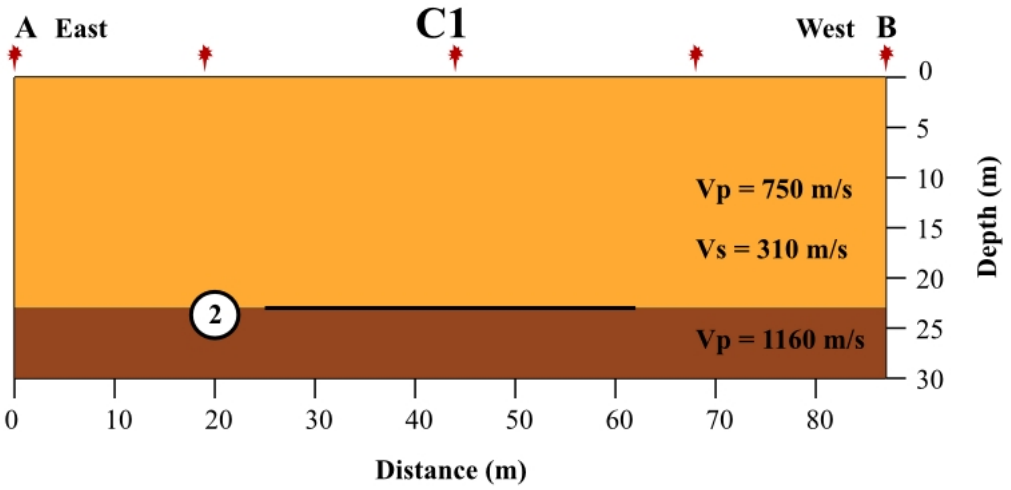

Figure 6.4: Diagram showing layer depths and velocities for survey C1. Refraction/reflection 2 from the layer boundary at 23 m depth is shown. The heavy black line shows the extent of the interface that was imaged.

20 m offset shots in both directions (figure 6.5). Measuring the curvature of the reflection gave a V_{rms} value of 450±50 m/s and T_0 value of 107±5 ms (see appendix B.4.3). This translated to an interface depth of 24±4 m which corresponded well to the depth obtained from seismic refraction data. The V_{rms} for reflection 2 was 450±50 m/s while the V_P for the top layer was 750±50 m/s, leading to the conclusion that reflection 2 was in fact a conversion from the 23 m layer boundary and that the top layer had an S-wave velocity of 310±50 m/s. Reflection 2 was not apparent in the vertical geophone data (figure 6.3) yet it was clearly visible in the horizontal components of the three-component geophone data (figure 6.5), indicating that it was likely a P-S conversion with the majority of its energy arriving in the horizontal component directions. The amplitudes of these reflected arrivals were analysed using Zoeppritz's equations in an attempt to confirm

whether this was a P-S or S-P conversion. The small number of traces over which the reflection was visible and poor signal-to-noise ratio of the data made it impossible to determine any trend in the variation of amplitude with offset, so this analysis provided no indication of which type of conversion was being observed.

Survey C2 - North of the resistivity anomaly

Direct arrival 1: Direct arrival velocity observations in both directions found the near-surface layer to have a velocity of 550±50 m/s (figure 6.6, figure 6.7). From the observed velocity and comparison with the nearby water well logs (table 6.1) this layer was interpreted as likely a thin clay layer.

Refraction 2: A refraction from the second layer was apparent in shots from both directions (figure 6.6) and had a layer velocity of 1750±100 m/s. These refracted waves were observed to have the same velocity in both directions leading to the conclusion that they were from a horizontal layer. This refraction was calculated to come from an interface at a depth of 3.5±0.5 m (see appendix B.2.2). From the observed velocity and comparison with the nearby water well logs (table 6.1) this layer was interpreted as likely a sandstone or siltstone.

Offsets were not large enough to observe refractions from any deeper layers on either of surveys C1 and C2. Three-component geophone records from survey C2 showed no indication of reflections on the horizontal components as was seen on survey C1. The second layer of V_P = 1750±100 m/s beneath survey C2 was found to be much shallower than the V_P = 1160±100 m/s layer beneath C1, indicating a significant difference in shallow structure

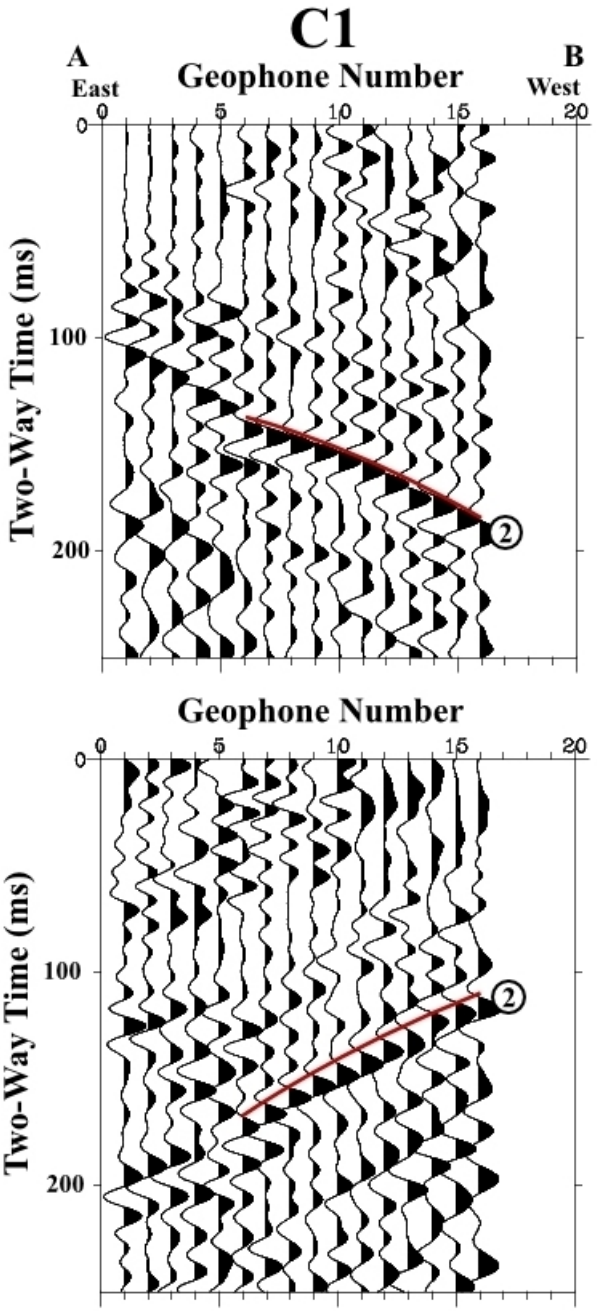

Figure 6.5: The in-line (east-west) horizontal component from the three-component geophone shots in survey C1. Reflection 2, the conversion from the 23 m layer boundary (red), is shown in both directions.

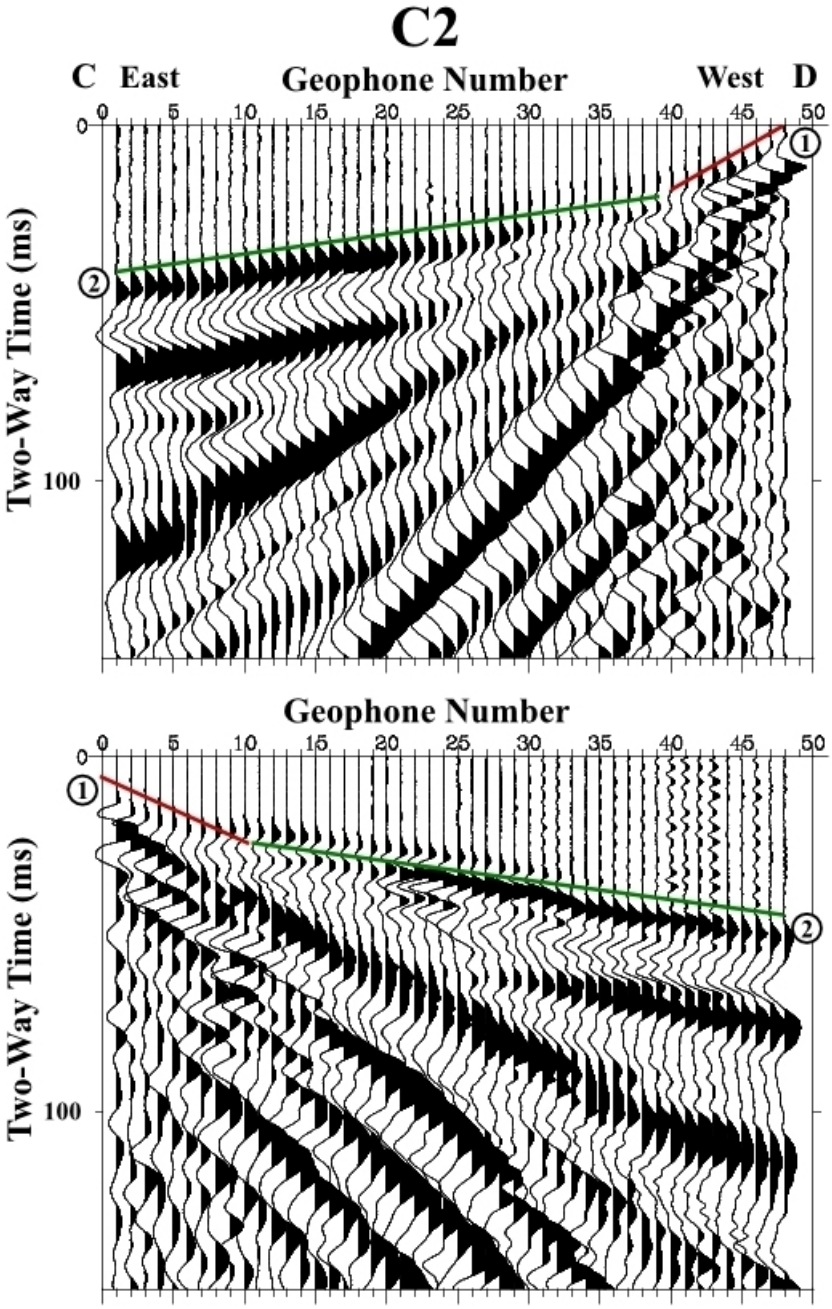

Figure 6.6: Seismic refraction shots from survey C2. Direct arrivals (red, 1, V_P = 550±50 m/s) and refractions from the second layer (green, 2, V_P = 1750±100 m/s in both directions). No deeper arrivals were observed.

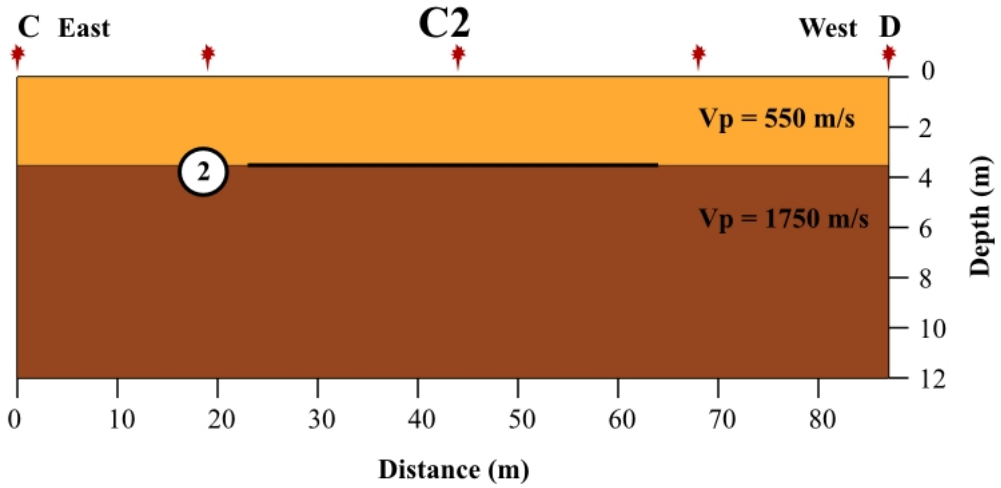

Figure 6.7: Diagram showing layer depths and velocities for survey C2. Refraction/reflection 2 from the layer boundary at 3.5 m depth is shown. The heavy black line shows the extent of the interface that was imaged. The fast layer lies at a much shallower depth than in survey C1.

from above the resistivity anomaly compared to north of it. This provided an indication that the resistivity anomaly correlated with a change in shallow structure regardless of the presence or absence of biogenic gas.

6.2 Campion Road seismic reflection surveys

Three seismic reflection surveys were collected to complement the seismic refraction surveys. Surveys D2 and D3 were placed adjacent to each other across the western edge of the anomaly as defined by the airborne resistivity survey. Survey D1 was conducted over the centre of the anomaly in the same location as survey C1 (figure 6.2).

For surveys D2 and D3 96 vertical geophones were used for each survey with a geophone spacing of 2 m. Data were recorded on a Geometrics^{TM}

Strataview^{TM} R48. The R48 was capable of recording data from only 48 channels at a time, so a rollbox with 96 channels was used to select which 48 channels were active for each shot. For survey D2 the shot offset was always 2 m from the nearest active geophone. For each shot the active geophones and shot location were rolled along by 4 m resulting in 24 shot locations. For survey D3 the shot offset was changed to 10 m from the nearest active geophone in order to better avoid interference between the direct arrival and the reflection from the top of the second layer. In survey D2 the shot locations were always to the west of the geophones, while in survey D3 shots were recorded off both east and west ends of the active line. For survey D1 48 geophones were placed at 2 m spacing. Shots began at 10 m offset from the end of the line and the shot point was moved 4 m for each shot resulting in different survey geometries for each shot.

Survey D2 was begun using a single shot from a hydraulic thumper at each shot location, but after 16 shots the mechanism used to raise the thumper broke so the survey was completed using stacks of 8 sledgehammer shots at each shot location. Surveys D3 and D1 were collected using entirely stacks of sledgehammer shots. All shots were recorded at a 250 μs sampling rate using record lengths of 2048 ms.

The gap left between surveys D2 and D3 was due to the presence of fences and a track that would have been difficult to run a single survey across. The western edge of the resistivity anomaly as defined by the airborne survey fell directly between surveys D2 and D3. The aim in placing surveys D2 and D3 across the edge of the resistivity anomaly was to identify any change in seismic characteristics across the boundary. Survey D1 was conducted over

the centre of the anomaly in the same location as survey C1. This was to provide a direct comparison of a seismic reflection to a seismic refraction survey over the anomaly, and to allow comparison with the D2 survey to examine whether the anomaly changed characteristics between its centre and edge.

6.2.1 Campion Road seismic reflection survey processing

A detailed discussion of the methods used for analysis of seismic reflection surveys D2, D3 and D1 can be found in appendix B.5. The aim of this processing was to resolve and examine the seismic characteristics of any reflector at a depth of between 15-30 m that might correspond to the observed resistivity anomaly. All three seismic reflection surveys had the same processing steps applied, although statics, FK filters and velocity fields were picked individually for each survey.

- Dead/noisy trace removal
- First break removal
- Static shift to correct for near-surface effects
- Frequency-wavenumber filter
- Frequency domain filter: BP (10 20 80 100)
- Spherical divergence
- Balance

- Traces sorted by CDP
- Brutal stack created
- Velocity field created (see appendix B.5.3 for methods used)
- Stack created using picked velocity field
- Post-stack AGC: 300 ms window

6.2.2 Campion Road seismic reflection survey interpretation

Seismic reflection surveys D2 and D3 (figure 6.8) show a packet of highly coherent reflections from 60-150 ms TWTT. The top of this reflection packet is relatively flat, is observable for the whole length of survey D2 and ceases 40 m into survey D3. A similar packet of reflections with a relatively flat upper boundary is visible at 80 ms across the entire length of survey D1 (figure 6.9). The velocity and TWTT of these reflections indicate that they come from a layer at 24 m depth, which corresponds well with the 23 m layer boundary observed on seismic refraction survey C1 over the centre of the resistivity anomaly. The stacking velocity for survey D2 and the eastern half of survey D3 increases strongly for the western half of survey D3 (figure 6.10), indicating a significant change in subsurface structure. While there are no bright reflectors in the western half of survey D3, a clear increase in the velocity structure was noticable in both the semblance analysis and the constant velocity gather (see appendix B.5.3). The location of this slower stacking velocity corresponds to the area of high resistivity located by the

airborne survey, and the increase in shallow velocity away from the resistivity anomaly is backed up by the results of refraction survey C2 to the north.

The initial hypothesis was that the presence of the high resistivity anomaly was due to groundwater being displaced by biogenic gas. Organic matter in peat-rich sediments, even without gas present, absorbs water and causes clay particles to aggregate, creating an open structure that is weak and easy to deform. This leads to increased compressibility which lowers the acoustic velocity [Missiaen *et al.*, 2002]. The areas outside the resistivity anomaly (western half of D3 line and whole C2 line) show no sign of any low velocity layer, while the anomaly has a compressional velocity 1200±100 m/s. Interval velocities were calculated from the stacking velocities using the Dix equation (see appendix B.4.4). A depth of 24 m is well below the expected water table. This layer has no water, otherwise the compressional velocity would be at least 1500 m/s. Stacking velocities also showed layer 2 to have a thickness of 45±5 m and the third layer to have V_P = 3375±500 m/s (using the Dix equation).

The simplest explanation for this low seismic velocity and highly reflective interface coinciding with a high resistivity anomaly is that the groundwater has been displaced by gas in either a gas-charged sand or a gas-charged peat body. A velocity of 1200±100 m/s falls within the expected range for a gas-charged peat body [Missiaen *et al.*, 2002]. It is likely that the presence of gas in the layer formed a channel with acoustic impedance contrasts above and below in which the seismic signal reverberated creating the packet of highly coherent reflections observed.

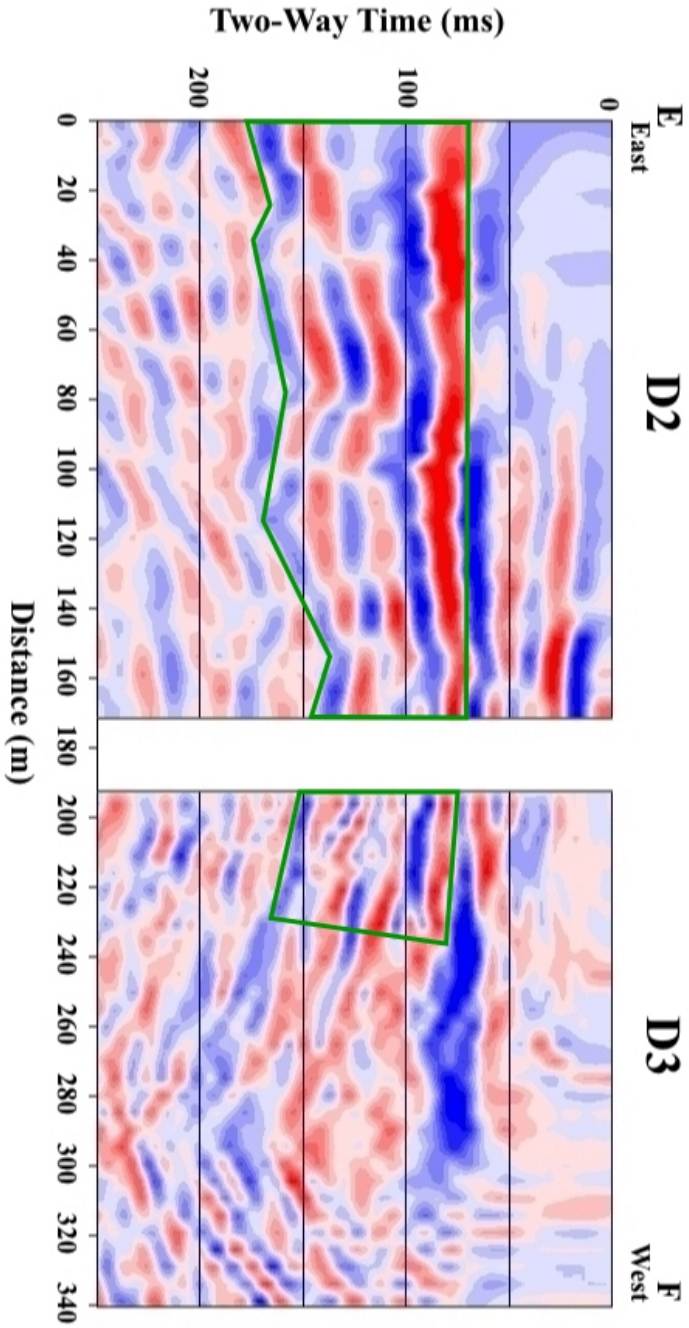

Figure 6.8: Final stacked section for surveys D2 and D3. The packet of highly coherent reflection from 70-150 ms TWTT is outlined. The top of the bright reflections corresponds to the 23 m layer boundary at the top of the resistivity anomaly. The edge of the anomaly can be observed in the middle of survey D3 where there is a strong change in the seismic character.

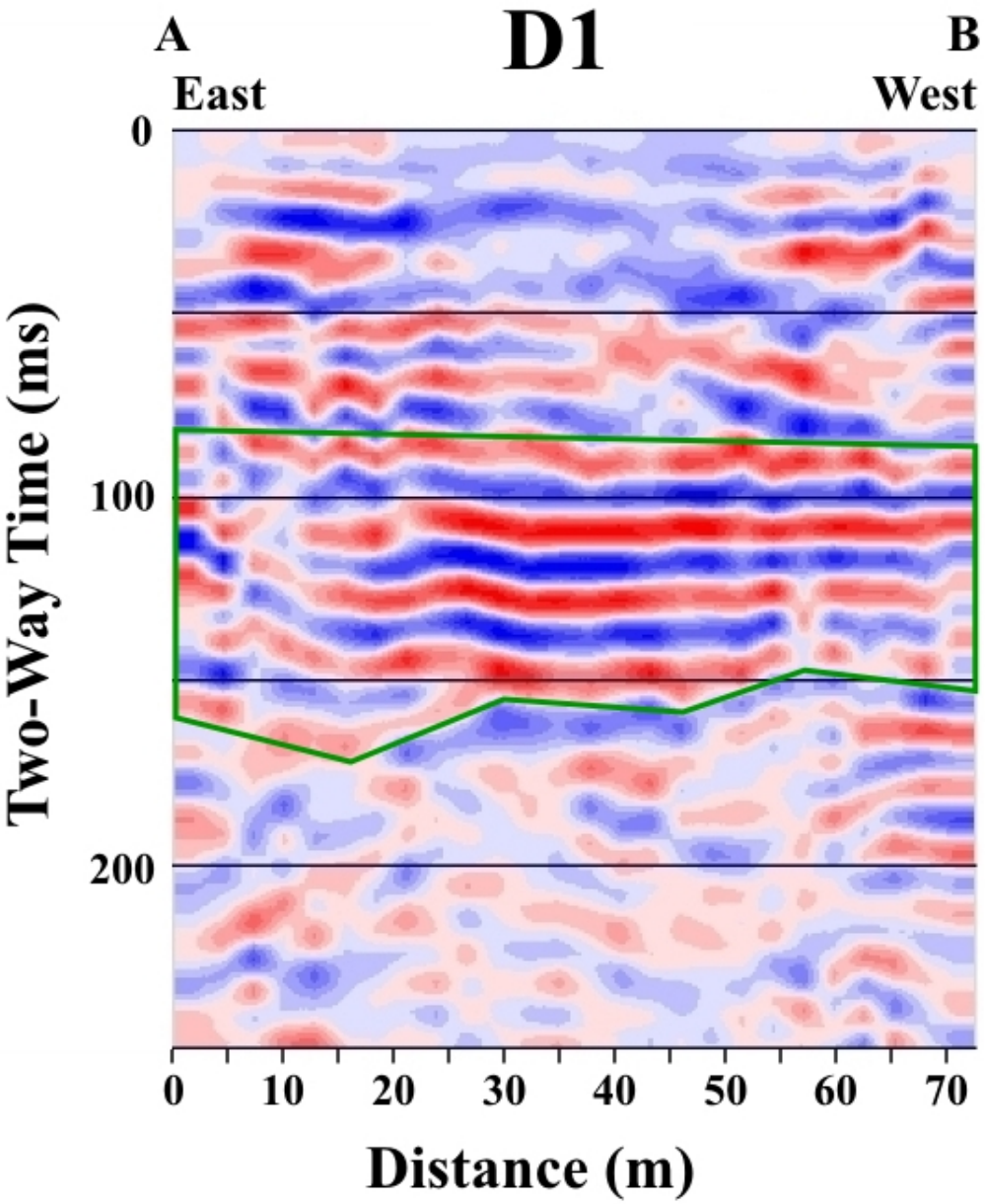

Figure 6.9: Final stacked section for survey D1. The packet of highly coherent reflection from 80-150 ms TWTT is outlined. The top of the bright reflections corresponds to the 23 m layer boundary at the top of the resistivity anomaly.

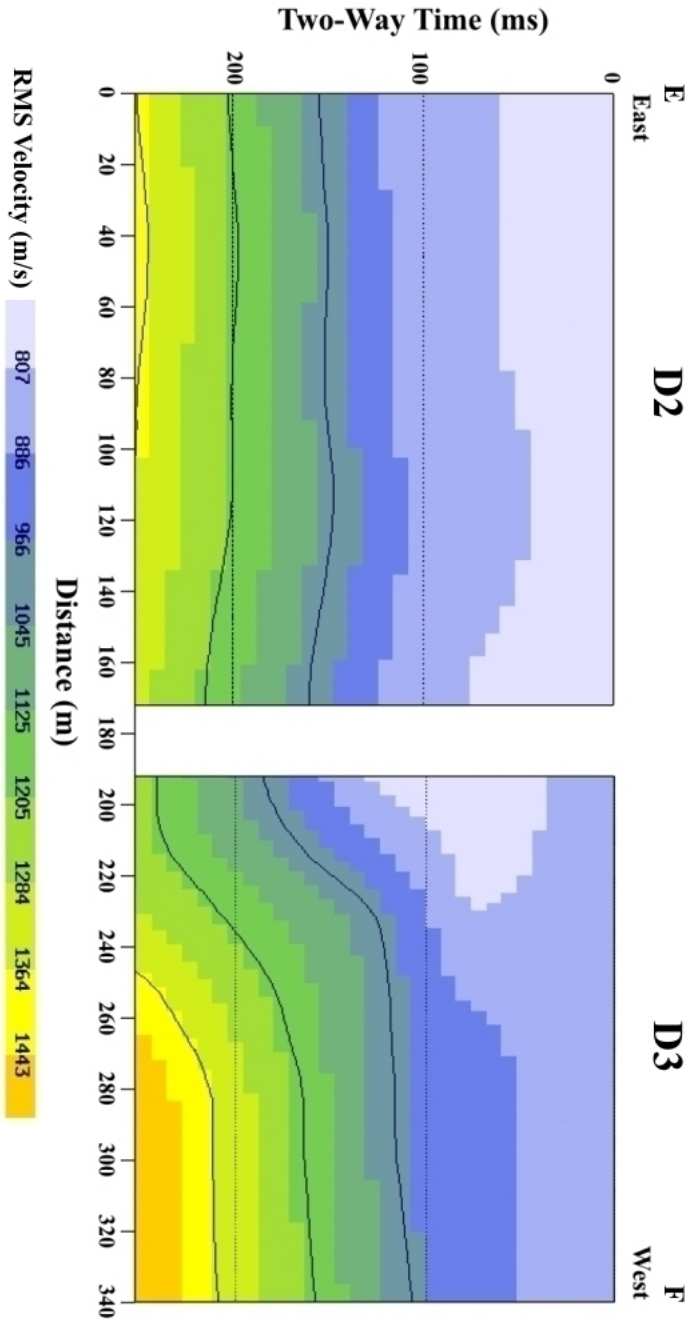

Figure 6.10: Stacking velocity field for surveys D2 and D3. In the middle of survey D3 there is a marked change where the velocity field becomes faster across the edge of the anomaly.

6.3 AVO Analysis

The S-wave velocity of the resistivity anomaly (layer 2) could not be determined directly from the available seismic data. Using Zoeppritz's equations the amplitude of a reflection from a layer boundary can be predicted for a given angle of incidence and V_P and V_S velocities for both layers. Using seismic surveys C1 and D1, V_P and V_S for the top layer and V_P for the second layer were measured. The amplitudes and angles of incidence of reflections from the 24 m layer boundary on seismic surveys C1 and D1 were also measured.

A range of predicted reflection amplitude curves were calculated with Zoeppritz equations using the known V_P and V_S from layer 1 and V_P from layer 2, by varying the V_S for layer 2 (see table 6.2). These predicted curves were then compared with the observed reflection amplitude data to determine the S-wave velocity of the resistivity anomaly (figure 6.11). Any background seismic noise would contribute to inaccurate amplitude measurements so a frequency domain filter BP (15 30 80 120) was applied (see appendix B.5.1). The corner frequencies of this bandpass filter were carefully selected to preserve the frequency content of the reflected arrival. This was the only processing done so as to preserve accurate amplitude information.

Figure 6.11 shows that small variations in V_S for layer 2 lead to large variations in the predicted reflection amplitude. A layer 2 V_S velocity of 650±50 m/s gives a Poisson ratio for the second layer of 0.26±0.06 which is high for gas-charged sand or peat [Ostrander, 1984]. The top layer has a Poisson ratio of 0.39±0.06 showing a contrast between the resistivity anomaly

Depth (m)	**V_P (m/s)**	**V_S (m/s)**	**Poisson's Ratio (σ)**
0 - 24	750±50	310±50	0.39±0.06
24 +	1160±100	650±50	0.26±0.06

Table 6.2: Table detailing observed layer velocities for use in AVO analysis. Layer boundary depth, V_P and V_S for the top layer and V_P for the second layer were constrained using seismic refraction and reflection data (see figures 6.3 and 6.5). V_S for the second layer was calculated using observed reflection amplitudes with Zoeppritz's equations (see figure 6.11). Poisson's Ratios were calculated using V_P and V_S for each layer (see equation 3.2).

and the overlying sediments. According to Ostrander [1984] the presence of gas in pore space causes a strong drop in V_P and a small increase in V_S, resulting in a decrease in Poisson's ratio for the layer.

While the scatter of the data and limited shape of curves available in figure 6.11 don't allow for a good fit, it does indicate an increase in V_S from layer 1 to layer 2. This coupled with an observed V_P of 1160±100 m/s that indicates an absence of groundwater in this layer, leads to the conclusion that groundwater has been replaced by gas and that layer 2 is either a gas-charged sand or peat layer.

6.4 Campion Road survey summary

An airborne resistivity survey located a resistivity high of approximately 1 km^2 that indicated the possible presence of a shallow gas-charged body. Initial seismic refraction surveys C1 and C2 confirmed the presence of a

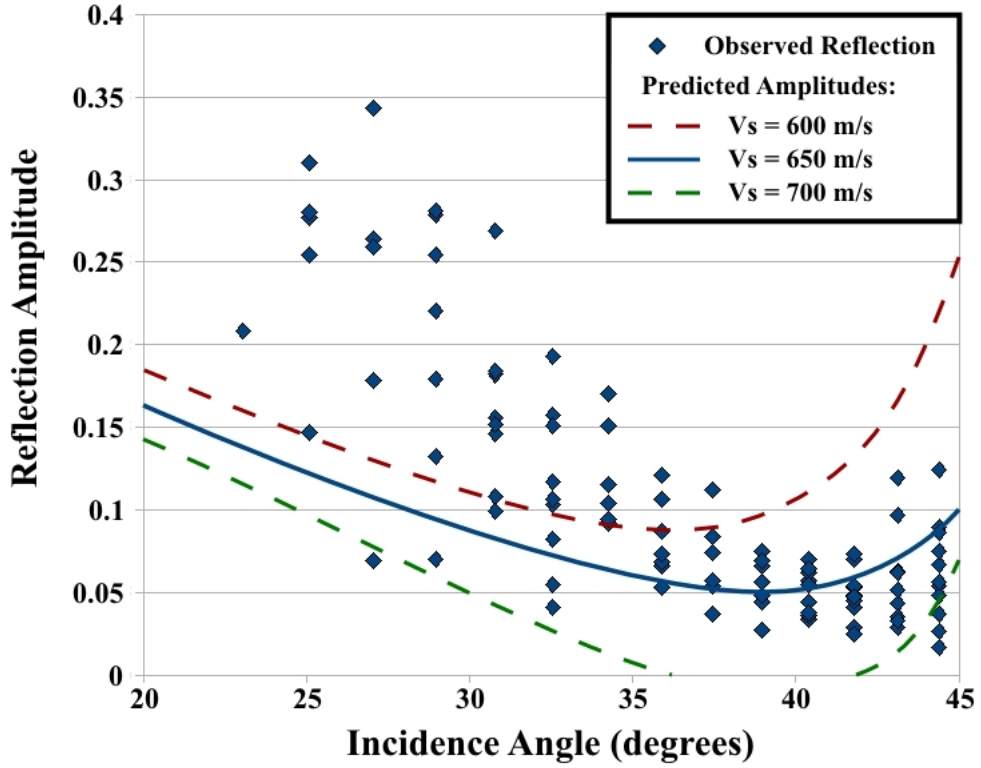

Figure 6.11: Plot showing the predicted and observed amplitudes of reflection 2 for varying angle of incidence in survey D2. The points are calculated from seismic traces showing the amplitude of the reflection from the top of the 24 m layer relative to the source energy. The hard blue line is the predicted P-P reflection amplitude calculated using Zoeppritz's equations to find the S-wave velocity of the second layer. This predicted reflection amplitude refers to the proportion of the incident energy at the layer boundary that is reflected rather than transmitted.

different subsurface structure over the resistivity high compared to nearby areas. Survey C1 found a slow velocity structure with a layer boundary at 23 m depth over the resistivity anomaly, while survey C2 found a much faster velocity structure with a layer boundary at 3.5 m depth to the north of the resistivity anomaly. Well log data from two nearby water wells found no presence of gas and confirmed lithologies consistent with the faster velocity structure found by survey C2.

Seismic reflection surveys D1, D2 and D3 found the resistivity anomaly to be associated with a packet of highly coherent reflections with TWTT of 70-150 ms. The lateral extent of this reflection package was shown to correspond well to the edge of the resistivity anomaly by survey D3. Analysis of the interval velocities using the Dix equation for surveys D1 and D2 showed this 24 m deep body to have a compressional velocity of 1200±100 m/s, which corresponded well to the refraction analysis from survey C1 showing a 23 m deep layer with V_P = 1160±100 m/s. Analysis of stacking velocities for surveys D1 and D2 using the Dix equation yielded a second layer thickness of 45±5 m and a third layer velocity of 3375±500 m/s (figure 6.12).

Zoeppritz amplitude analysis found the second layer to have V_S = 650±50 m/s leading to a lower Poisson ratio of 0.26±0.06 compared to the overlying layer's Poisson ratio of 0.39±0.06. The slow V_P of the second layer indicates an absence of groundwater at depth. The velocities and Poisson ratio observed in the second layer are the expected results for shallow gas-saturated marine sediments [Ostrander, 1984], leading to the conclusion that this highly reflective body is either a sand or peat layer with gas displacing the groundwater in the pore space.

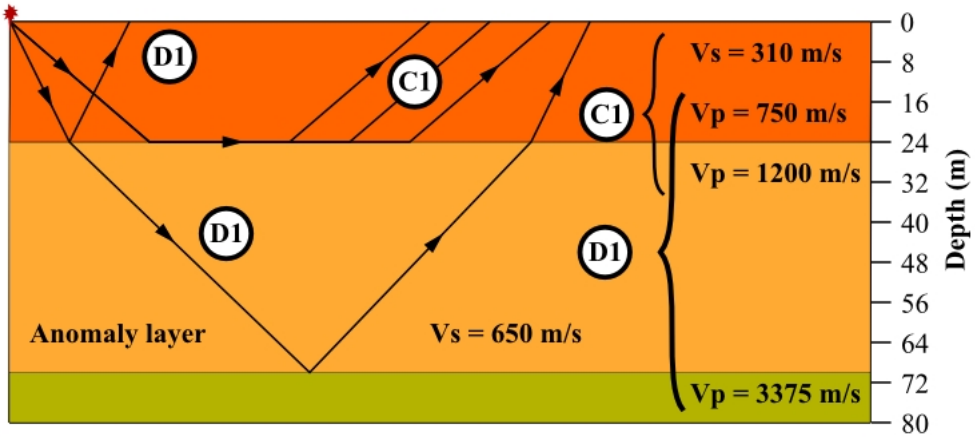

Figure 6.12: Diagram showing layer depths and velocities beneath the centre of the resistivity anomaly. Survey C1 identified V_P for the direct arrival and refraction from the second layer, and V_S for the first layer from a conversion from the top of the second layer in the horizontal components of three-component geophones. Survey D1 identified V_P for the top layer from reflections from the top of the second layer, and the thickness of the second layer and V_P of the second and third layers from the Dix equation and stacking velocities. The V_S of the second layer was found by using Zoeppritz's equations and examining reflection amplitudes from the base of the first layer.

Chapter 7

Summary and conclusions

7.1 Basement depth survey

The seismic and gravity study near Muhunoa East Road investigated the basement depth beneath sediments near the edge of the Tararua range front. Near Levin the range front is controlled by oblique normal faulting with dextral strike-slip motion on the Northern Ohariu Fault. A seismic line shot along Muhunoa East Road by Aharoni [1991] was reprocessed by Ewig [2008] who identified a deep reflection that was interpreted to possibly be a result of side-swipe from basement at a lateral step in the Tararua range front. A gravity survey and two seismic surveys were carried out for this study (figure 4.4).

The gravity profile constructed found the greywacke basement south of Muhunoa East Road to dip northeast with a steepest apparent dip of 12±4° (figure 4.6). Seismic line A1 found the greywacke basement to dip east with an apparent dip of 9±4° (figure 4.8). Reflections from the greywacke base-

ment were apparent on seismic line A2 but were visible over too few traces for an apparent dip to be calculated (figure 4.10). Between seismic refraction line A1 and the gravity profile, the true dip of the greywacke basement was calculated to be 310/NE/12 (figure 4.12). Errors in the two apparent dips used to calculate the basement dip lead to uncertainty in azimuth between 278–008 and dip between 12–19°.

The basement depth found by the new seismic surveys and gravity profile was shallower than the depth found by the previous seismic and gravity surveys along Muhunoa East Road (figures 4.2, 4.3). A different regional gravity model was used for the gravity profile in this study, yielding a basement depth of 230±50 m rather than 350 m beneath Muhunoa East Road. The travel times of reflections where survey A2 and the Muhunoa East Road seismic lines intersect correspond well but their interpretations are different. Based on the velocity structure, observed reflection 2 on survey A2 was interpreted as greywacke basement while reflection 4 was interpreted as an intra-basement layer. On the Muhunoa East Road seismic line the greywacke basement was interpreted to lie at 0.38 s TWTT which puts it slightly deeper than reflection 4 on survey A2. Reflection 2 on survey A2 converts to a greywacke basement depth of 250±50 m depending on layer dip beneath Muhunoa East Road, which corresponds well to the basement depth from the gravity profile in this study.

The surveys conducted for this study found no sub-vertical drops in basement depth that would indicate the presence of a pull-apart basin or provide a favourable surface off which a laterally travelling seismic wave could reflect. This indicates that the deep arrival on the Muhunoa East Road seismic line

is likely to be due to an in-plane low angle intra-basement thrust fault similar to those seen on other seismic lines across the South Wanganui Basin.

7.2 Biogenic gas surveys

Four new gravity points and seismic line B1 were collected near the Wallace Road biogenic gas survey site to constrain basement depth in the area. The gravity survey found the basement to dip west at 14±4° while the seismic survey found a sediment layer above the basement to dip west at 9±5°. Because of the formation of the Tararua Ranges the basement dip must be greater than or equal to the dip of the overlying sediments. This result corresponded well to the basement dip beneath the parallel Muhunoa East Road to the south. The gravity and seismic surveys conducted near the Wallace Road biogenic gas survey found no unusual basement structures that could lead to the accumulation of biogenic gas.

The Wallace Road site had the presence of biogenic gas confirmed when a water well drilled in 1970 flowed gas for 24 hours. The aim of this survey was to use the known shallow structure and the confirmed presence of gas to calibrate the findings for the Campion Road seismic reflection survey and to observe amplitude variation with offset (AVO) in reflections from the gas-charged sand layer.

Three reflections were observed on seismic survey B2: a conversion from the top of the gas-charged sand layer at 19 m depth, an S-S reflection from the base of the gas-charged sand layer at 24 m depth and an S-S reflection from a layer boundary at 31 m depth. The lack of S-wave generation from

the western end of survey B2 and the arrival of the conversion from the top of the gas-charged sand in only the eastern shots led to the conclusion that the conversion was S-P, not P-S. Owing to the swampy nature of the ground and variable near-surface layer thickness the signal-to-noise ratio of the data was poor.

E3D software was used to model a synthetic seismogram with layer depths and initial velocity field taken from the observed lithologies in the well log data. The velocity field was then modified to fit the observed reflection arrival times and Poisson's ratios were calculated for each layer. The gas-charged sand layer was found to have a significantly lower Poisson ratio than the surrounding layers (0.180 compared to 0.485 and 0.474) which was the expected result for shallow gas-saturated marine sediments [Ostrander, 1984].

The predicted amplitudes for the conversion and S-S reflection from the top and base of the gas-charged sand were calculated using Zoeppritz's equations and compared with the observed amplitudes for these arrivals. Due to large scatter in the data it was not possible to determine whether the predicted S-P or P-S conversion amplitude fitted the data better. This meant that the type of conversion observed from the top of the gas-charged sand layer could not be determined from this analysis. The observed S-S reflection amplitudes from the base of the gas-charged sand also showed large scatter with no obvious correlation with the predicted amplitudes. The reflections from the top and base of the gas-charged sand were observable across only a few traces, so their curvature could not be measured and therefore layer dip could not be determined.

A high resistivity anomaly near Campion Road was interpreted as possi-

bly being caused by the presence of biogenic gas displacing local groundwater. Two initial seismic refraction lines C1 and C2 revealed a slower velocity structure over the anomaly with a layer boundary at 23±1 m, compared to a faster shallow velocity structure with a layer boundary at 3.5±0.5 m north of the anomaly. Well log data from two nearby water wells showed a fast shallow velocity structure similar to that observed by the C2 seismic line near the anomaly, and no presence of gas.

Three seismic reflection surveys, D1, D2 and D3, were carried out across the resistivity anomaly (figure 6.2). These surveys found that the resistivity anomaly was associated with a packet of highly coherent reflections with TWTT of 60-150 ms which corresponded to a depth of 24 m. Survey D3 across the boundary of the resistivity anomaly observed a corresponding change in the velocity structure. The interval velocities for survey D1 were calculated using the Dix equation and plotted together with layer depths (figure 6.12). Survey D1 in conjunction with survey C1 was able to show the anomaly to have a thickness of 45±5 m and V_P = 1200±100 m/s.

Amplitudes of the reflection from the top of the second layer were measured and compared with predicted amplitudes calculated using Zoeppritz's equations, to find the second layer V_S = 650±50 m/s. This allowed calculation of Poisson's ratio for the first layer of 0.39±0.06 and second layer of 0.26±0.06. The low Poisson ratio and compressional velocity of 1200±100 m/s (<1500 m/s) indicate an absence of groundwater in the second layer, leading to the conclusion that this highly reflective body is either a sand or peat layer with gas displacing the groundwater.

At Campion Road, as with the Wallace Road site, the velocities and

Poisson ratio observed in the second layer are the predicted results for a shallow gas-saturated layer [Ostrander, 1984]. The packet of highly coherent reflections observed at the Campion Road site shows different characteristics from the reflection observed at Wallace Road, although this could largely be due to the difference in thickness of the two gas bodies. At Campion Road the seismic energy is able to reverberate within the 45±5 m thick layer while the much thinner gas-charged sand at Wallace Road does not allow this. At Wallace Road the biogenic gas must be sourced elsewhere since it is observed within a sand body. At Campion Road, however, if the resistivity anomaly is due to a peat body rather than a gas-charged sand then it is likely to be the source rock of any biogenic gas in the area.

The velocities of the anomaly layer at Campion Road are $V_P = 1200\pm100$ m/s and $V_S = 650\pm50$ m/s compared to the gas-charged sand at Wallace Road with $V_P = 800\pm100$ m/s and $V_S = 500\pm100$ m/s. The layers have similar burial depths so the difference in velocity could be due to a different layer composition with peat at Campion Road compared to the gas-charged sand at Wallace Road. The Poisson ratio observed at Campion Road of 0.26 ± 0.06 is slightly higher than expected for shallow gas-saturated marine sediments [Ostrander, 1984], possibly indicating a peat layer instead of gas-charged sand as observed at Wallace Road.

The high water table at the Wallace Road site was the cause behind many of the observed differences in seismic signature between the Wallace Road and Campion Road sites. Also the topography at Wallace Road limited the seismic line length and possible shot offsets making the shots not directly comparable between the two surveys. These differences between the

sites resulted in limited utility of the Wallace Road results in calibrating the findings for the Campion Road seismic refraction and reflection surveys.

Appendix A

Gravity methods

A gravity survey is a measurement of the variation of the acceleration due to gravity of the earth. The gravity at a location depends on a number of factors: the mass of the earth, the latitude and elevation of the point, the location of the sun and moon relative to the earth and the local factors of density variations in the subsurface and nearby topography.

Gravity is measured in Gal, with 1 Gal = 1 cm/s^2. The average value for gravity at the earth's surface is around 980 Gal and anomalies are expressed in mGal.

The acceleration of gravity of the earth (g) is defined as

$$g = (GM_e/R_e^2), \tag{A.1}$$

where M_e is the mass of the earth, R_e is the radius of the earth and G is the gravitational constant ($G = 6.67\times10^{-11}m^3kg^{-1}s^{-2}$)

Due to rotation the earth is an ellipsoid of rotation, not a sphere, flattened

at the poles and bulging at the equator. To allow for this the International Union of Geodesy and Geophysics proposed an equation IGF30

$$g_\phi = 978049(1 + 0.052884sin^2\phi - 0.0000059sin^2 2\phi), \qquad \text{(A.2)}$$

where ϕ is the geodetic latitude and g_ϕ is the gravity at that latitude (in mGal).

A.1 Gravity data processing

The instrument used for gravity surveys in this study is a Lacoste & Romberg model G gravity meter. This instrument measures relative gravity and must be tied to a point where the absolute gravity is known. In New Zealand there are 437 absolute gravity points, and for this study the Pekapeka point was used [Robertson and Reilly, 1960]. Each Lacoste & Romberg gravity meter is calibrated to a different scale so readings must be converted to mGal using a conversion table. At each location a Trimble GPS system was also used to accurately determine easting, northing and elevation.

A.1.1 Drift correction

Gravity readings will slowly drift throughout the day due largely to two factors: tidal effects and instrument creep. The positions of the sun and moon cause slight changes in the shape of the earth called solid earth tides. These tides mean that the distance from any point on the surface to the centre of the earth fluctuates causing gravity at that point to change slightly.

Instrument creep is due to springs expanding and contracting within the gravity meter itself, an effect that is minimised by keeping the instrument at a constant temperature. Both of these factors are small enough that they can be corrected for by drift correction calculations.

On each day of gravity surveying the first and last point measured was the absolute gravity point at Pekapeka. The other base station used was a point on Muhunoa East Road from the Aharoni [1991] survey. This base station was reoccupied 3 times during the day (every 3-4 hours). By observing how gravity at these two base stations varied throughout the day a drift curve could be calculated and applied to the data for that day.

A.1.2 Observed gravity

Once a reading has been taken, converted to mGal and drift corrected, it must be converted to an absolute gravity measurement (g_{obs}). This was done using the Pekapeka point where the value of absolute gravity is known. Absolute gravity at Pekapeka is 980200.8 mGal [Robertson and Reilly, 1960]. This value can be used to convert all drift corrected mGal gravity measurements to absolute gravity values.

A.1.3 Predicted gravity

The predicted gravity value at any location is a combination of four factors: Gravity at latitude, free air correction, Bouguer slab and terrain correction.

Gravity at latitude

The earth is an ellipsoid of rotation, not a sphere, hence gravity varies with latitude as the distance from the centre of the earth changes. (Gravity is greatest at the poles and least at the equator.) Using the IGF30 equation (equation A.2) gravity (g_ϕ) at sea level at any latitude (ϕ) can be predicted.

Free air

Gravity reduces by 0.3086 mGal for each metre of elevation above mean sea level because the distance to the centre of the earth increases.

$$\delta g_F = -0.3086 * h \tag{A.3}$$

where δg_{F} is the increase in gravity (in mGal) (a reduction so negative) and h is the elevation above mean sea level (in metres).

Bouguer slab

The free air correction accounts for reduction in gravity due to elevation above mean sea level. The Bouguer slab correction accounts for the increase in gravity due to the presence of additional rock between sea level and the elevation of the measurement by modelling the gravity from an infinitely extending slab of uniform thickness h and density ρ.

$$\delta g_B = 2\pi\rho G h = 0.0419 * \rho * h \tag{A.4}$$

where δg_{B} is the increase in gravity, ρ is rock density, G is the gravitational constant ($G = 6.67\times10^{-11}m^3kg^{-1}s^{-2}$) and h is the elevation above mean sea level (in metres). The Bouguer slab is assumed to be basement rock, in this case greywacke with density $\rho = 2.67$ g/cm^3.

Terrain corrections

The terrain correction δg_{TC} is used to account for variations in topography from a flat plane around the gravity station. Any hills or valleys will reduce gravity measurements either through mass above or lack of mass below the gravity meter. In this study the Hammer method [Hammer, 1939] of concentric circles around the station (zones A-M) was used. Zone M is the largest and extends out to 22 km from the station in all directions. Each zone is divided into a number of equal sized compartments and the average elevation difference from each compartment to the station is estimated. Zones A-D (0 - 170 m) are estimated from the station, while zones E-M (170 m 22 km) are calculated by the software tool demtools using the Victoria University of Wellington owned Digital Elevation Model (DEM, 25 m resolution) of the mainland of New Zealand. The inner terrain correction is found by reading all the A-D zone compartments into a table and calculating the total mGal reduction in gravity. The outer terrain correction (in mGal) can simply be added to the inner terrain correction to find the total terrain correction for each point.

A.1.4 Bouguer anomaly

The equation for the predicted gravity value is

$$g_{pred} = g_{\phi} + \delta g_F + \delta g_B - \delta g_{TC}. \tag{A.5}$$

The end product of this process is the Bouguer anomaly (Δg_{Boug}) where

$$\Delta g_{Boug} = g_{obs} - g_{pred}. \tag{A.6}$$

The Bouguer anomaly represents the difference between the observed and predicted gravity values at a point. The Bouguer anomaly is a combination of a short and long wavelength anomaly. The short wavelength anomaly results from shallow, localised geological features and overprints the long wavelength anomaly (regional gravity field). To analyse the short wavelength anomaly it must first be removed from the long wavelength anomaly. In this study information about the regional field gravity anomaly for the Horowhenua region was taken from Ewig [2008].

A.2 Residual gravity

The short wavelength gravity anomaly arises from the rock density beneath the station. The predicted gravity model assumes a solid greywacke slab density of $\rho = 2.67$ g/cm^3 from the station down to mean sea level. If there is a layer of less dense sediments overlying the greywacke basement this will reduce the measured gravity at the station. Given a known sediment density

it is then possible to model the sediment thickness based on the size of the Bouguer anomaly. Ewig [2008] calculated a regional gravity gradient and subtracted this from gravity readings on the profile along Muhunoa East Road to create a residual gravity model (see figure 4.3).

A.3 Uncertainties in gravity measurements

Uncertainties in gravity measurements come from four sources of error: uncertainty in the instrument reading, uncertainty due to drift and drift correction, uncertainty in the elevation of the station and errors in the terrain correction.

To minimise error at each location gravity measurements were repeated until three similar reading were obtained within 0.05 gravity meter units of one another (approximately 0.05 mGal). The aim of this was to eliminate outliers in the measurements. The gravity meter was moved and re-levelled for each reading. The mean of the three readings for each station was used.

The interpretation of the drift curve used to remove instrument drift introduces error. For each day of gravity surveying only five measurements could be used to create the drift curve: three from the Muhunoa East Road base station and two from Pekapeka base station. Linear drift between measurements was assumed, with the repeat interval between base station readings as large as three hours. This drift correction is estimated to have an error of $\pm$ 0.1 mGal.

The elevation of each gravity station was determined using a differential Global Positioning System (GPS) technique. For each survey baselines were

created to a known point during processing to compensate for daily drift. This method has an uncertainty in height of around 20 cm. Elevation is used in free air and Bouguer slab calculations, so the final uncertainty due to elevation in the Bouguer anomaly calculation is ± 0.08 mGal.

Inner terrain corrections performed by student groups showed an error in estimating heights of 10-20%. Assuming a maximum error of 20% and no inner terrain corrections higher than 0.8 mGal yields an error of ± 0.16 mGal. The outer terrain corrections calculated using the Digital Elevation Model of the mainland of New Zealand have a negligible error.

These error values give a total uncertainty of ± 0.4 mGal for the calculated Bouguer anomaly points. Bouguer gravity values used from the IGNS database are assumed to have a maximum uncertainty of ± 1.5 mGal [Ewig, 2008].

A.4 Gravity modelling software

(Henderson, M 2010.) Unpublished javascript software was used to create 2-dimensional gravity profiles near Muhunoa East Road and Wallace Road to model basement depth. This gravity modelling software takes an input file containing elevation and distance along profile for residual gravity anomaly readings. A model is created using blocks with different densities, and gravity anomaly created by the model can be compared to the observed anomaly. The modelled gravity can be adjusted either by varying the volume and placement of the blocks or changing their density. Once the modelled gravity anomaly curve fits the observed data well then one possible solution has been

found. It is important to note that infinitely many solutions for any curve exist and that it is important to consult other known data for the region to determine the model's validity.

A.5 Gravity data

Station ID	**Easting (m)**	**Northing (m)**	**Elevation (m)**	**Observed gravity (mGal)**	**Predicted gravity (mGal)**	**Bouguer anomaly (mGal)**
M01 (Base)	2704201.87	6055928.97	101.6	980165.35	980219.45	-54.1
M02	2704354.50	6055737.13	129.49	980161.25	980213.40	-52.16
M03	2704533.96	6055706.33	154.11	980156.72	980208.56	-51.83
M04	2701230.99	6056308.44	40.77	980175.73	980231.08	-55.35
M05	2700747.60	6055483.30	48.62	980175.78	980230.56	-54.78
M06	2703348.01	6055001.02	112.69	980164.07	980217.76	-53.70
M07	2703497.57	6055329.35	94.87	980166.21	980221.13	-54.92
M08	2703701.31	6055638.91	92.97	980165.91	980221.41	-55.50
M09	2702247.75	6056754.80	53.33	980172.27	980229.02	-56.75
M10	2702216.83	6056565.53	52.46	980173.15	980229.25	-56.10
M11	2702014.32	6056492.20	49.28	980174.47	980229.99	-55.52
M12	2701779.09	6056510.45	47.12	980175.49	980230.26	-54.76
M13	2699875.02	6056580.53	30.46	980170.86	980233.98	-63.12
M14	2699991.68	6055581.06	39.30	980175.10	980232.79	-57.69
M15	2702043.02	6055445.33	74.66	980171.03	980225.63	-54.60
M16	2704203.14	6055924.27	101.6	980165.25	980219.60	-54.35
M17	2705194.70	6055712.42	156.12	980157.63	980207.66	-50.03
M18	2699750.98	6057358.23	29.12	980167.65	980233.78	-66.13
W01	2707849.70	6064769.73	12.25	980160.80	980230.83	-70.02
W02	2708344.48	6064355.69	20.08	980164.19	980229.19	-65.00
W03	2708702.78	6064020.37	32.53	980164.81	980226.80	-61.99
W04	2708933.25	6063621.00	44.90	980164.30	980224.45	-60.14
W05	2709344.92	6064058.95	65.36	980161.17	980219.79	-58.62

Table A.1: Muhunoa East Road gravity data from M01-M18. Wallace Road gravity data from W01-W05.

Appendix B

Seismic methods

B.1 Seismic data acquisition

B.1.1 Seismic source

Two different seismic sources were used for the surveys in this study. For A1, A2, B1, C1 and C2 a hydraulic thumper was used. An EG&G hydraulic thumper is a drop weight mounted on a trailer with additional acceleration due to an engine-generated vacuum beneath the weight. The hydraulic thumper is a repeatable source with a main frequency around 70 Hz and is capable of a maximum penetration depth of 1 second TWTT. Because of its size it was unfeasible to use the hydraulic thumper for surveys B2 and B3 since the site was at the bottom of a steep valley with limited vehicle access. The initial intention was to use the hydraulic thumper for D1, D2 and D3, but unfortunately the mechanism used to raise and lower the hydraulic thumper to enable movement broke during survey D2, so an alternative seis-

mic source needed to be used. It was decided to complete survey D2 and and shoot surveys D3 and D1 using sledgehammer shots on an iron rail as a seismic source.

The maximum penetration of sledgehammer shots is worse than the hydraulic thumper, so it was decided to use stacks of 8 sledgehammer shots at each location. The shots were recorded on top of each other using the R48. The aim of this stacking was to improve the signal to background noise ratio present in the shots. A problem with this method was that the triggering mechanism used to start the recording in the R48 was slightly inaccurate, meaning that each sledgehammer shot was triggered at a slightly different time so did not stack precisely with the other shots at the same location. This led to some destructive interference in the shot records, meaning that the signal to background noise ratio was not necessarily improved by stacking shots. Unfortunately this was not discovered until the shots were downloaded after the surveys were completed, at which stage there was no way to rectify the problem.

B.1.2 Receivers and data recorder

The vertical geophones used for all surveys had a frequency response of 10 Hz. These geophones have a spike on the bottom and are driven into the ground, requiring soil or soft ground to be deployed. In surveys B2, B3, C1 and C2 three-component geophones were also used. Three-component geophones measure motion in 3 component directions simultaneously; vertically, along the seismic line and perpendicular to the seismic line. Measuring motion

in the horizontal direction allows for easier detection of S-wave arrivals. At small offsets, reflections from a deeper layer would arrive sub-vertically at the surface, meaning that any compressional P-waves would have motion mostly in the vertical direction while shear S-waves would have motion mostly in the horizontal directions. By shooting the same surveys again using three-component geophones, the horizontal components of detected arrivals can be measured, potentially leading to the identification of other phases and a better understanding of the layers and velocity structure present.

The geophones were plugged into takeout cables, each of which connects 24 geophones. The cables were in turn connected to a Geometrics^{TM} Strataview^{TM} R48. Three-component geophones require three takeouts since they record three records, so 8 three-component geophones can be attached to a takeout cable and the R48 can record all records from 16 three-component geophones simultaneously. This is the reason why when re-shooting surveys using three-component geophones they were placed at every third geophone location. The R48 is capable of recording 48 channels of seismic data at a time. For surveys D2 and D3, which were more than 48 geophones long, a rollbox was used to select which geophones were to be recorded from for each shot. The rollbox is capable of having 4 takeout cables (96 geophones) attached at a time.

All seismic processing was done using Globe Claritas^{TM} software. After field work all the data files from the R48 were converted to segy format and loaded into Claritas^{TM}. Before any other processing was done a geometry file was created for each survey and applied in the first job.

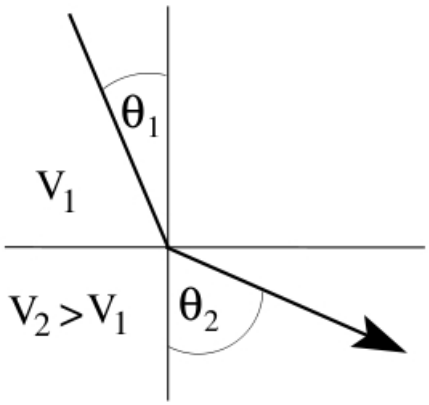

Figure B.1: Diagram showing the refraction of a seismic ray at a layer boundary.

B.2 Seismic refraction methods

B.2.1 Theory

When a seismic ray encounters an impedance contrast (rapid change in medium velocity or density) it splits into different paths, with some of the energy reflected back into the same layer and the rest of the energy refracted into the next layer. The refraction is described by Snell's law

$$\frac{sin\theta_1}{sin\theta_2} = \frac{V_1}{V_2} \tag{B.1}$$

where θ_1 is the angle of incidence, θ_2 is the angle of refraction, and V_1 and V_2 are the velocities of the two layers (figure B.1). If velocity is increasing with depth (V_2 is greater than V_1) then the ray will be refracted away from the normal to the interface.

If $\theta_2 = 90^o$ then the refracted ray travels along the V_2 side of the layer boundary. This is called critical refraction. For critical refraction to occur

the angle of incidence (θ_1) must be the critical angle (θ_c). From equation B.1 the critical angle depends on the velocities of the two layers

$$\theta_c = sin^{-1}\left(\frac{V_1}{V_2}\right). \tag{B.2}$$

A critically refracted ray will propagate along the layer boundary at velocity V_2 and emit a seismic wave under the critical angle at every point along its travel path.

B.2.2 Seismic refraction analysis

These arrivals appear as straight lines on a time vs. receiver distance plot (figure B.2).

$$t_1 = \frac{2z_1\sqrt{V_2^2 - V_1^2}}{V_1 V_2} \tag{B.3}$$

where t_1 is intercept time (seconds), z_1 is thickness of layer 1 (metres) and V_1 and V_2 are the layer velocities (metres/second). This equation can be rearranged to solve for the thickness of the top layer (z_1). The crossover distance ($\mathrm{x_{cross}}$) is the offset from the shot point at which the direct arrival and the critically refracted arrival have the same travel time.

B.2.3 Seismic refraction from a dipping layer method

When the refracting layer is dipping the direction of observation is important. The refracted ray that travels in the downdip direction will arrive earlier but have a slower apparent velocity than the true velocity for the layer, while the ray that travels updip will arrive later but have a faster apparent velocity

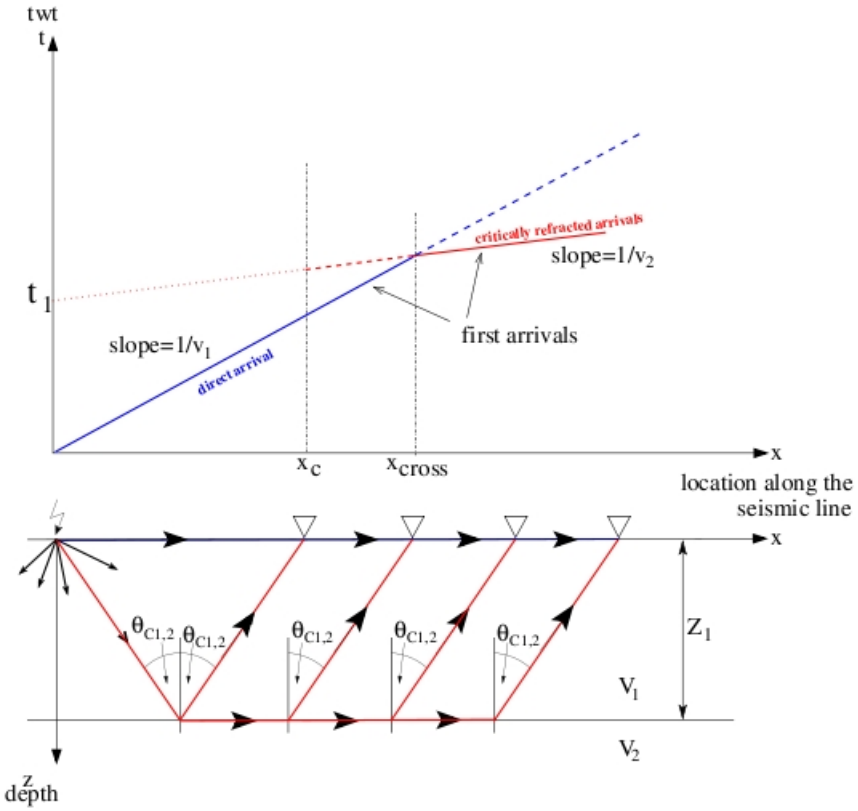

Figure B.2: Plot showing distance vs. travel time (top) for a seismic ray travelling directly along the top layer (blue) and refracting along a faster second layer (red). A cross-section in the earth (bottom) shows the ray paths followed by the two arrivals.

(figure B.3). If a shot is fired from each end of the same geophone array so that both updip and downdip velocities are found, then the dip of the refracting layer can be calculated using the equation

$$\gamma_1 = \frac{1}{2}\left[sin^{-1}\left(\frac{V_1}{V_{2d}}\right) - sin^{-1}\left(\frac{V_1}{V_{2u}}\right)\right] \tag{B.4}$$

where γ is the dip of the layer and $V_{2\mathrm{d}}$ and $V_{2\mathrm{u}}$ are the apparent downdip and updip velocities.

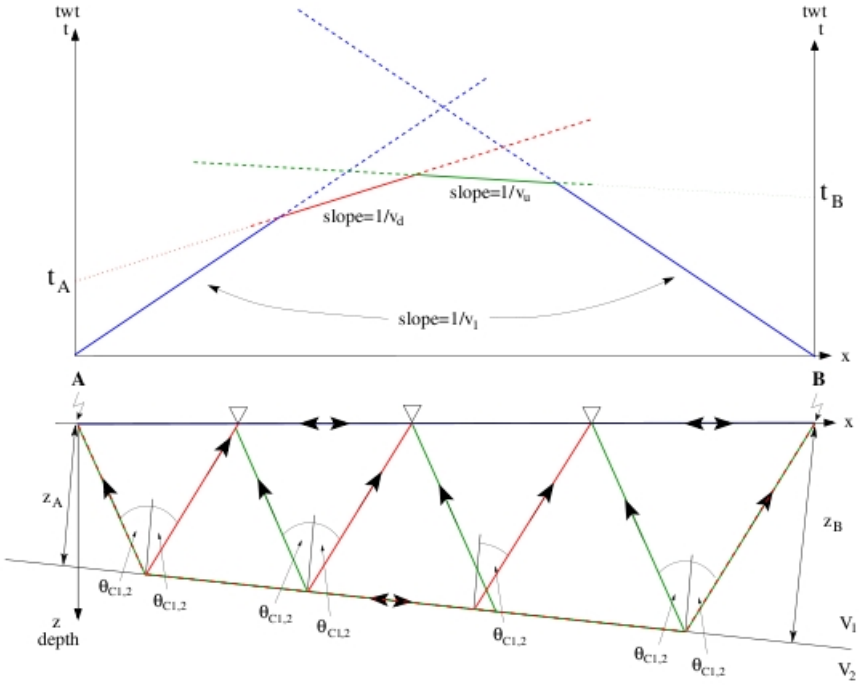

Figure B.3: Plot showing distance vs. travel time for a dipping layer case. The ray refracting from the second layer travelling in the down-dip direction (red) has a slower apparent velocity and earlier initial arrival than the up-dip refraction (green).

The thickness of the top layer under the two shot points (A and B) can be calculated

$$z_A = \frac{1}{2} t_A V_1 cos^{-1}(\theta_{C1,2}) \tag{B.5}$$

$$z_B = \frac{1}{2} t_B V_1 cos^{-1}(\theta_{C1,2}) \tag{B.6}$$

B.2.4 Plus-minus method

The plus-minus method is used to find the depth of a shallow layer using the arrival times of waves that refract along that layer in both directions. To

apply this method to a seismic line a single shot was selected at each end of the geophone array. For both shots the arrival time of the direct ray and first refraction was recorded at each geophone. The travel time for the refracted ray over the whole length of the line is the same in both directions because it follows the same path. The travel times for refracted rays travelling along sections of the line depend on the depth and dip of the second layer. By measuring the travel times for both shots at each geophone the velocities of both layers and the depth to the layer boundary along the line can be calculated. This method is capable of mapping undulations in the layer boundary. The delay time at any point (x) along the line is the difference between the travel time from both shot locations to that point (x), and the travel time from one shot point to the other (the whole length of the line). The delay time is given by

$$t_{delay} = 0.5(t_{ud} + t_{dd} - t_{tot}) \tag{B.7}$$

where t_{delay} is the delay time at the point (x) along the line, t_{ud} and t_{dd} are the up-dip and down-dip travel times to point (x) and t_{tot} is the travel time for the whole line. From this the depth (z) to the layer boundary at any point (x) along the line can be calculated:

$$z(x) = \frac{t_{delay}(x)V_1V_2}{\sqrt{V_2^2 - V_1^2}}. \tag{B.8}$$

B.3 Seismic refraction data processing

Below is the list of processes used to create seismic refraction images in Globe Claritas^{TM} software.

Trace removal

The TREDIT process was used to remove dead traces from each shot record. Channel 1 in each shot is always dead due to a fault in the R48. Other traces with too much noise were removed where appropriate. Often this is due to poor coupling between the geophone and the ground.

Frontmute

The SMUTE process was used to remove everything before the first break. This is generally the direct arrival or the seismic refraction from the second layer. Any record before this will simply be noise and can be removed with no loss of data. This mute was picked by eye on each shot and then applied using the SMUTE process.

Bulkshift static correction

The STATIC process allows traces to be shifted vertically. This allows for the zero time in each shot record to be altered. With a bulkshift STATIC all traces in a single shot are shifted the same amount of time. This was used in shots which were triggered manually so as to correctly zero the shot time.

Near-surface static correction

The STATIC process was also used to correct for near-surface velocity variations. The delay in arrival time from a slow near-surface layer depends on the thickness of that layer. If the thickness varies from one geophone to the next then each trace will be slowed by different amounts of time and the first arrival will not be on a straight line. The *2D Refstat* package in Claritas uses the picks of the first arrivals from all shots on the line to iteratively create a velocity model. This velocity model is then applied using the STATIC process to remove the near-surface layer variations by extending the source and receivers onto a flat horizontal datum beneath the weathered layer.

Automatic gain control (AGC)

The AGC process is a scaling process used to balance sets of live traces. A window length is set and each sample of the trace is multiplied by a scaling factor calculated so that the average amplitude over the given window length is constant down the trace.

Balance

The BALANCE process scales each trace by a scalar so that the average amplitude of each output trace is constant across the shot record. The BALANCE process is a purely spatial trace balance as opposed to time balancing like AGC which alters the frequency content of a trace and destroys all relative amplitude information.

Spherical divergence

The SPHDIV process scales each sample of each channel by a scalar that depends on the time elapsed since T_0 and the offset of that channel from the shot point. Seismic energy attenuates a certain amount for each wavelength travelled, meaning the frequency of the energy and the velocity of the medium are important for applying a spherical divergence correction.

Frequency-wavenumber (f-k) filtering

FK filter is a frequency-wavenumber filter which allows for the removal of certain types of unwanted energy, especially ground roll. Data can be converted from the time-offset tx-domain to the frequency-wavenumber fk-domain using a 2-D Fourier transform. Different velocities of arrival appear in different segments of the fk-domain allowing for specific types of arrivals to be removed. In Claritas^{TM} fk-domain mutes were picked using the FK spectrum in XVIEW and were applied in jobs using the FKMUTE process.

Butterworth bandpass filter

The Butterworth bandpass filter is used to select which energy in the frequency domain in the seismic record is preserved and which is removed. Four corner frequencies define the filter boundaries and each frequency is assigned an amplitude from 0 to 1 which corresponds to the amount of energy of that frequency that is preserved. The amplitudes of energy allowed at frequencies between the defined corner frequencies are interpolated by the filter. It can be used as a high-pass or low-pass filter rather than as a bandpass filter by

defining only the two high or two low frequencies instead of all four.

Frequency domain filter

The FDFILT process is a frequency domain filter similar to the BUTTERFILT process. Instead of being defined manually, the corner frequency amplitudes are set to 0 1 1 0. With the FDFILT process a time window is defined over which it is applied to each trace. This allows for FDFILT to be targeted at noisy sections of the seismic record and to be used to remove specific arrivals.

B.4 Seismic reflection methods

B.4.1 Theory

When a seismic ray is incident on an impedance contrast it splits into different paths with some of the energy reflected and some transmitted at angles described by Snell's law (see equation B.1). The reflected energy propagates back to the surface and is recorded by an array of geophones. The travel time of the recorded waves is governed by the distance travelled to the reflector and the seismic velocity of the rock passed through. By measuring the travel time of the reflection the depth, dip and curvature of the reflector as well as the velocities of subsurface media can be calculated.

B.4.2 Seismic reflection data acquisition

The geometry of the array and seismic source used to collect seismic data can have a strong influence on the quality of the final seismic image. The distance between the seismic source and the first receiver is important for minimising the amount of noise recorded. Ground roll is a Rayleigh wave with low frequency and high amplitude which travels in the near surface slightly slower than the S-wave velocity of the layer. If the source to first receiver offset is too small then the target reflection will arrive at the same time as the ground roll and be masked by the much larger amplitudes. If the source to first receiver distance is too large then only the wide-angle part of the target reflection will be recorded. Another important aspect of the survey geometry is the geophone spacing. The closer the geophone spacing the greater the resolution of the survey, but the smaller the maximum recorded offset because of the limit of 48 geophones recording each shot.

A rule of thumb states that the maximum offset between the seismic source and first geophone should not exceed the depth of the target reflector, and the geophone spacing should be between 1/10 and 1/20 of the depth of the shallowest reflector desired [Knapp and Steeples, 1986]. In this survey the desired reflector is known to be at a depth of 24 m, so a shot offset of 10 m and a geophone spacing of 2 m were chosen. This shot offset was chosen to be large enough to allow the first reflection from the target reflector to arrive ahead of the ground roll.

B.4.3 Seismic reflection analysis

Reflections from a flat layer will appear as curved, hyperbolic arrivals in a time vs. receiver distance plot. The equation for the hyperbolic travel time curve can be given as

$$T^2 = x^2/v_0^2 + 4h_0^2/v_0^2 = x^2/v_0^2 + t_0^2 \tag{B.9}$$

where T is TWTT (seconds), x is the horizontal offset from shot point (metres), h is the depth of the layer (metres), v_0 is the average velocity above the layer (metres per second) and t_0 is the time at which the curve intercepts the T axis (seconds). This equation can be rearranged to solve for the depth h from the surface to the reflection. For a reflection from a flat layer the peak of the reflection curve will be directly beneath the shot point.

V_{RMS} stands for the root mean square velocity. This can be calculated by measuring the curvature of the reflection and describes the mean velocity of all the layers between the surface and the reflector.

B.4.4 The Dix equation

The Dix equation allows the calculation of interval (individual layer) velocities given the TWTT and V_{RMS} of at least two reflections. If a reflection from the top of the n^{th} layer has vertical two-way travel time t_{n-1} and root mean square velocity V_{n-1}, and a reflection from the top of the $(n+1)^{th}$ layer has vertical two-way travel time t_n and root mean square velocity V_n, then the velocity for the n^{th} layer is

$$v_n^2 = \frac{V_n^2 t_n - V_{n-1}^2 t_{n-1}}{t_n - t_{n-1}}. \tag{B.10}$$

B.4.5 Seismic reflection from a dipping layer

If a seismic reflection comes from a dipping layer rather than a horizontal layer then the peak of the curve will not be directly beneath the shot point (figure B.4). By measuring how far this peak is offset from the shotpoint together with the depth and curvature of the reflection it is possible to calculate the depth and dip of the reflector. The depth and dip of a reflector can be calculated using

$$T^2 = [x^2 + 4h^2 + 4hx.sin\theta]/v_0^2 \tag{B.11}$$

where T is TWTT (seconds), x is the horizontal offset from the shot point (metres), h is the depth of the layer beneath $x = 0$ (perpendicular to the dipping layer, in metres), θ is the dip of the layer (degrees) and v_0 is the average velocity above the layer (metres per second).

B.5 Seismic reflection data processing

Below is the list of processes used to create seismic reflection images in Globe Claritas^{TM} software.

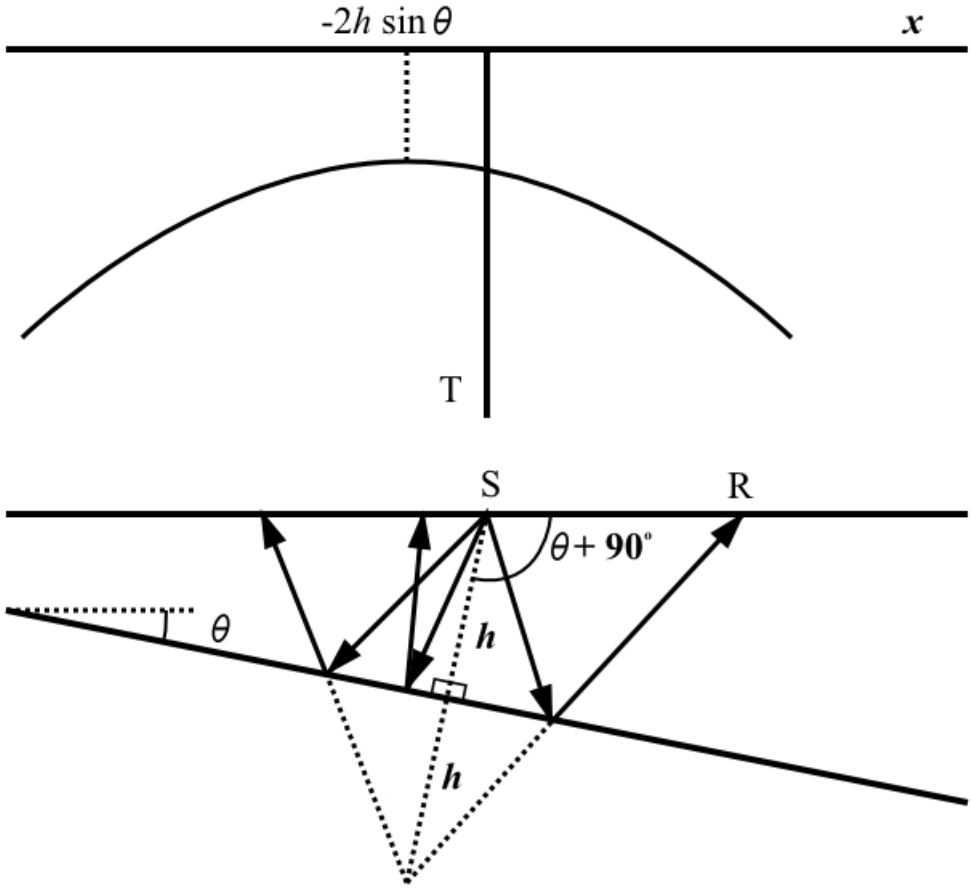

Figure B.4: Plot showing distance vs. travel time (top) for a reflection from a dipping layer. A cross-section in the earth (bottom) shows the ray paths followed.

B.5.1 Prestack processing

Quality control

- Dead/noisy channels: These can be caused by a local noise source, poor coupling between the geophone and the ground, or a badly connected geophone. These traces were identified and removed using the TREDIT process.

- First break removal: The first break of every channel is usually the direct arrival or a seismic refraction. These generally have high amplitudes and would interfere with later incoming seismic reflections. A frontmute was picked individually for each shot and applied using the SMUTE process. The limit of the mute was often chosen to compromise between retaining seismic reflections and removing seismic refractions, as at larger offsets the events began to overlap.

Static correction

Irregular topography and a low velocity near-surface weathered layer of variable thickness adds variation to travel times between different receivers. The aim of the static correction was to use the STATIC process to remove the effect of the weathered layer by applying a model created using the *2D Refstat* package.

Filtering

- Frequency-wavenumber (f-k) filtering. Ground roll is of a slower velocity than the seismic reflections in the shot record. An F-K filter was used to remove the unwanted ground roll energy with the FKMUTE process.

- Frequency filtering. Sledgehammer shots generate energy within a certain frequency band. By filtering the signal in the frequency domain, any noise that doesn't fall within the same band will be removed with no loss of signal. For this the FDFILT process was used.

Compensation for attenuation

- Spherical Divergence. Seismic energy attenuates owing to distance travelled and layer boundaries encountered. The spherical divergence process SPHDIV multiplies each sample of each channel by a scalar that depends on the time elapsed since T_0 and the offset of that channel from the shot point.

- Automatic gain control (AGC). The AGC process multiplies each sample of each trace by a scalar to give an unchanging average amplitude within a moving time window. The AGC process is easy to apply and can be used to assist the SPHDIV process as well as for quick assessment of other processing in XVIEW.

- Balance. The BALANCE process scales traces so that the average amplitude of each trace in a shot gather is the same. The BALANCE process is easy to apply and can be used to assist the SPHDIV process.

B.5.2 Sorting and brutal stack

Before seismic reflection data can be stacked, traces must be sorted into common midpoint (CMP) order. Assuming the reflecting layer is not dipping, the point each seismic ray reflects from will be half way between its source and its receiver. The even spacing of geophones causes a number of rays equal to the seismic fold to reflect from the same point on the reflector. Each of these points is called a common midpoint (CMP).

Since the rays reflecting from the same point on the reflector have different

path lengths due to different source locations and angles of incidence, their travel times will also be different. The travel time for a reflection from a flat layer depends on the distance between the source and receiver (x), the two-way zero offset travel time (t_0) and average velocity of all layers above the reflector (V).

$$\delta t \approx \frac{x^2}{2V^2 t_0} \tag{B.12}$$

The difference between measured two-way travel time and zero offset travel time at any CMP is called normal moveout (δt) (NMO). By assuming a velocity field, travel times for wider offset rays can be reduced using a NMO correction so they can be summed at each CMP. In a brutal stack, a single stacking velocity is applied to the whole line, allowing the data to be stacked for viewing; however, the arrivals on each summed trace will not add together properly as the correct NMO velocity was not used. The arrivals in an image produced from a brutal stack will not be clear.

B.5.3 Picking a velocity field

In the case of a single layer above the reflector, the stacking velocity will be the velocity of that layer. In the case of multiple layers with different velocities above the reflector the stacking velocity will be the root-mean-square (RMS) velocity of the layer sequence. Three methods of velocity field analysis were used to determine the final stacking velocity field.

- Constant Velocity Stack (CVS). The user selects a part of the stacked section and a range of stacking velocities. Constant velocity stacks

are created for a range of stacking velocities which can be compared manually to determine the velocity that gives the clearest event at different TWTT's.

- Constant Velocity Gather (CVG). The user selects a CMP or a range of CMP's and a range of stacking velocities. For each CMP all the traces to be stacked are displayed and scaled depending on the stacking velocity currently selected. The aim of a CVG is to determine which velocity gives the flattest event across all traces within a CMP gather.

- Semblance analysis. The semblance display shows arrival amplitudes using a colour palette on a stacking velocity vs. travel time plot for each CMP gather. Semblance analysis provides an easy visual method of quickly picking stacking velocities for each CMP.

For all three seismic reflection lines an initial velocity field was picked using semblance analysis. This was then corrected using CVG and CVS in turns.

B.6 E3D software

2D/3D Elastic Finite-Difference Wave Propagation Code (E3D) software was used to create a synthetic seismogram for the B2 seismic line. E3D takes an input file containing model parameters and outputs a synthetic seismogram. The input file contained specifications for grid size and node density, location, type and frequency range of seismic source, length of time step and number of time steps to calculate the model over. Layers were added with specified

depths, P and S velocities, densities and attenuations. The model began with the source explosion at time t_0 and ran for the specified number of time steps modelling the propagation of waves from the source. The output was a record of waves arriving at the top edge of the model, essentially the same as a seismogram. By changing layer velocities and thicknesses the travel times for different arrivals can be changed. This allows for E3D software to be used to back-model, where the structure is changed to fit an observed seismogram.

References

Aharoni, E. [1991], *Seismic reflection study across the Horowhenua coastal plain, North Island, New Zealand,* Masters thesis, Victoria University of Wellington, New Zealand.

Anderton, P. [1981], Structure and evolution of the South Wanganui Basin, New Zealand, *New Zealand Journal of Geology and Geophysics* **24:** 39-63.

Barnes, P. M., Mercier de Lepinay, B., Collot, J. Y., Deltiel, J. and Audru, J. C. [1998], Strain partitioning in the transition area between oblique subduction and continental collision, Hikurangi margin, New Zealand, *Tectonics* **17** (4), 534-557.

Barnes, P. M., Nicol, A. and Harrison, T. [2002], Late Cenozoic evolution and earthquake potential of an active listric thrust complex above the Hikurangi subduction zone, New Zealand, *Geol. Soc. Am. Bull.,* **114**(11), 1379-1405.

Beanland, S. [1995], *The North Island dextral fault belt, Hikurangi subduction margin, New Zealand,* PhD thesis, Victoria University of Wellington, New Zealand.

Bekesi, G. [1989], *Geopysical studies over the north Horowhenua sedimentary basin,* Masters thesis, Victoria University of Wellington, New Zealand.

Cowie, J. D. [1963], Dune-building phases in the Manawatu District, New Zealand, *New Zealand Journal of Geology and Geophysics,* **6**: 268-280.

Dang, Y., Zhao, W., Su, A., Zhang, S., Li, M., Guan, Z., Ma, D., Chen, X., Shuai, Y., Wang, H., Tan, Y., and Xu, Z., [2008], Biogenic gas systems in eastern Qaidam Basin, *Marine and Petroleum Geology* **25** 344-356.

Darby, D. and Beavan, J. [2001], Evidence from GPS measurements for contemporary interplate coupling on the southern Hikurangi subduction thrust and for partitioning of strain in the upper plate, *J. Geophysics. Res.,* **106**(B12), 30,881-30,891.

DeMets, C., Gordon, R., Argus, D. and Stein, S. [1990], Current plate motions, *Geophysical Journal International* **101:** 425-478.

DeMets, C., Gordon, R., Argus, D. and Stein, S. [1994], Effect of recent revisions to the geomagnetic reversal time scale on estimates of current plate motions, *Geophys. Res. Lett.,* **21**(20), 2191-2194.

Ewig, E. [2008], *Lithospheric shortening and ductile deformation in a back-arc setting: South Wanganui Basin, New Zealand,* PhD thesis, Victoria University of Wellington, New Zealand.

Gardner, G. H. F., Gardner, L. W. and Gregory, A. R. [1974], Formation velocity and density – The diagnostic basics for stratigraphic traps, *Geophysics* **39**(6): 770-780.

Hammer, S. [1939], Terrain corrections for gravity stations, *Geophysics* **4**(3): 184-195.

Hunt, T. [1980], Basement structure of the Wanganui Basin, interpreted from gravity data, *New Zealand Journal of Geology and Geophysics* **23**(1): 1-16.

Knapp, R. and Steeples, D. [1986], High-resolution common-depth-point seismic reflection profiling: field acquisition parameter design, *Geophysics* **51**(2): 283-294.

Lamarche, G., Beanland, S. and Ravens, J. [2005], Deformation style and history of the Eketahuna region, Hikurangi forearc, New Zealand, from shallow seismic reflection data, *New Zealand Journal of Geology and Geophysics* **38**(1): 105-115.

Lamb, S. and Vella, P. [1987], Last million years of deformation in part of the New Zealand plate-boundary zone, *Journal of Structural Geology* **9**(7): 877-891.

Li, Y-L and Lin, C-M. [2010], Exploration methods for late Quaternary shallow biogenic gas reservoirs in the Hangzhou Bay area, eastern China, *AAPG Bulletin,* **94**(11): pp. 1741-1759.

Missiaen, T., Murphy, S., Loncke, L., and Henriet, J. P. [2002], Very high-resolution seismic mapping of shallow gas in the Belgian coastal zone, *Continental Shelf Research* **22** 2291-2301.

Nicol, A., Mazengarb, C., Chanier, F., Rait, G., Uruski, C. and Wallace, L.

[2007], Tectonic evolution of the active Hikurangi subduction margin, New Zealand, since the Oligocene, *Tectonics* **26**(4): doi:10.1029/2006TC002090.

Nicol, A. and Beavan, J. [2003], Shortening of an overriding plate and its implication for slip on a subduction thrust, central Hikurangi margin, New Zealand, *Tectonics* **22**(6), 1070, doi:10.1029/2003TC001521.

Nodder, S., Lamarche, G., Proust, J. N. and Stirling, M. [2007], Characterizing earthquake recurrence parameters for offshore faults in the low-strain, compressional Kapiti-Manawatu Fault System, New Zealand, *Journal of Geophysical Research B: Solid Earth* **112**(12): doi:10.1029/2007JB005019.

Ostrander, W. J. [1984], Plane-wave reflection coefficients for gas sands at nonnormal angles of incidence, *Geophysics* **49**: pp. 1637-1648.

Palmer, J. A. P. B. [1993], Cretaceous-Tertiary Sedimentation and Implied Tectonic Controls on the Structural Evolution of Taranaki Basin, New Zealand, *in* P. F. Ballance (ed.), *Sedimentary Basins of the World,* Elsevier, New York, pp. 309-328.

Premchitt, J., Rad, N. S., To, P., Shaw, R., and James, J. W. C. [1992], A study of gas in marine sediments in Hong Kong, *Contmental Shelf Research* **12**(10): pp 1251-1264.

Proposed Geoprobe Programme, PEP 38771 Report, Ian R Brown Associates Ltd.

Proust, J. N., Lamarche, G., Nodder, S. and Kamp, P. [2005], Sedimentary architecture of a Plio-Pleistocene proto-back-arc basin: Wanganui Basin, New Zealand, *Sedimentary Geology* **181**(3-4): 107-145.

Pulford, A. and Stern, T. [2004], Pliocene exhumation and landscape evolution of central North Island: The role of the upper mantle, *Journal of Geophysical Research* **109**.

Robertson, E. I. and Reilly, W. I. [1960], New Zealand primary gravity network, *New Zealand Journal of Geology and Geophysics* **3**(1): 41-68.

Salmon, M. L., Stern, T. A. and Savage, M. K. [2011], A major step in the continental Moho and its geodynamic consequences: the TaranakiRuapehu line, New Zealand, *Geophysical Journal International* **186**(1): 32-44.

Saunders, D. F., Burson, K. R., Branch, J. F., and Thompson, C. K. [1993], Relation of thorium-normalized surface and aerial radiometric data to subsurface petroleum accumulations, *Geophysics* **58**(10): pp. 1417-1427.

Shepard, M. J. [1985], The origin of the Koputaroa dunes, Horowhenua, New Zealand, *New Zealand Journal of Geology and Geophysics,* **28**: 323-327.

Shepard, M. J. [1987], Holocene alluviation and transgressive dune activity in the lower Manawatu Valley, New Zealand, *New Zealand Journal of Geology and Geophysics* **30**: 175-187.

Shuey, R. T. [1985], A simplification of the Zoeppritz equations, *Geophysics* **50**: 609-614.

Stern, T. A. [1987], Asymmetric backarc spreading, heat flux and structure associated with the central volcanic region of New Zealand, *Earth Planet. Sci. Lett.* **85**(1), 265-276.

Stern, T., Quinlan, G. and Holt, W. [1992], Basin formation behind an active subduction zone: Three-dimensional flexural modelling of Wanganui Basin, New Zealand, *Basin Research* **4**: 197-214.

Stern, T. A., Stratford, W. R. and Salmon, M. L. [2006], Subduction evolution and mantle dynamics at a continental margin: Central North Island, New Zealand, *Reviews of Geophysics* **44**(4): 171-207.

Stern, T. A. and Davey, F. [1990], Deep seismic expression of a foreland basin: Taranaki Basin, New Zealand, *Geology* **18**(10): 979-982.

Stock, J. and Molnar, P. [1982], Uncertainties in the relative positions of the Australia, Antarctica, Lord Howe, and Pacific plates since the Late Cretaceous, *Journal of Geophysical Research* **87**(B6): 4697-4714.

Te Punga, M. T. [1953], A late Pleistocene land bridge across Cook Strait New Zealand, *New Zealand Journal of Science and Technology,* B35: 161-192.

Te Punga, M. T. [1957], Live anticlines in western Wellington, New Zealand, *New Zealand Journal of Science and Technology,* B38: 433-446.

Tillmann, A., Englert, A., Nyari, Z., Fejes, I., Vanderborght, J., Vereecken, H. [2008], Characterization of subsoil heterogeneity, estimation of grain size distribution and hydraulic conductivity at the Krauthausen test site using Cone Penetration Test, *Journal of Contaminant Hydrology* **95**: 57-75.

Woodward, D. J. and Kicinski, J. [1987], Minisosie seismic surveys at Hinds and Orton, South Canterbury, *Seismic Surveys for Groundwater in Canterbury, New Zealand 1985-86. A Case Study* Research Report No. 217: 30–43.

Yuan, F., Bennell, J. D. and Davis, A. M. [1992], Acoustic and physical characteristics of gassy sediments in the western Irish Sea, *Continental Shelf Research,* **12**(10): pp 1121-1134.

Zoeppritz, K. [1919], Erdbebenwellen VIII B, Uber Reflexion and Durchgang seismischer Wellen durch Unstetigkeitsflachen, *Gottinger Nachr* **1**: 66-84.